Modification of nucleon-nucleon interactions in nuclear medium and neutron densities extracted via proton elastic scattering at intermediate energies

AUTHOR(S):

Takeda, Hiroyuki

Memoirs of the Faculty of Science, Kyoto University, Series of Physics, Astrophysics, Geophysics and Chemistry, Vol.XXXXIV, No.1, Article 1, 2003

Modification of nucleon–nucleon interactions in nuclear medium and neutron densities extracted via proton elastic scattering at intermediate energies

By

Hiroyuki Takeda

Department of Physics, Faculty of Science, Kyoto University
Kyoto 606-8502, Japan

(*Received December 25, 2001)*

Abstract

Spin rotation parameters of proton elastic scattering from ^{58}Ni have been measured at $E_p = 200$, 300 and 400 MeV. By combining them with the previously measured cross sections and analyzing powers at the same energies, the series of measurements has become the "complete" experiment. Cross sections and analyzing powers of proton elastic scattering from ^{58}Ni at 250 MeV, those of ^{120}Sn at $E_p = 200$, 250, 300 and 400 MeV and spin rotation parameters of ^{120}Sn at $E_p = 300$ MeV have been also newly measured. The experiment has been performed at Research Center for Nuclear Physics, Osaka University.

In order to explain the ^{58}Ni data, it has been necessary to use realistic density distributions deduced from the nuclear charge distribution and to modify coupling constants and masses of σ and ω mesons. For ^{120}Sn, we have assumed the same modification and used the proton distribution deduced from the charge distribution, we have searched the neutron density distribution which has reproduced ^{120}Sn data at 300 MeV. The deduced neutron distribution has an increase at the nuclear center, which seems to be due to wave functions of neutrons in the $3s_{1/2}$ orbit. It also explains the ^{120}Sn data at other energies than 300 MeV. Effects of ρ meson modifications on neutron densities are also mentioned.

Contents

1 Introduction

Elastic scattering of protons at intermediate energies has been successfully employed as a probe to discern various microscopic approaches to nuclear interactions. The ground state wave function of the target nucleus used for elastic scattering is restricted by the charge distribution measured by electron scattering. Thus ambiguities due to the nuclear structure are relatively small for the elastic scattering. Moreover, the mean free path of intermediate energy protons in nuclear matter is large enough to penetrate into the nucleus, thus providing some sensitivity to the nuclear interior. Therefore, a considerable number of works have been devoted to proton elastic scattering to determine interactions and nuclear structures even in the nuclear interior.

In early years these researches have based on nonrelativistic approaches. However since 1980s, the relativistic approaches based on Dirac equations have been applied to the elastic scattering of intermediate energy protons, and have successfully explained the scattering, especially polarization observables. For example, analysis on the elastic scattering of 180 MeV polarized protons by ^{40}Ca[1] has shown that the combination of strong attractive scalar and strong repulsive vector potentials in the Dirac equation has led to a moderate but unusual "wine-bottle-bottom" shape of Schrödinger potential, which had been used in some earlier analysis. The Dirac equation have been employed but the potentials used in the analysis have been phenomenological Woods-Saxon type functions. It should be mentioned that in the Dirac approach the number of free parameters is the same as or less than the number used in the standard Schrödinger potential, but fits to the data are much better. Clark *et al.* have extended the Dirac phenomenology and finally released the "Global potentials"[2], which have been able to explain elastic proton scattering off spin zero nuclei from 20 MeV to 1040 MeV for ^{12}C to ^{208}Pb targets. It was a great success in parameterizing p–Nucleus scattering, however the physical meaning of the parameters was not clear.

More fundamental approach has been presented by McNeil, Shepard and Wallace[3] who also have found a dramatic improvements for spin dependent observables for ^{16}O and ^{40}Ca at 500 MeV by using the Dirac equation. They have applied impulse approximation to the Dirac approach, where the invariant amplitude has been expressed as

$$F(q) = F^S + F^V \gamma^{\mu}_{(0)} \gamma_{(1)\mu} + F^{PS} \gamma^5_{(0)} \gamma^5_{(1)} + F^T \sigma^{\mu\nu}_{(0)} \sigma_{(1)\mu\nu} + F^A \gamma^5_{(0)} \gamma^{\mu}_{(0)} \gamma^5_{(1)} \gamma_{(1)\mu}, \tag{1}$$

and determined directly from nucleon–nucleon (NN) phase shifts. Following the success of this relativistic impulse approximation (RIA), Murdock and Horowitz[4, 5] have calculated the elastic scattering off ^{16}O, ^{40}Ca and ^{208}Pb

between 200 and 400 MeV using the RIA and obtained qualitative agreement with experimental data, especially polarization observables. Tjon, Wallace and Ottenstein[6, 7] have performed calculations of elastic scattering off ^{40}Ca using the RIA (IA2) based on the general representation of the *NN* scattering amplitudes in full Dirac space and obtained a good agreement with experimentally observed differential cross sections at 800 MeV. From these results, it appears that the RIA successfully relates the *NN* interaction inside the nucleus directly to nuclear reaction phenomena.

In our previous paper[8], we compared differential cross sections and analyzing powers in proton elastic scattering from ^{58}Ni with two RIA models: the relativistic Love-Franey (RLF) model of Murdock and Horowitz (MH), and the IA2 model of Tjon, Wallace and Ottenstein. From the analysis of differential cross sections and analyzing powers, it was found that the results obtained from both of the RIA calculations deviated from the experimental results at large angles. In order to account for the experimental data we needed to modify the *NN* interaction in the nuclear medium by altering the coupling constants between nucleons and mesons and by adjusting the masses of the exchanged mesons in the framework of the MH model since the character of the *NN* interaction could be changed in the nuclear medium.

The two RIA models (the RLF model of MH and the IA2 model) predict similar values for analyzing powers, while they predict quite different spin rotation parameter values, especially at large scattering angles. The measurement of spin rotation parameters would determine the scattering amplitudes completely (a "complete" experiment) when combined with existing data of cross sections and analyzing powers, because there are only three independent observables for proton elastic scattering from a spin zero nucleus. The existing experimental data on spin rotation parameters are limited to ^{12}C [9] or double closed shell nuclei such as ^{4}He[10], ^{16}O[9, 11, 12], ^{40}Ca[9, 11, 12, 13, 14], ^{48}Ca[9], ^{90}Zr[15] and ^{208}Pb [11, 14, 15, 16], and most of the data are restricted to forward scattering angles (momentum transfer $q \leq 2\,\mathrm{fm}^{-1}$). For these reasons, we have measured spin rotation parameters up to a high momentum transfer region ($q \leq 3.6\,\mathrm{fm}^{-1}$). With these results it is expected that we will be able to differentiate the RIA models further.

From the earliest days of nuclear physics, the spatial extent of atomic nuclei and the radial distribution of nuclear charge and matter have received considerable attention. A considerable amount of efforts have been concentrated to develop the methods for studying nuclear distributions and radii. For charge densities, electron elastic scattering and X rays from muonic and ordinary atoms were widely applied.

Contrastingly, unambiguous information about matter and neutron distributions in nuclei is much more difficult to obtain, since electromagnetic inter-

action provides little information about neutrons. Measurements of Coulomb displacement energies and of magnetic electron scattering give some constraints on the neutron excess distribution $(\rho_n - \rho_p)$ or determine certain single-nucleon orbit sizes. A large variety of strongly interacting probes have been also utilized. Among them protons at intermediate energies have an advantage in investigating the nuclear interior due to their long mean free path in the nuclear medium.

A few experiments have been performed to measure not only the radius but also the shape of the distribution of neutrons directly. One of the examples was the analysis by Ray[17], the neutron density distribution of ^{116}Sn was obtained from a nonrelativistic second-order KMT[18] optical model analysis of polarized proton scattering at 800 MeV. Resulting neutron distributions had broad error band at the nuclear center.

Our procedure is based on reliable interactions obtained by the medium modified RIA which explain ^{58}Ni very well. Applying this model to ^{120}Sn, neutron distribution were searched. The newly measured spin rotation parameter data at large scattering angles enabled us to extract neutron distribution with relatively narrow error band even at the nuclear center. It is more and more important to establish procedures to extract neutron density distributions, due to the recent experimental developments in studying unstable nuclei.

The main purpose of this work are to check various RIA models and fix the medium effects at intermediate energies in the measurement of ^{58}Ni, to check the predictability of the medium effects and the applicability to deduce the neutron density distribution for ^{120}Sn.

Note that we have already measured cross sections and analyzing powers of ^{58}Ni at 200, 300 and 400 MeV[8]. Newly measured data in this article are cross sections and analyzing powers of ^{58}Ni at 250 MeV, those of ^{120}Sn at 200, 250, 300 and 400 MeV, spin rotation parameters of ^{58}Ni at 200, 300 and 400 MeV and those of ^{120}Sn at 300 MeV. However, the explanations and discussions are performed all together in this article.

In Sec. 2, the experimental procedures and equipment are described. In Sec. 3, the procedure of the data analysis is explained. In Sec. 4, after the review of the RIA, experimental results are compared to various RIA calculations and validity of the medium effect model is checked. Using the same medium effect neutron distribution are extracted. Future perspective of the procedure especially the applicability to unstable nuclei is reviewed in Sec. 5.

2 Experimental procedures and equipment

Experiment was performed at Research Center for Nuclear Physics (RCNP), Osaka University. We have measured cross sections, analyzing powers and spin rotation parameters of proton elastic scattering from ^{58}Ni and ^{120}Sn at $E_p = 200, 300$ and 400 MeV. Overview of the RCNP facility is shown in Fig. 1. Scattering angles were up to 60° for measurements of cross sections and analyzing powers, and up to 54° for spin rotation parameters. We can determine the scattering amplitudes completely from these measurements since there are only three independent observables in proton elastic scattering from a spin zero nucleus.

2.1 Polarized proton beam

Polarized protons from a high intensity polarized ion source (HIPIS)[20] were bent from the horizontal direction to the vertical direction, injected into the AVF cyclotron, transported to the six sector ring cyclotron and accelerated to final energies. The polarization axis was in the vertical direction in the AVF cyclotron. In the measurements of spin rotation parameters where horizontally polarized beam was required, the polarization axis was rotated to the horizontal direction by using a superconducting solenoid magnet placed in the injection line to the ring cyclotron.

Spin direction and magnitude of the beam polarization were continuously monitored using two sets of the sampling-type beam line polarimeter (BLP) placed between the ring cyclotron and a scattering chamber. $(CH_2)_n$ foils of 1.13 mg/cm^2 were used as analyzer targets, which were periodically inserted into the beam position during beam polarization measurements. The frequency of the beam polarization measurements were optimized run by run according to the event rate of the standard counters. Each polarimeter utilized the left-right and up-down asymmetries in p–H scattering from the $(CH_2)_n$ foil, which determined the transverse components (p_x, p_y) of the beam polarization. Figure 2 shows the horizontal part of the counter set up of the BLP. As displayed in Fig. 3 the beam was bent by 50° with bending magnets situated between the two BLP's, named CV-BLP and WN-BLP. The spin precession in the deflecting magnets between the two BLP's enabled us to determine the longitudinal component (p_z) of the beam polarization as described in Sec. 3.1. The polarization direction of the beam was periodically reversed at intervals of one second in order to reduce systematic asymmetries. A typical beam polarization was 60–70%.

The trigger signal L (left) was generated by the kinematical coincidence of the forward L and backward L' counters, and the R (right) trigger signal by

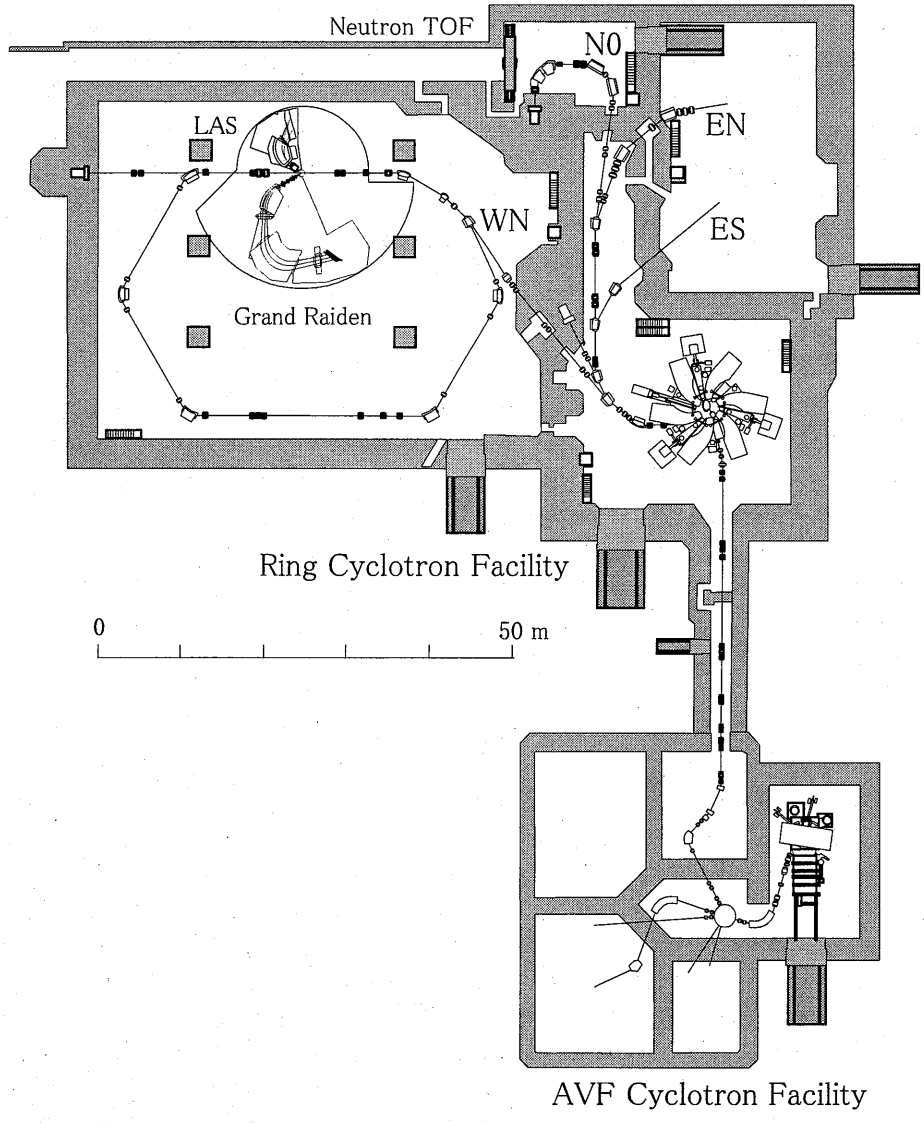

Figure 1: Overview of the RCNP facility. The experiment was performed in the WN experimental hall, where Grand Raiden spectrometer and the FPP were located.

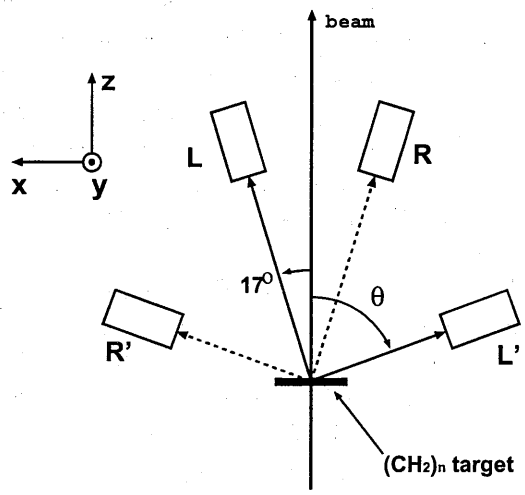

Figure 2: Top view of horizontal part of beam line polarimeter. Scattering from the hydrogen was selected by the kinematical coincidence between the scattered proton and the recoiled hydrogen. Scattering angles (denoted by θ in the figure) for backward counters were changed depending on beam energies.

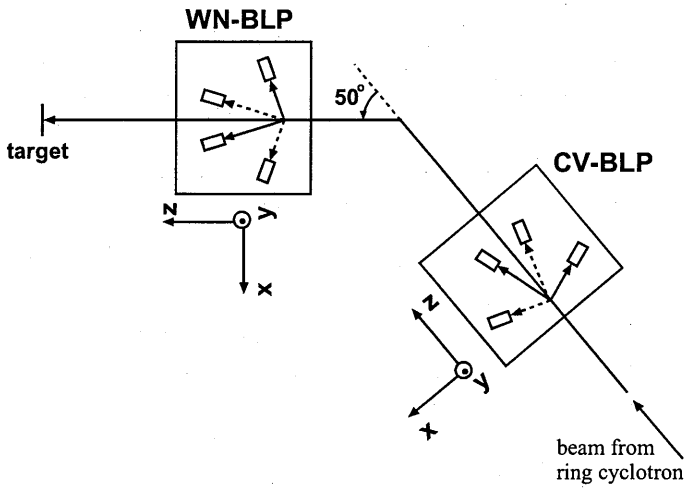

Figure 3: Two BLP's. For Q-parameter measurements we used two beam line polarimeter sets, which were separated by the bending magnet. Up-down asymmetries were measured to deduce the polarization direction in the horizontal plane.

the R and R' counters. The vertical part of the BLP has the same structure, determined the U (up) and D (down) signals. Accidental coincidence events were estimated by delaying the coincidence signals. Scattering angles of the forward counters ($LRUD$) with large acceptance were fixed at 17°, while angles of the backward counters ($L'R'U'D'$) were varied with the beam energies according to the kinematical coincidence conditions of the p–p elastic scattering, which were 71.3°, 70.5° and 69.7° for beam energies of 200, 300 and 400 MeV, respectively.

The beam was then transported to a target center in the scattering chamber. A typical beam spot size on the target was 1 mm in the vertical direction and 3 mm in the horizontal direction. Finally, the beam was stopped by a Faraday cup (FC) made of a 10.5 cm long tantalum block placed inside the scattering chamber in the case of forward angle measurements. The integrated beam current was monitored by a current digitizer. The beam current was adjusted from 0.5 nA to 10 nA depending on the scattering angle. The beam current was limited by the deadtime of the data acquisition system and leak currents of the wire chambers.

In the measurements at backward scattering angles larger than 20° the beam was not stopped in the scattering chamber, but transported to a newly developed external Faraday cup[21] located inside the shielding wall of the experimental room about 25 m downstream of the target. Beam was stopped in a 400 mm thick aluminum block which was electrically insulated in a vacuum pipe. Contrastingly, the old Faraday cup has been surrounded by the air. The current collection efficiency has been checked by the measured current ratio to the event number of elastic scattering from ^{58}Ni in the scattering chamber. The efficiency has been deviated by more than 20% from that of the FC in the scattering chamber. The deviation has been found to be due to the current leakage through the air. However, the efficiency of the new FC was stable within 3% at beam intensities from 1 to 700 nA.

2.2 Targets

Four kinds of self supporting metal foils were used for this experiment. Thin targets, 5.86 mg/cm^2 of ^{58}Ni and 5.12 mg/cm^2 of ^{120}Sn, were used for forward angle measurements in order to reduce the deadtime of the data acquisition system, while thick targets, 100.1 mg/cm^2 of ^{58}Ni and 39.87 mg/cm^2 of ^{120}Sn, were used for backward measurements to increase the yields. Enrichment of the targets were 99.875% and 98.39% for ^{58}Ni and ^{120}Sn, respectively.

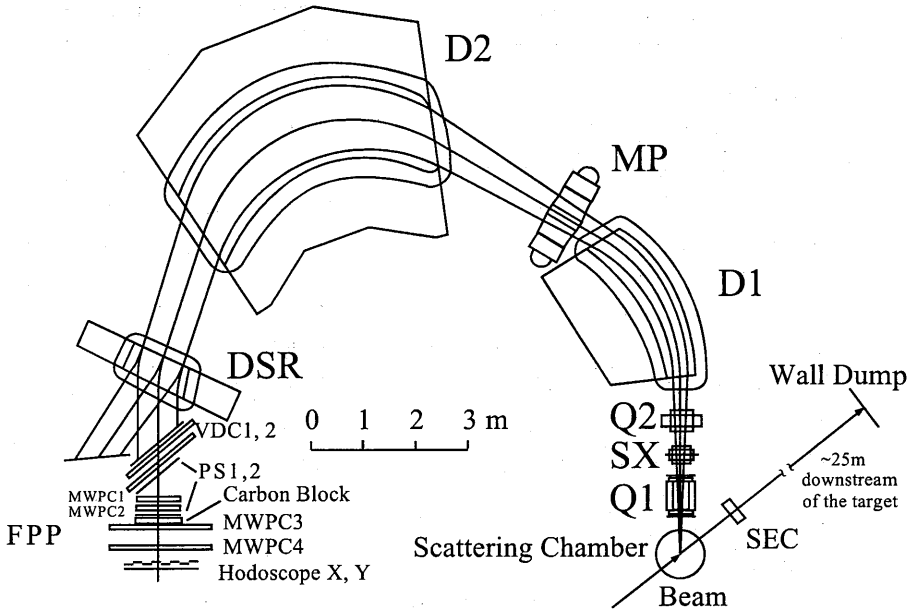

Figure 4: Grand Raiden spectrometer and the FPP. The Grand Raiden spectrometer has a Q1-SX-Q2-D1-MX-D2(-DSR) configuration. The DSR magnet was excited in the case of polarization measurement of the horizontal direction. The Focal Plane Polarimeter was located on the movable stage at the end of the spectrometer.

2.3 Grand Raiden spectrometer

Figure 4 depicts a setup of a high momentum resolution magnetic spectrometer 'Grand Raiden'[22] (GR) and focal plane detectors. The GR spectrometer has Q1-SX-Q2-D1-MX-D2(-DSR) configuration. Large momentum resolution of $p/\Delta p \sim 37,000$ and momentum acceptance of $\pm 2.5\%$ were achieved. At a position 2 m upstream of the focal plane of the spectrometer, there was an unique Dipole magnet for Spin Rotation (DSR) specially designed for the measurement of polarization of scattered particles. The DSR magnet bent the particle path by deflection angles of $+18°$ (DSR+ mode) or $-17°$ (DSR− mode), and provided two additional focal planes for polarization measurements. The design specification of the 'Grand Raiden' are summarized in Table 1. All the focal plane detectors were mounted on a pivoting carrier that was placed at the focal plane corresponding to the DSR mode. Spin precession angles in the GR could be changed by the additional deflecting angles provided by the DSR. All the components of polarization

Table 1: Design specification of the spectrometer 'Grand Raiden'.

Configuration	QSQDMD(+D)
Mean orbit radius	3 m
Total deflection angle (without DSR)	162°
Deflection angles of DSR	+18° (DSR+ mode)
	−17° (DSR− mode)
Scattering angle range	$-4° \sim 90°$
Focal plane length	150 cm
Tilting angle of focal line	45.0°
Maximum magnetic field strength	18 kG
Maximum particle rigidity	54 kG·m
Vertical magnification	5.98
Horizontal magnification	−0.417
Momentum dispersion	15.451 m
Momentum range	5 %
Momentum resolution	37076
(source width of 1 mm is assumed)	
Vertical acceptance	±70 mr
Horizontal acceptance	±20 mr

vector of scattered protons were obtained by combining the measurements in both DSR modes as described in the next section.

For the use of high intensity beam of 700 nA we have developed a remote rotation system of the GR. It enabled us to change the scattering angle of the GR without entering the experimental room. Without this system it had been necessary to wait for more than one hour before the radiation in the room had become below the dangerous level.

2.4 Focal plane detectors

Schematic view of the focal plane detector system is illustrated in Fig. 5. The system consisted of two parts, standard counters and the Focal Plane Polarimeter (FPP).

2.4.1 Standard counters

Protons scattered from the target were momentum analyzed by the Grand Raiden. The trajectory of the scattered protons was reconstructed from the position measurement made by two sets (X1,U1 and X2,U2) of vertical drift chambers (VDC's)[23], which were placed near the focal plane of the

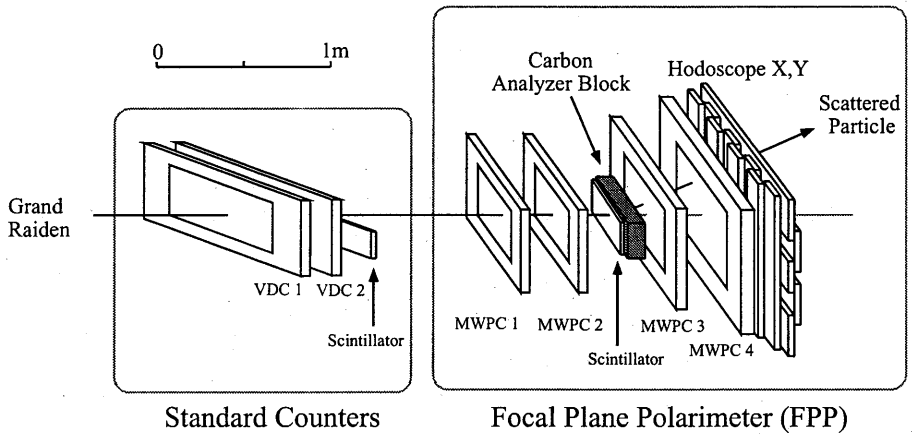

Figure 5: Focal plane detector system. The VDC1 and VDC2 are used for position and angle measurements of the scattered particles at the focal plane. MWPC1, MWPC2, MWPC3 and MWPC4 were used for the 2nd level trigger and also for offline analysis. Thickness of the carbon analyzer block was changed depending on the proton energy.

spectrometer. Wire configurations of the VDC's are illustrated in Fig. 6. Characteristics of the VDC's are summarized in Table 2.

Schematic view of the VDC structure is illustrated in Fig. 7. Chamber-gas consisted of argon (70%), isobutan (30%) and isopropyl-alcohol of saturated vapor pressure at 2°C was mixed with the argon gas at 1 atm. A high voltage of −5.6 kV was applied to the cathode planes and a voltage of −0.3 kV to the potential wires. The sense wires were remained at the ground voltage. When a charged particle passed through the electric field, the chamber-gas along the particle trajectory was ionized. Electrons in ionized gas moved

Table 2: Characteristics of the vertical drift chambers

Wire configuration	$X(0°)$, $U(-48.2°)$
Active area	1150 mm (width) × 120 mm (height)
Number of sense wires	192 (X), 208 (U)
Anode-cathode gap	10 mm
Anode wire spacing	2 mm
Sense wire spacing	6 mm (X), 4 mm (U)
Anode sense wires	20 μmϕ gold-plated tungsten wire
Anode potential wires	50 μmϕ gold-plated beryllium copper wire
Cathode film	10 μm carbon-aramid film
Applied voltage	−5.6 kV (cathode), −0.3 kV (potential), 0 V (sense)

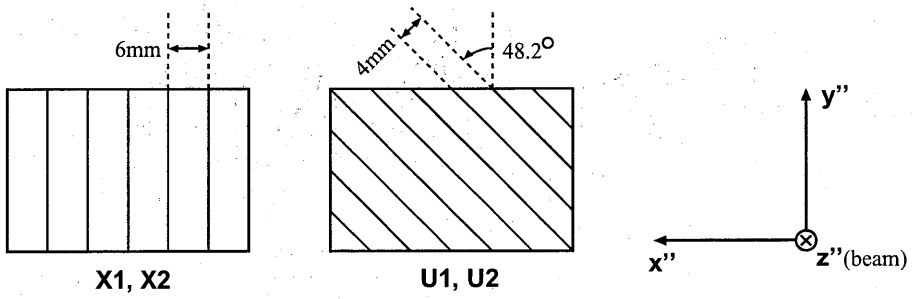

Figure 6: Wire configurations of the VDC's

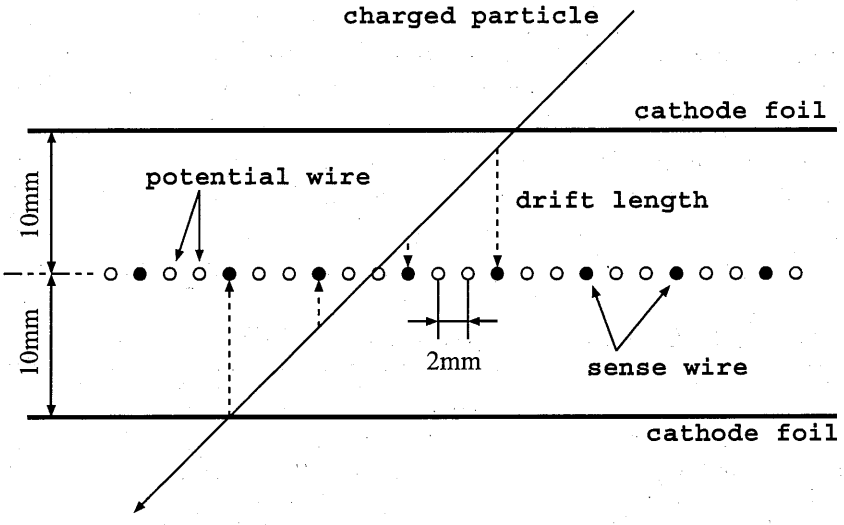

Figure 7: Schematic view of the VDC structure

to a sense wire by the electric field. The drift velocity was almost constant ($\sim 50\mu$m/nsec). Avalanche multiplication occurred near the sense wire where the electric field was so strong that electrons gained sufficient energies to induce multipilication, and generated a negative signal on the sense wire. Time difference between this signal and the delayed signal of plastic scintillators described below was digitized by a LeCroy 3377 drift chamber TDC module, which was converted to the drift length of electrons along the electric field.

Central ray of the particles from the spectrometer inclined by 45° (or 40° with the DSR magnet excited) in the horizontal plane from the normal direction of the wire plane. Thus more than two wires were hit for one trajectory in usual. These adjacent hit wires were grouped as a cluster. The intercept position of a trajectory at the wire plane was calculated by a least-squares fit method from the drift lengths of the hit wires in one cluster. Information on the incident angle was also obtained. The position resolution was about 300 μm in full width at half maximum, which corresponded to the energy resolution of 13 keV and to the angular resolution of 0.069°.

In the measurements of cross sections and analyzing powers, there were two plastic scintillating counters (PS1 and PS2) downstream of the VDC's. Thickness of the PS1 and PS2 were 10 mm. Both of them were used for triggers and particle identification. Aluminum plate of 10 mm thickness was installed between the PS1 and PS2 in order to prevent δ-electrons knocked out of the PS1 from entering the PS2, which increased background events due to the accidental coincidence.

In spin rotation parameter measurements, only the PS1 was installed and the PS2 and δ-electron supressor were removed. In this case, another plastic scintillator PS3 described below was used for triggers instead of the PS2.

2.4.2 Focal plane polarimeter

Polarizations of scattered protons were determined by using information from the focal plane polarimeter (FPP), which measured scattering asymmetries in a carbon analyzer block. The FPP consisted of two multiwire proportional chambers (MWPC's; MWPC1 and MWPC2), a 3 mm thick plastic scintillator (PS3), a carbon analyzer block, two additional MWPC's (MWPC3 and MWPC4), and two sets of plastic scintillator hodoscopes (HODO-X and HODO-Y).

The MWPC1 and MWPC2 had single X planes named MWPC-X1 and -X2, respectively, while the MWPC3 and MWPC4 consisted of X, U, V planes named MWPC-X3, -U3, -V3 and MWPC-X4, -U4, -V4, respectively. The MWPC-X3 and -X4 planes were not operated in this experiment. The specifications of the MWPC's are summarized in Table 3. Wire configura-

Table 3: Specifications of the MWPC's

	MWPC1,2	MWPC3	MWPC4
Wire configuration	$X(0°)$	$X(0°)$, $U(-45°)$, $V(+45°)$	
Active area	$760^{W} \times 200^{H}$ mm	$1400^{W} \times 418^{H}$ mm	$1400^{W} \times 600^{H}$ mm
Number of wires	384	704 (X), 640 (U, V)	704 (X, U, V)
Anode-cathode gap	6 mm		
Anode wire spacing	2 mm		
Anode wires	25 mmϕ gold-plated tungsten wire		
Cathode film	10 μm carbon-aramid		6 μm aluminized mylar
Cathode voltage	-4.9 kV	-4.7 kV	

tions of the MWPC's and schematic view of the structure of one of MWPC's are illustrated in Fig. 8 and 9, respectively. Chamber-gas was a mixture of argon (66%), isobutane (33%), freon (0.3%) and isopropyl-alcohol of saturated vapor pressure at 2°C was mixed with the argon gas at 1 atm.

Operation of the MWPC's was simple compared to the VDC's. Only the hit pattern of sense wires was read out and the drift times were not measured. Thus the position resolutions of the MWPC's were determined by the anode wire spacing of 2 mm, which corresponded to the angular resolution of 0.45° in horizontal or vertical directions. The actual resolution was slightly better since adjacent two wires were hit when a trajectory passed through near the middle of wires. The LeCroy PCOSIII system clusterized the hit pattern, transferred the central position and the width of each cluster.

The carbon block was 100 cm wide, 20 cm high and the thickness was changed according to the beam energies as 4 cm, 9 cm and 12 cm for T_p = 200 MeV, 300 MeV and 400 MeV, respectively. These values were chosen in order to optimize the figure of merit.

The hodoscopes were located downstream of the MWPC's. The HODO-X consisted of eight vertically placed plastic scintillators of dimension 250 mm (width) × 1000 mm (height) × 10 mm (thickness). The HODO-Y consisted of five horizontally placed plastic scintillators. The central one was 1500 mm (width) × 100 mm (height) × 10 mm (thickness) and the other four were 1500 mm (width) × 150 mm (height) × 10 mm (thickness). The scintillators of the HODO-X and the HODO-Y were placed to overlap each other as shown in Fig. 5.

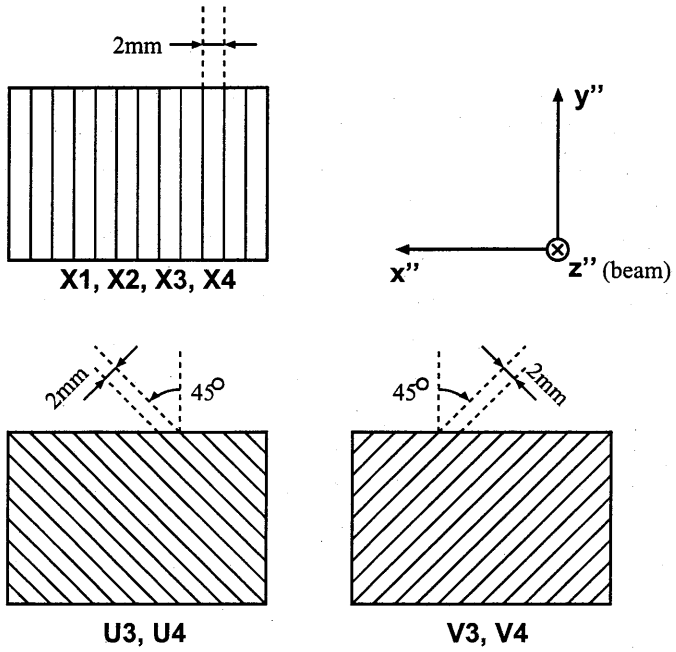

Figure 8: Wire configurations of the MWPC's

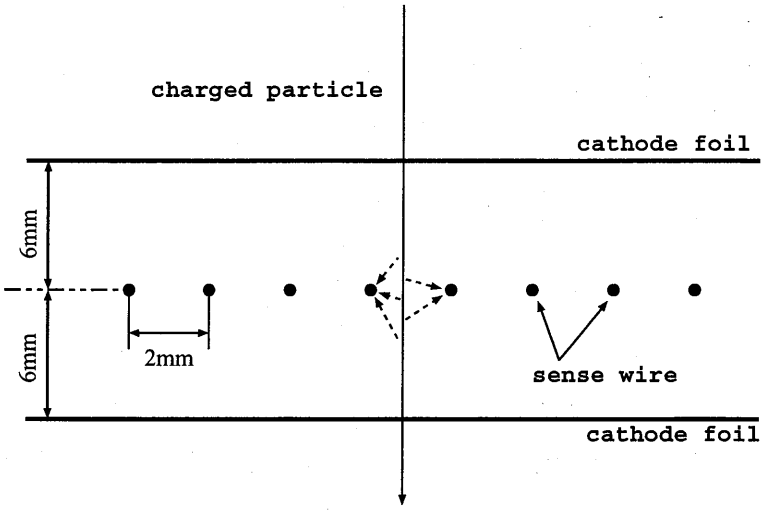

Figure 9: Schematic view of the MPWC structure

2.5 Triggers

2.5.1 First level triggers

The first level trigger consisted of two types of triggers; FP and FPP triggers. The FP (focal plane) triggers were generated by taking the coincidence of the signals from the PS1 and PS2 (or the PS1 and PS3 in the measurements using the FPP). Each PS signal was the coincidence of the photo-multiplier tube (PMT) signals from both sides of the plastic scintillator. The FPP (focal plane polarimeter) triggers were the coincidence of the HODO-X, HODO-Y and the FP trigger described above. The HODO-X signals were generated by taking OR of all HODO-X scintillator signals. Similarly the HODO-Y signals were OR of all HODO-Y scintillators. Each scintillator signal was the coincidence of PMT signals from both sides. In the measurements without the FPP only the FP triggers were used.

A LeCroy 2366 Universal Logic Modules (ULM's) with field programmable gate arrays (FPGA's) were employed for the core of the trigger system[24]. Logic circuits were designed on a personal computer and downloaded into the FPGA's.

2.5.2 Second level triggers

Most of the first level triggered events corresponded to small scattering angles in the carbon block. These events were of no use to determine the polarization of the protons since the analyzing powers were too small. In order to reduce such meaningless events without any software intervention the second level trigger system have been developed[25]. The system calculated an approximate scattering angle in a few μsec and made decision whether to accept or to reject the event. The system was also based on the LeCroy 2366 ULM.

The horizontal direction of the incoming particle to the carbon block is approximately expressed as

$$\theta_x^{in} \sim \frac{x_2 - x_1}{L_{12}}, \tag{2}$$

where $x_{1(2)}$ is the position of the hit wire of the MWPC-X1(2), L_{12} is the distance between the MWPC-X1 and -X2. The incoming particles were almost in the horizontal plane due to the ion optical properties of the GR, thus the vertical angle was assumed to be 0° for the second level trigger. The projections onto the $U(-45°)$ and $V(+45°)$ planes were written as

$$\theta_u^{in} \sim -\frac{x_2 - x_1}{\sqrt{2}L_{12}}, \tag{3}$$

$$\theta_v^{in} \sim +\frac{x_2 - x_1}{\sqrt{2}L_{12}}. \quad (4)$$

Similarly the (U, V) components of the directions of the outgoing particles from the carbon block are

$$\theta_u^{out} \sim \frac{u_4 - u_3}{L_{34}}, \quad (5)$$

$$\theta_v^{out} \sim \frac{v_4 - v_3}{L_{34}}, \quad (6)$$

where u_3, u_4, v_3 and v_4 are positions of hit wires of the MWPC-U3, -U4, -V3 and -V4, L_{34} is the distance between the MWPC-U3 and -U4, which is equal to the distance between the MWPC-V3 and -V4. L_{34} have been designed to be $\sqrt{2}$ times longer than L_{12};

$$L_{34} = \sqrt{2}L_{12}. \quad (7)$$

Using the above relations, approximate scattering angles are reduced to

$$\begin{aligned} \theta_u &= \theta_u^{out} - \theta_u^{in}, \\ &\propto (u_4 - u_3) + (x_2 - x_1), \quad (8) \\ \theta_v &= \theta_v^{out} - \theta_v^{in}, \\ &\propto (v_4 - v_3) - (x_2 - x_1). \quad (9) \end{aligned}$$

Only additional and subtractional operations are contained in (8) and (9) thus they can be performed by simple logic circuits downloaded into the FPGA chip of the ULM module.

The hit wire position data were transported to the ULM via the ECL port of the LeCroy PCOSIII controller. The ULM calculated (8) and (9), compared with the accept/reject matrix on the LeCroy 2372 Memory Lookup Unit and made a decision whether to accept or to reject. The accept/reject matrix was downloaded by CAMAC functions in advance of the measurements. When multi-cluster events were occurred, the ULM surveyed all combinations of the clusters. The event was rejected if all combinations were rejected. If the event was rejected, fast clear signals were distributed to reset all circuits and to prepare for the next event. Typical second level cut is shown in Fig. 10 as scatter plots of Y angle versus X angle of the scattering in the carbon block. The left side of the figures is for the first level triggers, the right part for the second level triggers. It can be seen that events in the small scattering angle region are suppressed by the second level trigger.

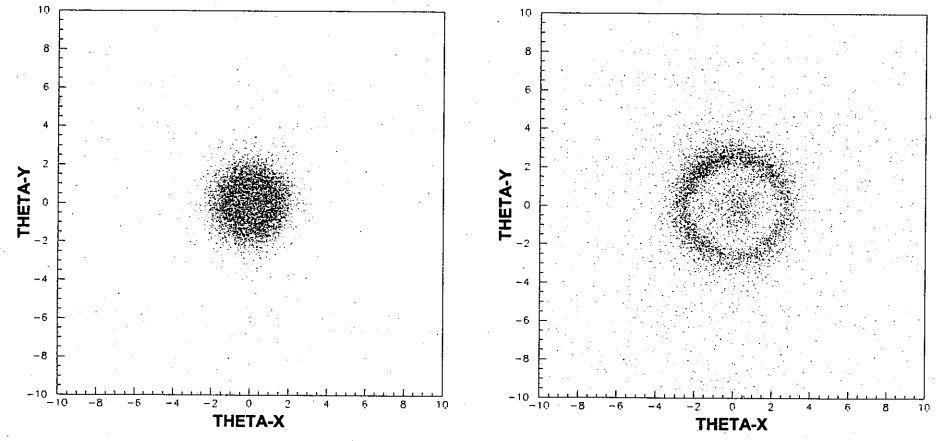

Figure 10: Scatter plots of vertical angle versus horizontal angle of scattering in the carbon block. The left figure shows the scattered plot of the 1st level trigger, while the right figure displays the result of the 2nd level trigger.

2.6 Data acquisition system

A new data acquisition (DAQ) system has been developed[26] for high rate measurements with the FPP system. Overview of the DAQ system is displayed in Fig. 11. The drift time data of VDC's were digitized by the LeCroy 3377 Drift Chamber TDC's and transferred to a pair of the LeCroy 1190 Dual Port Memory Modules on a VME system via FCET (Flow Controlling Event Tagger) modules[27] newly designed and produced by us. The event header, the event number and the input register words were appended event by event by the FCET. The hit wire positions of the MWPC's were clusterized and digitized by the LeCroy PCOSIII system described above, transferred to a CES HSM8170 High Speed Memory module with a RDTM (Rapid Data Transfer Module)[28] also newly designed for the FPP. The RDTM received the data via the LeCroy DATABUS in differential TTL logic signals, converted to ECL logic signals, and transferred to the HSM with appending event header and event counter to each event. Details of this module are described in Appendix D. Timing and charge signals of plastic scintillators were digitized by the LeCroy FERA/FERET system. These data were also transferred to another pair of the LeCroy 1190 Dual Port Memories via the ECL BUS.

As described above a pair of memories was assigned for each counter system (the HSM was operated in the double buffer mode). Data were stored in

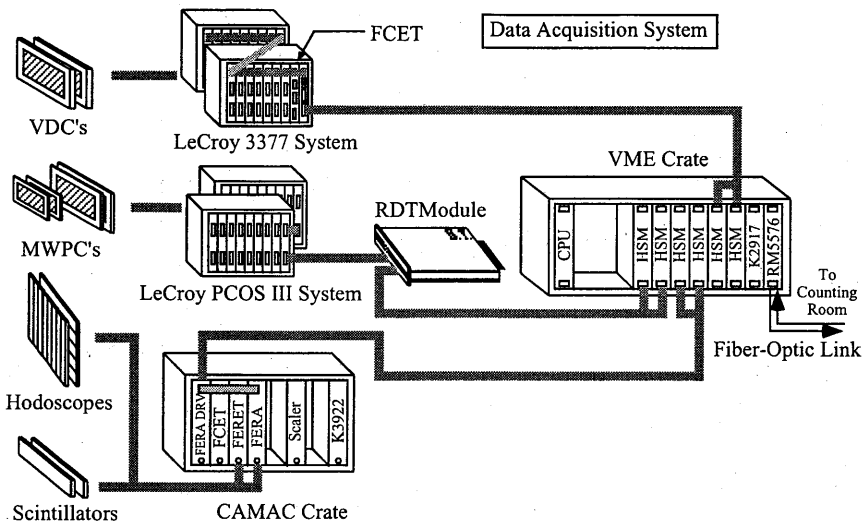

Figure 11: Overview of the DAQ system. Raw data with sequential event numbers were stored in parallel into the dual buffered memories of VME by the hardware logic without any software intervention. They were then transferred to the storage device via a fiber optical link.

one of the double buffer memories. When a buffer reached near the full memory, it switched to an inactive mode and another buffer was activated. This switching took place for all pairs of memories at once. Data in each inactivated memory were transferred and stored as each data block in a VMIC reflective memory (RFM) module via the VME bus. Stored data in the RFM were automatically distributed to the counting room via a fiber-optic link and stored in another RFM. Data transfer rates of up to 2 MBytes/sec were achieved.

The data conversion, accumulation and distribution described above were performed only by hardware logics without any software intervention nor CAMAC functions. We have developed the RDTM and FCET modules for this purpose.

Transferred data in the RFM of the counting room were read out by SUN workstations, which stored the data on hard disks and reconstructed the events in separate data blocks to perform online analysis for monitoring the detectors.

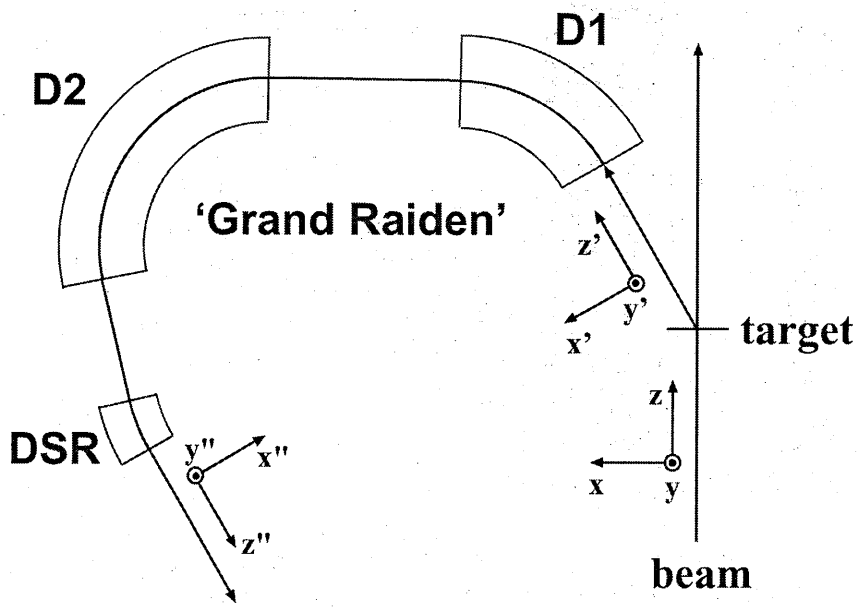

Figure 12: Definition of the coordinate system used in the data reduction.

3 Data reduction and results

In this section the following notation is used in general to distinguish the coordinate systems;

- (x, y, z) for the beam,
- (x', y', z') for the particles just after the scattering,
- (x'', y'', z'') for the particles after passing through the Grand Raiden,

as shown in Fig. 12. All of them axes directions are defined according to the Madison convention[29].

3.1 Beam polarization

The proton beam polarization was measured by two sets of beam line polarimeters (BLP's) as was described in Sec. 2.1. The x components of the beam polarization at the CV-BLP were obtained as

$$p_{x\uparrow}^{\mathrm{C}} = \frac{1}{A_y^{\mathrm{BLP}}} \cdot \frac{2Q - (D+U)}{D-U}, \tag{10}$$

Table 4: Analyzing powers of the $(CH_2)_n$ target of CV- and WN-BLP's.

Energy (MeV)	200	300	400
$A_y^{\rm BLP}$	0.29 ± 0.02	0.40 ± 0.01	0.44 ± 0.02

$$p_{x\downarrow}^{\rm C} = \frac{1}{A_y^{\rm BLP}} \cdot \frac{2Q^{-1} - (D^{-1} + U^{-1})}{D^{-1} - U^{-1}}, \tag{11}$$

$$U \equiv \frac{N_{U\downarrow}^{\rm C}}{N_{U\uparrow}^{\rm C}}, \quad D \equiv \frac{N_{D\downarrow}^{\rm C}}{N_{D\uparrow}^{\rm C}}, \quad Q \equiv \frac{Q_{\downarrow}^{\rm C}}{Q_{\uparrow}^{\rm C}}, \tag{12}$$

where $\uparrow$ and $\downarrow$ relate to the spin direction at the ion source, $N_{U(D)}^{\rm C}$ are the number of coincidence events after subtracting accidental coincidence of UU' (DD') counters of the CV-BLP, $Q^{\rm C}$ stands for the number of protons in the beam, respectively. $A_y^{\rm BLP}$ is an analyzing power of the $(CH_2)_n$ target. $A_y^{\rm BLP}$ has been measured in a separate run by comparing with another polarimeter N-BLP. The N-BLP has been located at the injection line of the ring cyclotron where the beam energies have been 39, 53 and 65 MeV for the final energies of 200, 300 and 400 MeV, respectively. The N-BLP has utilized the up-down and left-right asymmetries in p–C elastic scattering in a $(CH_2)_n$ foil with CsI crystal counters to determine the polarization. Analyzing powers of p–C elastic scattering at these lower energies had been measured precisely at RCNP[30]. Obtained analyzing powers of CV- and WN-BLP's are summarized in Table 4. Uncertainties in the x component of beam polarization were expressed as

$$\begin{aligned}
\Delta p_{x\uparrow}^{\rm C} &= \frac{2}{A_y^{\rm BLP}} \cdot \frac{UD}{(U-D)^2} \\
&\times \left[\left(\frac{Q}{U} - 1 \right)^2 \left(\frac{1}{N_{D\uparrow}} + \frac{1}{N_{D\downarrow}} \right) + \left(\frac{Q}{D} - 1 \right)^2 \left(\frac{1}{N_{U\uparrow}} + \frac{1}{N_{U\downarrow}} \right) \right. \\
&\left. + \left(\frac{(U-D)^2}{2UD} p_{x\uparrow}^{\rm C} \Delta A_y^{\rm BLP} \right)^2 \right]^{1/2}, \qquad (13) \\
\Delta p_{x\downarrow}^{\rm C} &= \frac{2}{A_y^{\rm BLP}} \cdot \frac{U^{-1}D^{-1}}{(U^{-1} - D^{-1})^2} \\
&\times \left[\left(\frac{Q^{-1}}{U^{-1}} - 1 \right)^2 \left(\frac{1}{N_{D\uparrow}} + \frac{1}{N_{D\downarrow}} \right) + \left(\frac{Q^{-1}}{D^{-1}} - 1 \right)^2 \left(\frac{1}{N_{U\uparrow}} + \frac{1}{N_{U\downarrow}} \right) \right.
\end{aligned}$$

$$+\left(\frac{(U^{-1}-D^{-1})^2}{2U^{-1}D^{-1}}p^{\mathrm{C}}_{x\downarrow}\Delta A_y^{\mathrm{BLP}}\right)^2\Bigg]^{1/2}. \tag{14}$$

Similarly the y components of beam polarization and their uncertainties were obtained by replacing U, D with R, L in (10)$\sim$(14), respectively. The x, y components of the beam polarization at the WN-BLP were obtained in the same manner.

The beam was bent by 50° between the two BLP's as described in Sec. 2.1. As is generally known the spin precesses in dipole fields of bending magnets. The precession angle χ relative to the beam trajectory after passing through the magnetic field is expressed as

$$\chi = \gamma\left(\frac{g_p}{2}-1\right)\chi_L, \quad \gamma = \frac{T_p + m_pc^2}{m_pc^2}, \tag{15}$$

where χ_L is the deflection angle of the proton beam, g_p, T_p and m_pc^2 denote the gyro-magnetic ratio, the kinetic energy and the rest energy of proton, respectively. Thus the relation between the polarization components of CV- and WN-BLP's are

$$\begin{pmatrix} p^{\mathrm{W}}_x \\ p^{\mathrm{W}}_y \\ p^{\mathrm{W}}_z \end{pmatrix} = \begin{pmatrix} \cos\chi_{\mathrm{cw}} & 0 & \sin\chi_{\mathrm{cw}} \\ 0 & 1 & 0 \\ -\sin\chi_{\mathrm{cw}} & 0 & \cos\chi_{\mathrm{cw}} \end{pmatrix} \begin{pmatrix} p^{\mathrm{C}}_x \\ p^{\mathrm{C}}_y \\ p^{\mathrm{C}}_z \end{pmatrix}, \tag{16}$$

where χ_{cw} is a precession angle between CV- and WN-BLP's obtained by (15). From (16), z components of the beam polarization were calculated as

$$p^{\mathrm{C}}_{z\uparrow(\downarrow)} = \frac{p^{\mathrm{W}}_{x\uparrow(\downarrow)} - p^{\mathrm{C}}_{x\uparrow(\downarrow)}\cos\chi_{\mathrm{cw}}}{\sin\chi_{\mathrm{cw}}}, \tag{17}$$

$$\Delta p^{\mathrm{C}}_{z\uparrow(\downarrow)} = \sqrt{\left(\frac{\Delta p^{\mathrm{W}}_{x\uparrow(\downarrow)}}{\sin\chi_{\mathrm{cw}}}\right)^2 + \left(\frac{\Delta p^{\mathrm{C}}_{x\uparrow(\downarrow)}}{\tan\chi_{\mathrm{cw}}}\right)^2}, \tag{18}$$

$$p^{\mathrm{W}}_{z\uparrow(\downarrow)} = \frac{p^{\mathrm{W}}_{x\uparrow(\downarrow)}\cos\chi_{\mathrm{cw}} - p^{\mathrm{C}}_{x\uparrow(\downarrow)}}{\sin\chi_{\mathrm{cw}}}, \tag{19}$$

$$\Delta p^{\mathrm{W}}_{z\uparrow(\downarrow)} = \sqrt{\left(\frac{\Delta p^{\mathrm{W}}_{x\uparrow(\downarrow)}}{\tan\chi_{\mathrm{cw}}}\right)^2 + \left(\frac{\Delta p^{\mathrm{C}}_{x\uparrow(\downarrow)}}{\sin\chi_{\mathrm{cw}}}\right)^2}. \tag{20}$$

$p^{\mathrm{W}}_{x,y,z\uparrow(\downarrow)}$ are used as the beam polarization $p_{x,y,z\uparrow(\downarrow)}$ on the target.

3.2 Particle identifications

For charged particles in the same material medium, the Bethe-Bloch's energy loss formula[31] can be reduced as

$$-\frac{dE}{dx} = z^2 f(\beta), \tag{21}$$

where z is the charge of the particle, $f(\beta)$ is a function of the particle velocity β only. Charged particles after passing through the spectrometer have almost same values of momentum to ion charge ratio $p/q = B\rho$ since the magnetic field B is almost uniform in the dipole magnets and the radii of the particle orbits ρ change only a little in the acceptance of the spectrometer. In such case, particle velocity β is a function of the mass to charge ratio m/q of the charged particle only. Thus $-dE/dx$ becomes characteristic quantity of the charged particle.

The light output I_0 in the plastic scintillator are proportional to $-dE/dx$. The light is absorbed exponentially in passing through the scintillator and the light intensity at the distance l from the point of charged particle becomes

$$I(l) = I_0 \exp(-l/\lambda), \tag{22}$$

where λ is the attenuation length of the scintillator. This position dependence due to the attenuation can be cancelled by taking a geometrical average of light intensities measured by photo-multiplier tubes on both sides of the scintillator. Suppose x to be a position where a charged particle passes through, L_0 to be the total length of the scintillator. Geometrical mean I_{mean} becomes

$$\begin{aligned} I_{\mathrm{mean}} &= \sqrt{I(x)I(L_0 - x)} \\ &= I_0 \exp(-L_0/2\lambda) \\ &\propto -\frac{dE}{dx}. \end{aligned} \tag{23}$$

Thus I_{mean} independent of the position of the particle but dependent on the energy losses only and can be used for the particle identification.

Figure 13 shows the I_{mean} of PS1 versus the X position at the focal plane. X position measurements are mentioned in the next subsection. Protons are clearly separated from deuterons and tritons. Small position dependence can be seen in the figure. It seems due to the position dependent effects which cannot be cancelled by the method describes above, such as escape of light from the surface of the scintillator.

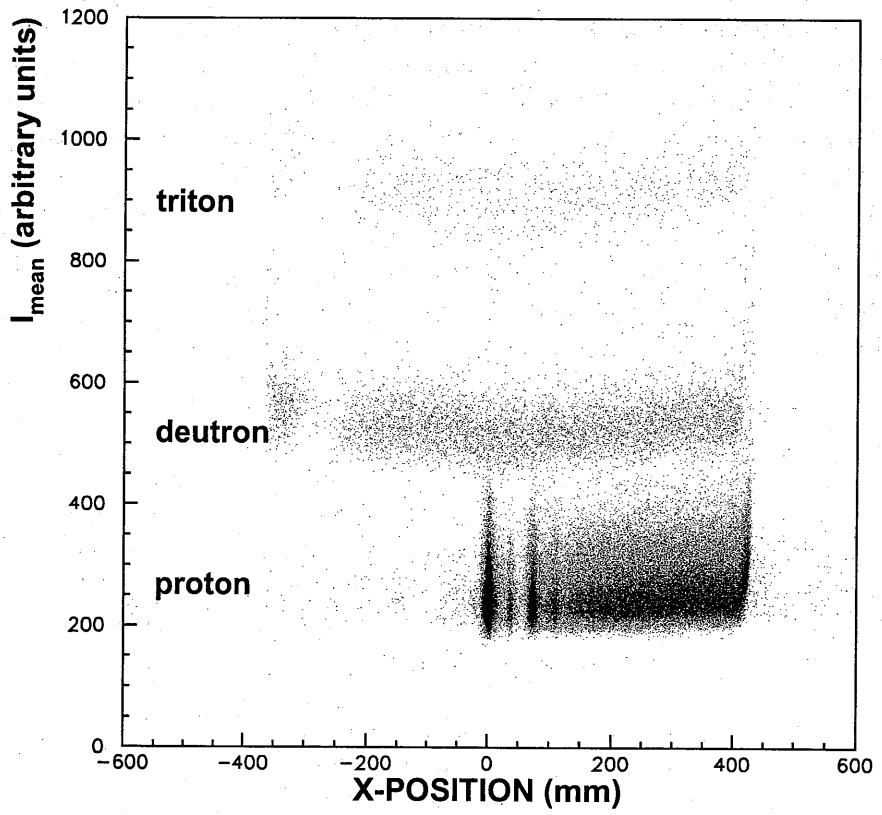

Figure 13: Scatter plot of I_{mean} (geometrical mean of the light outputs of the both sides of the scintillator) versus the X position at the focal plane. Protons and deuterons were separated clearly.

3.3 Excitation energy measurements with VDC

The following procedures were applied for the reconstruction of the trajectory of passed particles in the VDC's. For each VDC plane;

- It required that a cluster had at least two hit wires. The events with a single hit wire were ignored.
- If there were more than two hit wires in a single cluster, the wire with shortest drift time (*i.e.* nearest to the ray) in the cluster was ignored, since the uniformity of the electric field was distorted near the sense wire which caused relatively large uncertainty in the conversion of the drift time to the drift length.
- The intercept position and angle for each cluster were calculated by a least-squares fitting.

If more than one clusters existed in the VDC-X1 and/or -X2, the consistency among the angles was checked for all the possible combinations; one was the angle determined from X1 and X2 positions of the clusters while the other two were the angles obtained from single plane analysis described above for X1 and X2 planes. Inconsistent combinations were eliminated. Similar consistency check was performed if more than one clusters existed in the VDC-U1 and/or VDC-U2. This multi-cluster treatment significantly improved the efficiencies of the VDC's as described below. After the multi-cluster treatment, neither the events with one or more planes in which the hit positions could not be determined nor the remaining multi-cluster events were used in this analysis. Three dimensional ray of each particle was reconstructed from the hit positions of all the planes.

The rotation of VDC's around the x''-axis was adjusted so that the distribution of vertical angles of the rays became symmetrical around 0°. This correction was order of 0.1°. The rotation around the z''-axis was ignored. Since only the relative angle to the FPP was important, the rotation around the y''-axis was fixed at the designed value of 45° (or 40° in the measurements using the FPP).

None of planes of the VDC's was actually located on the focal plane of the spectrometer thus the raw position spectrum was broadened. After the raytracing of VDC's, it was able to make two dimensional X-θ plots on any virtual plane with arbitrary z'' position and inclination angle. The focal plane was searched by changing position and angle of the virtual plane so that X positions of protons with same momentum were independent of θ which meant that any locuses in the X-θ plot were straight and parallel to the θ axis over the acceptance region. Figure 14 shows the result of focal

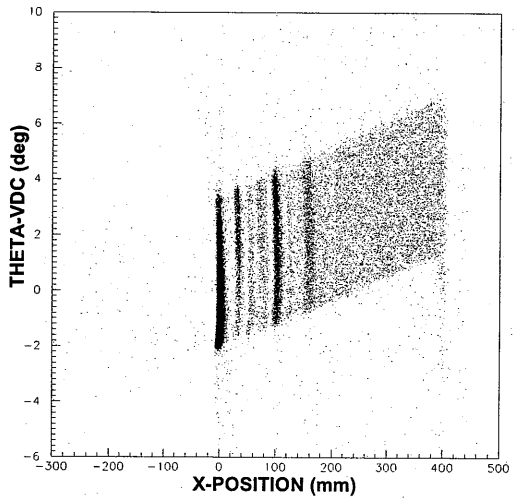

Figure 14: X-θ plot at the focal plane of the spectrometer. z'' position and inclination angle of the focal plane were determined so that any locuses in the X-θ plot became straight and parallel to the θ-axis as shown in the figure.

plane search. Figure 15 shows an example of excitation energy spectrum at the focal plane. This is the case of proton elastic scattering from ^{58}Ni at 400 MeV and the scattering angle $\theta_{\rm LAB}$ is 11.5°.

The efficiency of the VDC-X1 was estimated as

$$\varepsilon_{X1} = \frac{N_{X1,U1,X2,U2}}{N_{X1,U1,X2,U2} + N_{\bar{X}1,U1,X2,U2}}, \tag{24}$$

where $N_{X1,U1,X2,U2}$ denotes the number of events in which the cluster positions can be determined for all planes, while $N_{\bar{X}1,U1,X2,U2}$ is the same but the cluster position in X1 plane cannot be determined. The efficiencies of other planes were estimated in a similar way. Obtained efficiencies were 95∼98% per plane. The total efficiency is estimated by multiplying the efficiencies of all four planes;

$$\varepsilon_{total} = \varepsilon_{X1}\varepsilon_{U1}\varepsilon_{X2}\varepsilon_{U2}. \tag{25}$$

If the multi-cluster treatments described above were not performed, the efficiency of each plane would reduce to be less than 90% in the case of high intensity beam of a few hundred nA in the backward angle measurements, which caused severe reduction of the total efficiency.

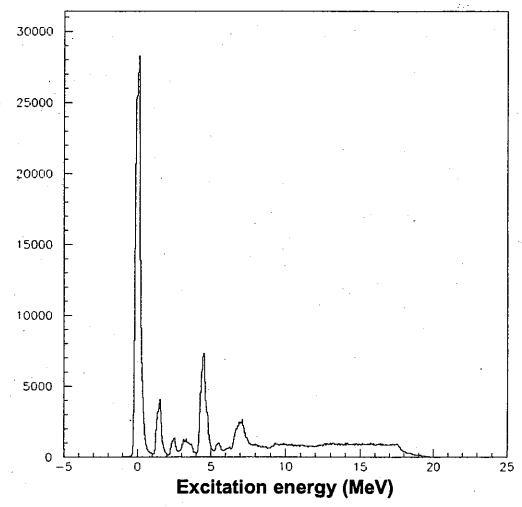

Figure 15: Example of the excitation energy spectrum at the focal plane. This is the case of proton elastic scattering from ^{58}Ni at 400 MeV. θ_{LAB} is 11.5°.

3.4 Polarization measurements with FPP

3.4.1 Raytrace of the particles in the MWPC's

The MWPC-X1 and -X2 planes were used only in the second level trigger system described in Sec. 2.5.2. The data of these planes were recorded but not used in the offline analysis since the raytrace of the VDC's provided the same but much precise information on the incoming particles into the carbon block.

The following procedures were applied in reconstructing the rays from the MWPC3 and MWPC4.

- If all planes had one or more clusters, consistency with the hit pattern of the hodoscopes was checked for all combinations of clusters. Inconsistent combinations were removed.
- For each combination of clusters consistent with hodoscopes, the distance between the ray of the combination and the incoming ray determined by the VDC raytrace was calculated.
- The combination with the smallest distance to the incoming ray was selected.

If the positions could not determined in one or more planes, the events were not used in the data analysis.

Positions and rotations of the MWPC's relative to the VDC's were adjusted using the trajectory data. The rotation around z''-axis was ignored. The rotation around x''- and y''-axes were adjusted so that the rays became parallel to the rays determined by the VDC's. The x'' and y'' positions of the MWPC's were adjusted so that the position differences between the MWPC's and VDC's became symmetrical around 0.

Scattering vertices at the carbon block were obtained as follows. Suppose ℓ_i and ℓ_f are straight lines representing the incoming and outgoing rays. If ℓ_i and ℓ_f are not parallel, there is the point P_i on ℓ_i nearest to ℓ_f, whereas the P_f also exists on ℓ_f nearest to ℓ_i. The distance between the two lines were determined as the distance between the P_i and P_f. A typical distribution of the distance is shown in Fig. 16. The vertex point was determined as the middle point of the segment P_iP_f. Figure 17 shows an example of Z vertex distribution. The horizontal axis represents the distance in millimeter from the VDC-X1 plane along the z'' direction. Fake peaks around $Z =$ 1870 mm and 2233 mm are due to the wrong selection of multi-cluster events in the MWPC-U3 and -U4 planes, respectively. Note that these fake peaks appeared only in the case of high room background measurements where 10 nA beam was stopped in the Faraday cup inside the scattering chamber. They disappeared in usual. Only the events in a C-block gate indicated by a hatched area were used in the analysis.

3.4.2 Scattering angle in the carbon block

Suppose $\hat{p}_i$ and $\hat{p}_f$ are unit vectors parallel to the incoming and outgoing rays obtained by the VDC's and MWPC's, respectively. The polar scattering angle $\theta_{\rm FPP}$ in the carbon block is obtained by taking a scalar product of $\hat{p}_i$ and $\hat{p}_f$;

$$\cos\theta_{\rm FPP} = \hat{p}_i \cdot \hat{p}_f. \tag{26}$$

In general incoming ray is not parallel to the z''-axis fixed on the detector system. In order to determine the azimuthal angle $\phi_{\rm FPP}$, new coordinate system $(\tilde{x}, \tilde{y}, \tilde{z})$ along to each incoming ray is introduced, where the $\tilde{z}$-axis is taken parallel to the incoming ray;

$$\tilde{z} = \hat{p}_i, \tag{27}$$

the $\tilde{x}$-axis is in the direction normal to the plane determined by y'' and $\tilde{z}$ axes;

$$\tilde{x} = \frac{(0,1,0) \times \tilde{z}}{|(0,1,0) \times \tilde{z}|}, \tag{28}$$

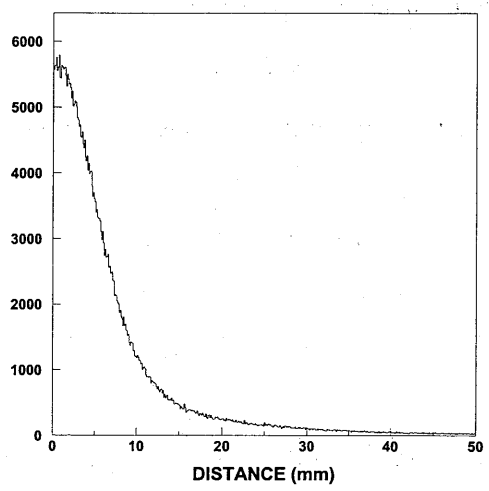

Figure 16: A typical distribution of the distance between incoming and outgoing ray.

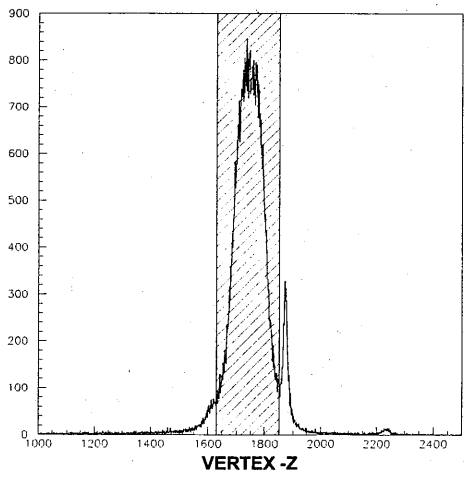

Figure 17: An example of Z vertex distribution. The horizontal axis represents the distance in millimeter from the VDC-X1 plane along the z'' direction. Fake peaks around $Z = 1870\,\mathrm{mm}$ and $2233\,\mathrm{mm}$ are due to the wrong selection of multi-cluster events in the MWPC-U3 and -U4 planes, respectively. Only the events in a C-block gate indicated by a hatched area were used in the analysis.

where $(0,1,0)$ is a unit vector parallel to y''-axis. Finally $\tilde{y}$ is determined so that $(\tilde{x},\tilde{y},\tilde{z})$ becomes right-handed coordinate;

$$\tilde{y} = \tilde{z} \times \tilde{x}. \tag{29}$$

$\tilde{x}$ and $\tilde{y}$ components of the outgoing ray are expressed as

$$\hat{p}_{f\tilde{x}} = \hat{p}_f \cdot \tilde{x}, \tag{30}$$

$$\hat{p}_{f\tilde{y}} = \hat{p}_f \cdot \tilde{y}. \tag{31}$$

Thus ϕ_{FPP} can be obtained as

$$\tan\phi_{\mathrm{FPP}} = \frac{\hat{p}_{f\tilde{y}}}{\hat{p}_{f\tilde{x}}}. \tag{32}$$

3.4.3 Polarization of scattered protons

In general, number of events scattered in the carbon block into a solid angle $d\Omega$ with the direction of $(\theta_{\mathrm{FPP}},\phi_{\mathrm{FPP}})$ is expressed as

$$dN(\theta,\phi) \propto \frac{d\sigma}{d\Omega}(\theta)\left\{1 + |p''_{x''y''}|A_y(\theta)\sin(\phi-\phi_p)\right\}d\Omega, \tag{33}$$

where the subscript "FPP" of θ and ϕ is omitted for simplicity, $d\sigma/d\Omega$ and A_y are the differential cross section and the analyzing power of inclusive p–C scattering, $|p''_{x''y''}|$ and ϕ_p are the magnitude and azimuthal angle of polarization projected onto the $x''y''$-plane. The scattering asymmetry for the U and D regions indicated in Fig. 18 can be written as

$$\begin{aligned}
\mathrm{Asym} &= \frac{N_D - N_U}{N_D + N_U} \\
&= \frac{\int_D dN(\theta,\phi) - \int_U dN(\theta,\phi)}{\int_D dN(\theta,\phi) + \int_U dN(\theta,\phi)} \\
&= \frac{\int_D dN(\theta,\phi) - \int_D dN(\theta,\phi+180^\circ)}{\int_D dN(\theta,\phi) + \int_D dN(\theta,\phi+180^\circ)}.
\end{aligned} \tag{34}$$

where it is used in the last transformation that U and D regions are symmetrical around the origin.

$$\begin{aligned}
(\text{numerator of (34)}) &\propto \int_D \frac{d\sigma}{d\Omega}|p''_{x''y''}|A_y\{\sin(\phi-\phi_p) - \sin(\phi-\phi_p+180^\circ)\}d\Omega \\
&= 2\,|p''_{x''y''}|\int_D \frac{d\sigma}{d\Omega}A_y\sin(\phi-\phi_p)d\Omega \\
&= 2\,|p''_{x''y''}|\int_D \frac{d\sigma}{d\Omega}A_y(\sin\phi\cos\phi_p - \cos\phi\sin\phi_p)d\Omega
\end{aligned}$$

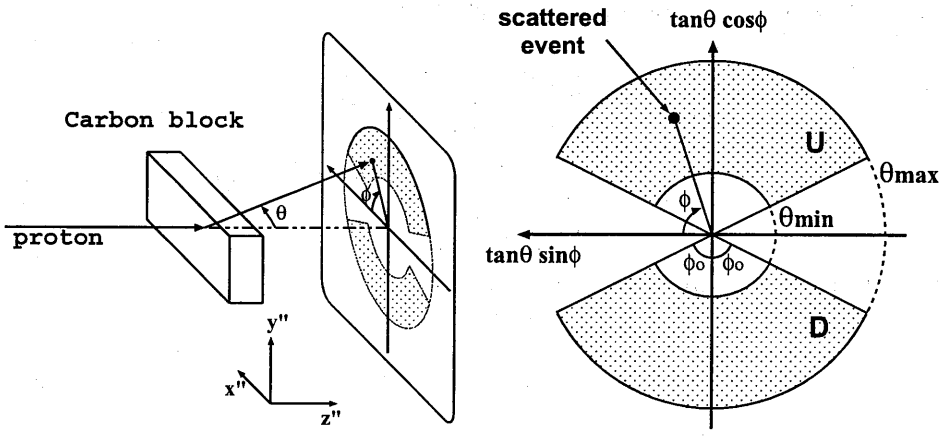

Figure 18: Coordinate system and integration regions in the analysis of scattering angles.

$$
\begin{aligned}
&= 2\,|p''_{x''y''}|\cos\phi_p \int_D \frac{d\sigma}{d\Omega} A_y \sin\phi\, d\Omega \\
&\quad -2\,|p''_{x''y''}|\sin\phi_p \int_D \frac{d\sigma}{d\Omega} A_y \cos\phi\, d\Omega \qquad (35) \\
&= 2\,p''_{x''} \int_D \frac{d\sigma}{d\Omega} A_y \sin\phi\, d\Omega, \qquad (36)
\end{aligned}
$$

where $p''_{x''} = |p''_{x''y''}|\cos\phi_p$ is the x'' component of proton polarization, the second term in (35) vanishes by the symmetry of the D region, and

$$
\begin{aligned}
\text{(denominator of (34))} \;&\propto \int_D \frac{d\sigma}{d\Omega}\{2 + |p_{xy}|A_y \\
&\quad \times[\sin(\phi-\phi_p) + \sin(\phi-\phi_p+180^\circ)]\}\, d\Omega \\
&= 2\int_D \frac{d\sigma}{d\Omega}\, d\Omega. \qquad (37)
\end{aligned}
$$

Then (34) reduces to a simple form as

$$
\text{Asym} = p''_{x''} \cdot \frac{\int_D \frac{d\sigma}{d\Omega} A_y \sin\phi\, d\Omega}{\int_D \frac{d\sigma}{d\Omega}\, d\Omega}. \qquad (38)
$$

Thus the x'' component of polarization of protons can be obtained as

$$
\begin{aligned}
p''_{x''} &= \left(\frac{\int_D \frac{d\sigma}{d\Omega} A_y \sin\phi\, d\Omega}{\int_D \frac{d\sigma}{d\Omega}\, d\Omega}\right)^{-1} \text{Asym} \\
&= \frac{1}{A_y^{\text{eff}}} \cdot \frac{N_D - N_U}{N_D + N_U}, \qquad (39)
\end{aligned}
$$

where the effective analyzing power $A_y^{\rm eff}$ is defined as

$$\begin{aligned} A_y^{\rm eff} &\equiv \frac{\int_D \frac{d\sigma}{d\Omega}(\theta) A_y(\theta) \sin\phi \, d\Omega}{\int_D \frac{d\sigma}{d\Omega}(\theta) \, d\Omega} \\ &= \frac{\int_{\theta_{min}}^{\theta_{max}} \frac{d\sigma}{d\Omega}(\theta) A_y(\theta) \sin\theta \, d\theta}{\int_{\theta_{min}}^{\theta_{max}} \frac{d\sigma}{d\Omega}(\theta) \sin\theta \, d\theta} \cdot \frac{\sin\phi_0}{\phi_0}. \end{aligned} \tag{40}$$

Similarly the y'' component of polarization becomes

$$p''_{y''} = \frac{1}{A_y^{\rm eff}} \cdot \frac{N_L - N_R}{N_L + N_R}. \tag{41}$$

Typical $\phi_{\rm FPP}$ spectra are displayed in Fig. 19. N_U and N_D are obtained by integrations of the hatched U and D regions, respectively. Asymmetries between U and D regions can be seen clearly. The dependency on the beam spin modes is also obvious.

The boundaries of the integration region, defined by ϕ_0, θ_{min} and θ_{max}, were determined to maximize the figure of merit (FoM) defined as[32]

$$\text{FoM} \equiv \eta (A_y^{\rm eff})^2. \tag{42}$$

The efficiency of the FPP η becomes

$$\begin{aligned} \eta &\equiv \frac{\text{number of analyzed events}}{\text{number of total events}} \\ &\propto \frac{N_D + N_U}{\int \frac{d\sigma}{d\Omega} \, d\Omega} \\ &= \frac{2 \int_D \frac{d\sigma}{d\Omega} \, d\Omega}{\sigma} \\ &\propto \int_D \frac{d\sigma}{d\Omega} \, d\Omega. \end{aligned} \tag{43}$$

Substitution of (40) and (43) into (42) yields

$$\begin{aligned} \text{FoM} &\propto \int_D \frac{d\sigma}{d\Omega} \, d\Omega \cdot \left(\frac{\int_D \frac{d\sigma}{d\Omega} A_y \sin\phi \, d\Omega}{\int_D \frac{d\sigma}{d\Omega} \, d\Omega} \right)^2 \\ &= \frac{(\int_{\theta_{min}}^{\theta_{max}} \frac{d\sigma}{d\Omega} A_y \sin\theta d\theta)^2}{\int_{\theta_{min}}^{\theta_{max}} \frac{d\sigma}{d\Omega} \sin\theta d\theta} \cdot \frac{2\sin^2\phi_0}{\phi_0}. \end{aligned} \tag{44}$$

The FoM takes the maximum at $\phi_0 \simeq 66.8°$ which is the solution of

$$\tan\phi_0 = 2\phi_0, \tag{45}$$

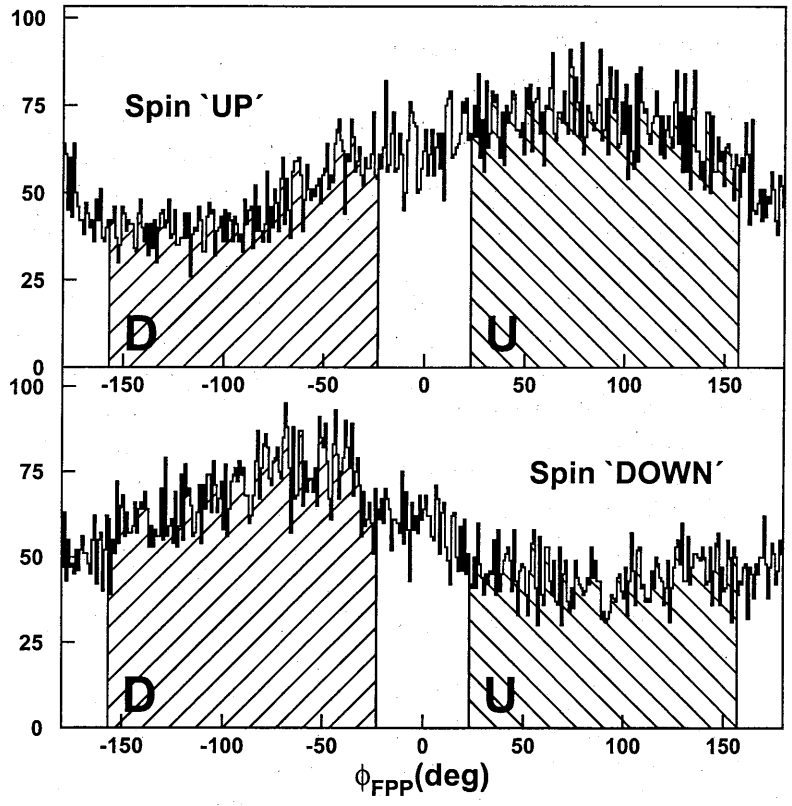

Figure 19: Typical ϕ_{FPP} spectra in both beam spin modes are displayed. Hatched regions indicate U and D regions, respectively. Clear scattering asymmetries and dependency on the beam spin modes can be seen.

Table 5: Summary of parameters for $A_y^{\rm eff}$ estimation.

beam energy	200 MeV	300 MeV	400 MeV
energy in C-block	182 MeV	269 MeV	363 MeV
ϕ_0	66.8°	66.8°	66.8°
θ range	$5.0 - 21.0°$	$5.0 - 20.7°$	$5.0 - 19.1°$
$A_y^{\rm eff}$	0.397 ± 0.012	0.391 ± 0.012	0.317 ± 0.010

whereas the most desirable θ range depends on angular distributions of $d\sigma/d\Omega$ and A_y of inclusive p–C scattering.

In order to determine the θ range and $A_y^{\rm eff}$ value, the following procedures were performed. The angular distribution of the differential cross section was obtained from the data of $\theta_{\rm FPP}$ distribution of the scattering in the carbon block measured in this experiment since $d\sigma/d\Omega(\theta)\sin\theta$ in (40) is proportional to the $\theta_{\rm FPP}$ distribution.

A_y was estimated by using the empirical energy dependent fit by McNaughton *et al.*[33]. The energy of protons in the carbon block was represented by the energy at the block center. The energy losses in traveling the half thicknesses of the carbon block were obtained from the well-known Bethe-Bloch formula[31]. The results were 18 MeV, 31 MeV and 37 MeV for the beam energies of 200 MeV, 300 MeV and 400 MeV, respectively. Energy differences of incoming protons according to the scattering angle were small compared to above energy losses. θ_{min} was fixed at 5° for all energies and θ_{max} were searched to maximize the FoM. The searched results were 21.0°, 20.7° and 19.1° for 200 MeV, 300 MeV and 400 MeV. Corresponding $A_y^{\rm eff}$ were 0.397, 0.391 and 0.317, respectively. Figure 20 shows the FoM and $A_y^{\rm eff}$ as functions of θ_{max} for 300 MeV case. These results are summarized in Table 5. We have also directly measured single scattering in the carbon block of a polarized faint proton beam at several beam energies and for various carbon thicknesses[34] to calibrate $A_y^{\rm eff}$ and found that the angle averaged effective analyzing powers estimated by the McNaughton formula have been agreed with the experimental results within approximately 3%. Thus systematic 3% errors are introduced in Table 5.

The root mean square angular spreading due to the Coulomb multiple scattering in the carbon block was estimated in the Gaussian approximation as[35]

$$\theta_{\rm rms}({\rm rad.}) = \frac{13.6\,({\rm MeV})}{\beta cp} z\sqrt{x/X_0}\,[1 + 0.038\ln(x/X_0)]\,, \qquad (46)$$

where p, βc and z are the momentum, velocity and charge number of the

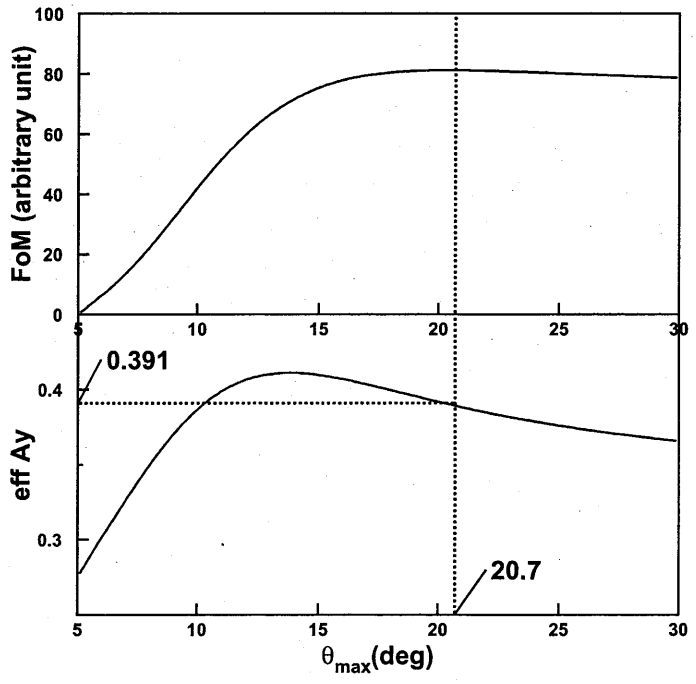

Figure 20: The FoM and A_y^{eff} are displayed as functions of θ_{max} for 300 MeV case. The FoM takes maximum at 20.7°, where A_y^{eff} becomes 0.3909.

incident particle, and x/X_0 is the thickness of the scattering medium in radiation lengths. The results were 0.93°, 0.99° and 0.90° for 200, 300 and 400 MeV beam, respectively.

3.5 Cross sections and analyzing powers

Vertically polarized beam ($p_x, p_z \sim 0$) was used for cross section and analyzing power measurements. The FPP was not used in this measurement.

Number of elastically scattered protons detected with the standard counters can be expressed as

$$N_{\uparrow(\downarrow)} = \frac{d\sigma}{d\Omega}\left(1 + p_{y\uparrow(\downarrow)} A_y\right) Q_{\uparrow(\downarrow)} \Omega x \varepsilon_{\uparrow(\downarrow)} \ell_{\uparrow(\downarrow)}, \tag{47}$$

where $\uparrow$ ($\downarrow$) represents the spin direction of the beam, $p_y, Q, \Omega, x, \varepsilon, \ell$ are the y component of beam polarization, number of protons in the beam, solid angle of the spectrometer defined by the slit which was ± 20 mrad wide and ± 30 mrad high, number of the target nuclei in unit area, total efficiency of the VDC's and the live-time of the DAQ system estimated by the accepted event number ratio to the requested event number, respectively. Cross sections and analyzing powers can be deduced by solving the simultaneous equations (47);

$$\frac{d\sigma}{d\Omega} = \frac{1}{p_{y\uparrow} - p_{y\downarrow}} \left(\frac{N_\downarrow p_{y\uparrow}}{Q_\downarrow \varepsilon_\downarrow \ell_\downarrow} - \frac{N_\uparrow p_{y\downarrow}}{Q_\uparrow \varepsilon_\uparrow \ell_\uparrow} \right) \frac{1}{\Omega x}, \tag{48}$$

$$A_y = \frac{1-\alpha}{\alpha p_{y\uparrow} - p_{y\downarrow}}, \tag{49}$$

where

$$\alpha = \frac{N_\downarrow}{Q_\downarrow \varepsilon_\downarrow \ell_\downarrow} \Big/ \frac{N_\uparrow}{Q_\uparrow \varepsilon_\uparrow \ell_\uparrow}. \tag{50}$$

Note that $p_{y\downarrow}$ is a negative value, thus $d\sigma/d\Omega$ becomes positive definite. Statistical errors can be estimated as

$$\begin{aligned} \Delta\frac{d\sigma}{d\Omega} = {} & \frac{d\sigma}{d\Omega} \cdot \frac{1}{p_{y\uparrow} - p_{y\downarrow}} \cdot \frac{1}{\alpha p_{y\uparrow} - p_{y\downarrow}} \\ & \times \Big\{ (1-\alpha)^2 [(p_{y\downarrow} \Delta p_{y\uparrow})^2 + (p_{y\uparrow} \Delta p_{y\downarrow})^2] \\ & + (p_{y\uparrow} - p_{y\downarrow})^2 \left(\frac{p_{y\downarrow}^2}{N_\uparrow} + \frac{\alpha^2 p_{y\uparrow}^2}{N_\downarrow} \right) \Big\}^{1/2}, \end{aligned} \tag{51}$$

$$\Delta A_y = \frac{1}{(\alpha p_{y\uparrow} - p_{y\downarrow})^2} \Big\{ (1-\alpha)^2 (\alpha^2 \Delta p_{y\uparrow}^2 + \Delta p_{y\downarrow})$$

$$+ \alpha^2 (p_{y\uparrow} - p_{y\downarrow})^2 \left(\frac{1}{N_\uparrow} + \frac{1}{N_\downarrow} \right) \Bigg\}^{1/2} . \quad (52)$$

3.6 Spin rotation parameters

Horizontally polarized beam ($p_y \sim 0$) was employed in the measurement of spin rotation parameters.

In the proton elastic scattering from spin 0 nuclei, proton polarization vector after the scattering can be expressed as

$$\begin{pmatrix} p'_{x'} \\ p'_{y'} \\ p'_{z'} \end{pmatrix} = \frac{1}{1 + p_y A_y} \begin{pmatrix} p_x R + p_z A \\ A_y + p_y \\ -p_x A + p_z R \end{pmatrix}, \quad (53)$$

where $p_{x,y,z}$ are beam polarizations, A_y is the analyzing power of the target obtained by the vertically polarized beam measurements described above, and R and A are Wolfenstein's parameters[36]. Due to the spin precession in the dipole magnetic fields of the Grand Raiden, polarization vector at the FPP becomes

$$\begin{pmatrix} p''_{x''} \\ p''_{y''} \\ p''_{z''} \end{pmatrix} = \begin{pmatrix} \cos\chi_{\rm GR} & 0 & \sin\chi_{\rm GR} \\ 0 & 1 & 0 \\ -\sin\chi_{\rm GR} & 0 & \cos\chi_{\rm GR} \end{pmatrix} \begin{pmatrix} p'_{x'} \\ p'_{y'} \\ p'_{z'} \end{pmatrix}. \quad (54)$$

Here $\chi_{\rm GR}$ is the precession angle obtained by the general expression of (15) with $\chi_L = 162 + 18°$ or $162 - 17°$ for DSR$\pm$ modes. Thus the polarization $p''_{x''}$ of scattered protons along the x'' axis measured with the FPP are represented by

$$p^{''\pm}_{x''\uparrow(\downarrow)} = \frac{1}{1 + p^{\pm}_{y\uparrow(\downarrow)} A_y} \Big[\left(p^{\pm}_{x\uparrow(\downarrow)} \cos\chi^{\pm}_{\rm GR} + p^{\pm}_{z\uparrow(\downarrow)} \sin\chi^{\pm}_{\rm GR} \right) R + \left(p^{\pm}_{z\uparrow(\downarrow)} \cos\chi^{\pm}_{\rm GR} - p^{\pm}_{x\uparrow(\downarrow)} \sin\chi^{\pm}_{\rm GR} \right) A \Big], \quad (55)$$

where $\uparrow$ ($\downarrow$) denotes the spin mode of the ion source, $\pm$ indicates the polarity of the DSR mode. $p^{''\pm}_{x''\uparrow(\downarrow)}$ were obtained from the measurements of scattering asymmetries at the FPP as (39). It can be seen that $p^{''\pm}_{x''\uparrow}$ and $p^{''\pm}_{x''\downarrow}$ had almost the same magnitude with the opposite sign since the term $p^{\pm}_{y\uparrow(\downarrow)} A_y$ in the denominator were small in the horizontally polarized beam and p_x, p_z changed the sign according to the spin mode of the beam. Thus it was statistically profitable to add $p^{''\pm}_{x''\uparrow}$ and $p^{''\pm}_{x''\downarrow}$ in the opposite sign;

$$(1 + p^{\pm}_{y\uparrow} A_y) p^{''\pm}_{x''\uparrow} - (1 + p^{\pm}_{y\downarrow} A_y) p^{''\pm}_{x''\downarrow}$$

$$= \left\{ \left[(p^{\pm}_{x\uparrow} - p^{\pm}_{x\downarrow}) \cos\chi^{\pm} + (p^{\pm}_{z\uparrow} - p^{\pm}_{z\downarrow}) \sin\chi^{\pm} \right] R \right.$$
$$\left. + \left[(p^{\pm}_{z\uparrow} - p^{\pm}_{z\downarrow}) \cos\chi^{\pm} - (p^{\pm}_{x\uparrow} - p^{\pm}_{x\downarrow}) \sin\chi^{\pm} \right] A \right\}. \quad (56)$$

R and A parameters were obtained by solving simultaneous equations (56). Spin rotation parameters Q can be obtained from the R and A parameters as

$$Q = R\sin(\theta_{\rm LAB} + \varepsilon) + A\cos(\theta_{\rm LAB} + \varepsilon), \quad (57)$$

where $\theta_{\rm LAB}$ is the scattering angle in laboratory frame. ε is a small relativistic correction which comes from the intrinsic coordinate axis rotation due to the successive Lorentz transformations in different directions[37] and expressed as

$$\sin\frac{\varepsilon}{2} = \left[\frac{(\gamma_1 - 1)(\gamma_2 - 1)}{2(\gamma_0 + 1)} \right]^{\frac{1}{2}} \sin\theta_{\rm LAB}, \quad (58)$$

with

$$\gamma_0 = \frac{T^{out}_{p\,({\rm CM})} + m_p c^2}{m_p c^2}, \quad (59)$$

$$\gamma_1 = \frac{T^{out}_{p\,({\rm LAB})} + m_p c^2}{m_p c^2}, \quad (60)$$

$$\gamma_2 = \frac{T^{in}_{p\,({\rm LAB})} + m_p c^2 + Mc^2}{\sqrt{s}}, \quad (61)$$

$$s = (m_p c^2 + Mc^2)^2 + 2Mc^2 T^{in}_{p\,({\rm LAB})}, \quad (62)$$

where $m_p c^2$ and Mc^2 are the rest energies of proton and target nucleus, T^{in}_p and T^{out}_p are kinetic energies of incoming and outgoing protons.

There are several methods to deduce the statistical uncertainties of Q parameters (ΔQ). The usual error propagation method may not be good since the contribution of higher order terms in the Taylor expansions may not be negligible. Thus the ΔQ were estimated by a Monte-Carlo method. Each quantity was changed randomly so as to be the normal distribution with its mean and standard deviation, Q was calculated with new random values. The resulting Q distribution was fitted with a Gaussian and its standard deviation σ was considered as ΔQ.

Experimental results of cross sections, analyzing powers and spin rotation parameters are shown in next section together with the various model calculations. Digital data are summarized in Appendix A.

4 Discussion

Nucleon–nucleon (NN) interactions in nuclear medium and ground state wave functions of the targets are basic ingredients for analyzing proton elastic scattering. As for the interactions, impulse approximations have successfully explained proton elastic scattering at intermediate energy regions, especially for polarization observables. In these models the interaction between the projectile and target nucleons is assumed to be the same form as the interaction between two nucleons in free space. This approximation also implies that the scattering is dominated by single collision process, thus it is expected to be appropriate for scattering at intermediate energies where the elementary NN cross section reaches its minimum.

Point proton distributions in nuclei have relatively small uncertainties since they are restricted by nuclear charge distributions obtained from electron scattering, if available. Contrastingly, it is hard to extract point neutron distributions from charge distributions. For $Z \simeq N$ nuclei, however, neutron distribution is expected to have the same shape as the proton distribution except for the normalization factor due to the charge independent property of nuclear forces. For $Z \neq N$ nuclei, such assumption may not be a good approximation. Neutron distributions are still unknown parameters in this case. Neutron distributions in nuclei can be searched so as to reproduce proton elastic scattering data, if we know the NN force inside the nucleus.

In this section, in order to focus the problem on the interactions, analysis on ^{58}Ni ($Z \simeq N$ nucleus) is discussed first. Modifications to the NN interactions are introduced by changing coupling constants and masses of exchanged mesons. Then, the modified NN interactions are applied to ^{120}Sn ($Z \neq N$ nucleus) to extract neutron distribution.

4.1 Original impulse approximation

Our experimental results of ^{58}Ni are plotted as solid circles in Fig. 21, 22. First of all we compare our results with the predictions of three types of impulse approximation models. Solid curves in the figures represent relativistic impulse approximation (RIA) calculations of Murdock and Horowitz[4] (MH) with the Pauli-blocking effect correction. In this model the experimental NN amplitudes are represented by a standard set of five Lorentz covariants as (79) in Appendix B, then they are folded with nuclear densities to produce a first order "$t\rho$" optical potential for use in a Dirac equation. Details of the MH model are reviewed in Appendix B. The density distributions of ^{58}Ni are obtained using the relativistic Hartree (RH) approximation[38, 39]. Although the MH model well reproduce polarization observables, the cross sections are

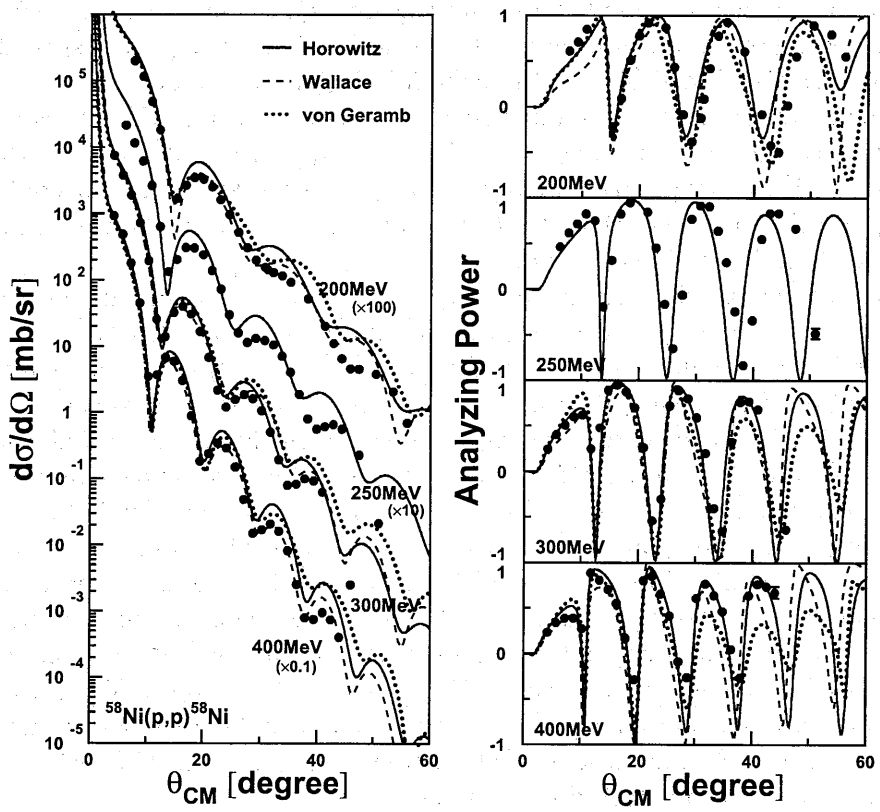

Figure 21: The experimental data of cross sections and analyzing powers of proton elastic scattering from ^{58}Ni at 200, 250, 300 and 400 MeV indicated by solid circles are compared to original (unmodified) impulse approximation models. Solid curves and dashed curves indicate the relativistic impulse approximations of Horowitz *et al.* and Wallace *et al.*, respectively. Dotted curves represent the nonrelativistic microscopic optical potential calculations using the G matrix of von Geramb. Note that calculations of Wallace and von Geramb models are not performed at 250 MeV. None of these models satisfactorily explain the experimental data, especially angular distributions of cross sections.

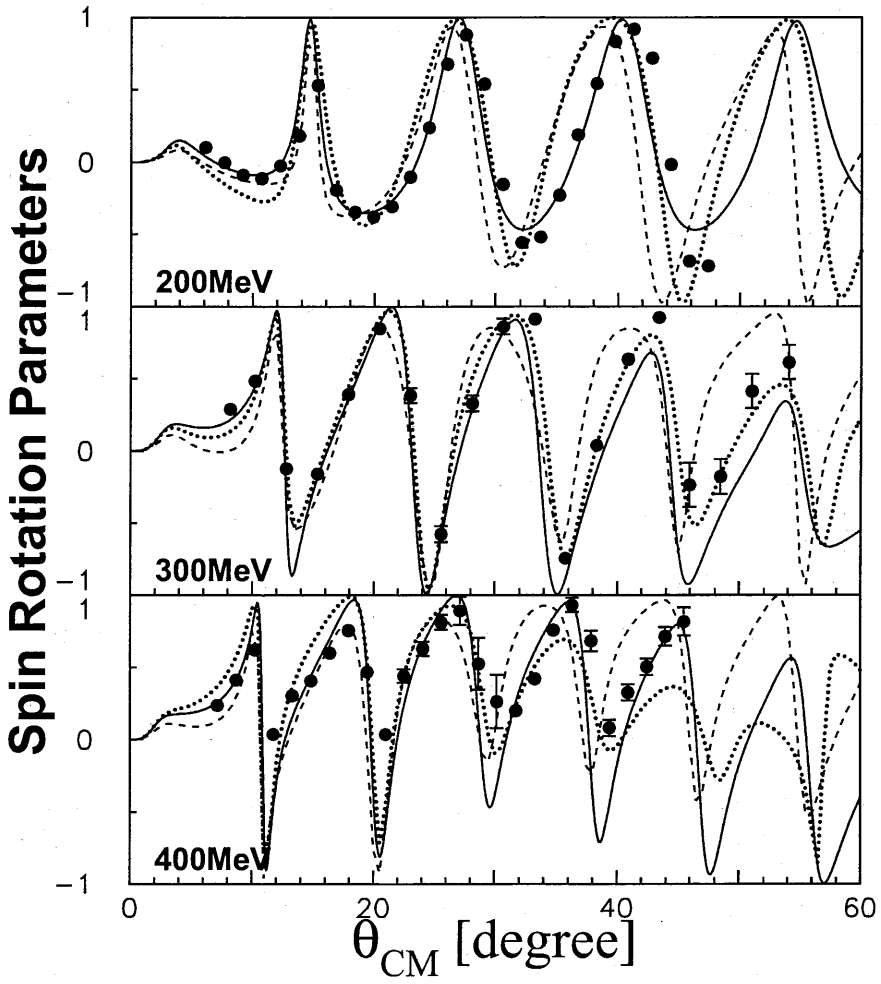

Figure 22: Same as Fig. 21, but for spin rotation parameters.

poorly reproduced, especially for backward scattering angles. Since the cross sections at forward angles, where the Rutherford scattering is the dominant mechanism, are reproduced quite well, the ambiguity in the absolute value of the cross section is small.

Same feature is found in another RIA model of Tjon and Wallace[6] (IA2), in which a complete set of Lorentz invariant NN amplitudes are taken into account, as denoted by dashed curves in the same figures. For comparison, nonrelativistic impulse approximation calculations are also plotted as dotted curves. The nonrelativistic Schrödinger optical potentials are calculated using the G matrix of von Geramb[40] following the procedure of Rikus and von Geramb[41]. Overestimation of the cross sections at backward angles can be found also in this model. Although the nonrelativistic calculation explains the experiments at 200 MeV fairly well, deviation between the prediction and the data increases as energy increases. In particular, this deviation is serious in analyzing powers at 400 MeV. In summary none of the three impulse approximation models listed here can satisfactorily explain the experimental data.

4.2 Realistic density distributions

From now on, modifications to the MH model are discussed. In the analysis given in Ref. [8] of cross sections and analyzing powers, to account for the experimental data it has been necessary to use realistic densities of the target nuclei and to modify the coupling constants between nucleons and mesons and the masses of exchanged mesons in the NN interaction as a medium effect.

The realistic densities are obtained as follows. Nuclear charge distributions of various target nuclei have been extracted from electron elastic scattering[42]. A considerable number of parameterizations are available in Ref. [43]. In principle we should consider the contributions from magnetic moments of protons and neutrons, meson exchange currents and other effects, though we expect the dominant contribution to the nuclear charge distribution comes from the intrinsic proton charge distribution. The nuclear charge distribution can be approximated by convolution of the point proton distribution and the intrinsic proton charge distribution, as expressed in (94). The contribution from the intrinsic proton charge distribution can be unfolded as (96), thus the point proton distribution is obtained. In the previous work[8] the root mean square radius of the intrinsic proton charge distribution, which was needed in (99), has been assumed to be 0.80 fm according to Ref. [44], while in this work it was assumed to be 0.875 ± 0.022 fm from recent analyses of the proton charge radius with two-loop binding ef-

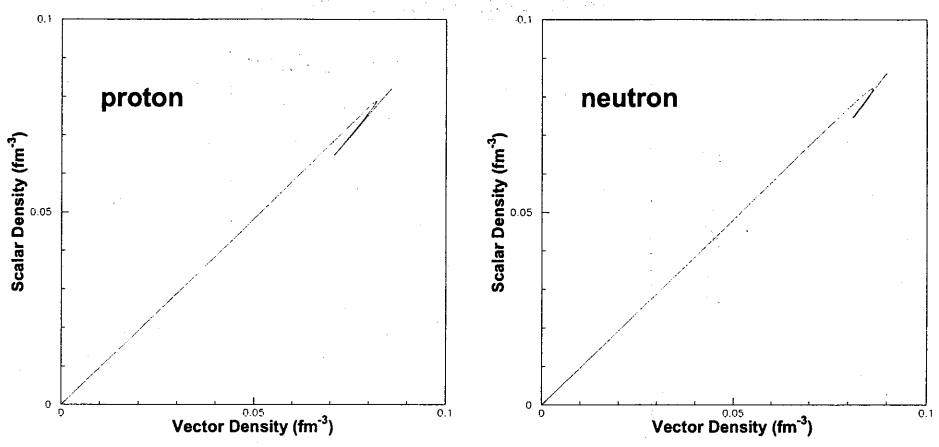

Figure 23: The RH scalar densities are compared with the RH vector densities for the ^{58}Ni nucleus. Left and right parts of the figure show the comparisons of proton and neutron, respectively. It can be seen that the ratio of the scalar densities to the vector densities are almost constant.

fects in the QED calculations[45]. We assume that the proton charge radius is unchanged in the target nucleus. In general unfolding procedure requires numerical integration to perform inverse Fourier transform, though it can be carried out analytically if a sum of Gaussians (SOG) type of nuclear charge distribution is chosen. See Appendix C for details. In this analysis we use the SOG charge distribution of ^{58}Ni from Ref. [43] and calculate the point proton distribution $\rho_p^V(r)$.

The point neutron distribution cannot be obtained from the charge distribution according to the procedure above. However, it can be assumed for $Z \simeq N$ nuclei that it has the same shape as the point proton distribution except for the normalization factor of the volume integral, because of the charge independence property of nuclear forces which form the nucleus. Thus

$$\rho_n^V(r) = \frac{N}{Z}\rho_p^V(r), \tag{63}$$

where $Z = 28$ and $N = 30$ are the numbers of protons and neutrons in the ^{58}Ni nucleus, respectively. In the RIA formalism another type of density distributions, scalar density distributions ρ^S for both proton and neutron, are needed. According to the RH calculation with the computer code by Horowitz *et al.*[38], the ratio of the scalar density to the vector density for ^{58}Ni is almost constant as shown in Fig. 23. Although in light nuclei the

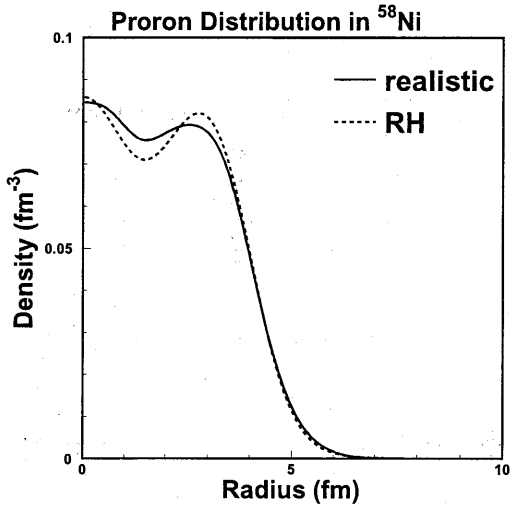

Figure 24: The realistic proton distribution (solid curve) deduced from the charge density is compared with the prediction by the relativistic Hartree (RH) calculation (dashed curve).

RH calculation predicts scalar to vector ratios slightly changed, in nuclei heavier than ^{40}Ca they are almost independent of the nuclei and the value is approximately 0.96. Thus by partially using the results of the RH calculation it is assumed that the scalar distributions have the same shapes as the vector distributions;

$$\rho^S_{p,n}(r) = R_{SV}\rho^V_{p,n}(r), \tag{64}$$

where $R_{SV} = 0.96$. Thus all target density distributions needed in the RIA calculation can be expressed by the point proton distribution $\rho^V_p(r)$ deduced from the target nuclear charge distribution. The obtained realistic proton distribution is shown in Fig. 24 by the solid curve. In comparison with the RH distribution denoted by the dashed curve, the oscillatory behavior at the nuclear center is moderate.

As shown in Fig 25, 26, the obtained realistic density distributions remarkably improve the fits to the cross section data, while the quality of the fitting for polarization observables are preserved. However, there are still discrepancies between the data and the calculations. The Pauli-blocking effect is already included in both calculations in Fig 25, 26, thus these deviations cannot be attributed to the Pauli-blocking only.

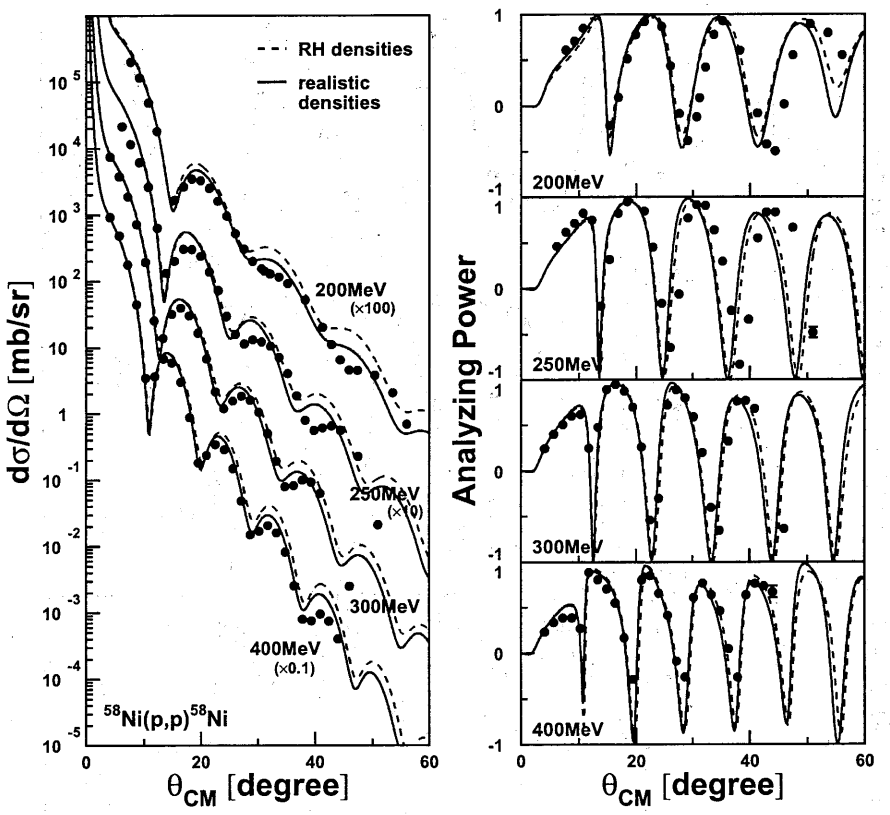

Figure 25: Experimental data and the RIA calculations with the RH densities (dashed curves) and the realistic densities (solid curves) for cross sections and analyzing powers of proton elastic scattering from ^{58}Ni at $E_p = 200$, 250, 300 and 400 MeV. The fits to the data are meaningfully improved, especially for cross sections, if the realistic densities are used.

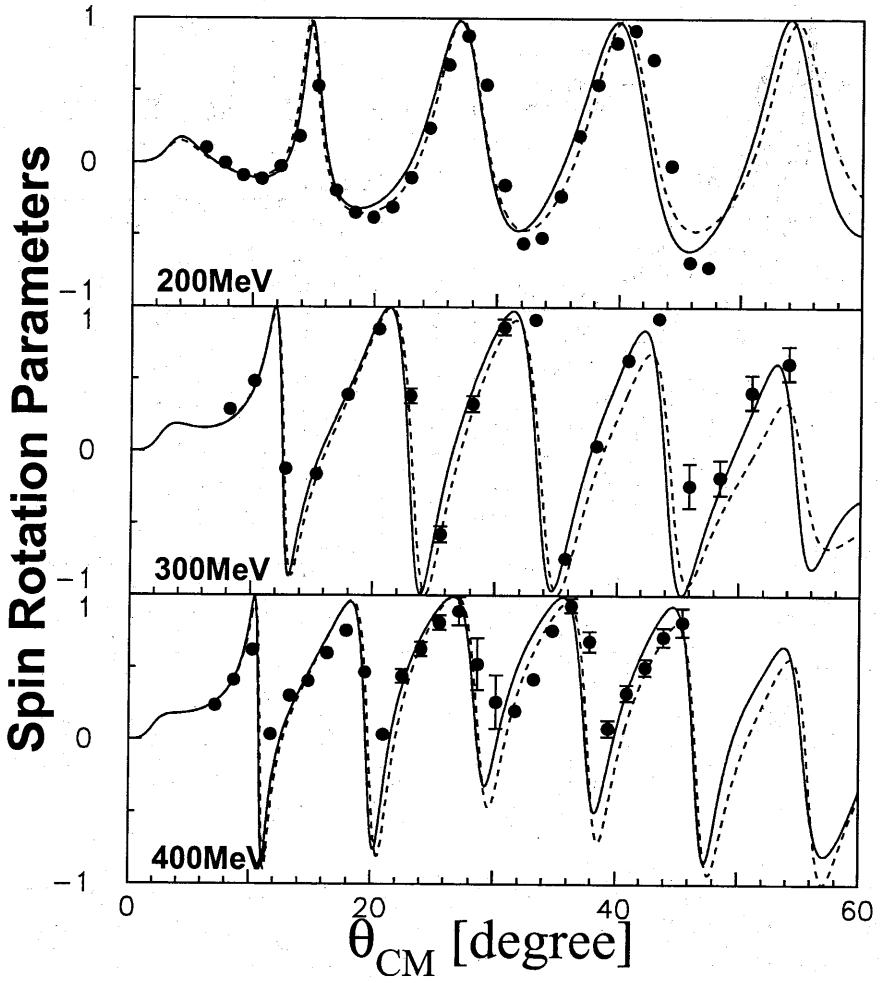

Figure 26: Same as Fig. 25, but for spin rotation parameters.

4.3 Medium modified *NN* interactions

In order to improve the fits to the experimental data, coupling constants and masses of σ and ω mesons in the *NN* scattering amplitude (83) in the MH model are modified as follows;

$$g_j^2 \rightarrow g_j^{*2} = \frac{g_j^2}{1 + a_j\,\rho(r)/\rho_0}, \tag{65}$$

$$\bar{g}_j^2 \rightarrow \bar{g}_j^{*2} = \frac{\bar{g}_j^2}{1 + \bar{a}_j\,\rho(r)/\rho_0}, \tag{66}$$

$$m_j \rightarrow m_j^* = m_j\,(1 + b_j\,\rho(r)/\rho_0)\,, \tag{67}$$

$$\bar{m}_j \rightarrow \bar{m}_j^* = \bar{m}_j\,(1 + \bar{b}_j\,\rho(r)/\rho_0)\,, \tag{68}$$

where j refers to the σ or ω mesons and $\rho_0 = 0.1934\,\mathrm{fm}^{-3}$ stands for the normal density. In the free space, where the density $\rho(r)$ of the target is zero, the coupling constants and masses of mesons are identical to those of the free *NN* interaction, but inside the nucleus the modification is assumed to be proportional to the nucleon density. If we express various nuclear many-body effects in terms of the nuclear density, which is assumed to be small for a normal nucleus, we can obtain a lowest order approximation of the influence of this density by retaining only the effects that are first order in this parameter. Effects on higher order Dirac potentials and uncertainty in selecting the ratio of the scalar densities to the vector densities R_{SV} in (64) are effectively taken into account in the above parameters.

Although many other mesons contribute to real *NN* interactions, it is well known that contributions from mesons other than the isoscalar σ and ω are negligible for elastic scattering from $N \simeq Z$ nuclei; in other words, we can find the medium effect on σ and ω mesons by studying elastic scattering from $N \simeq Z$ nuclei.

By using the same parameter values as obtained in our previous work[8], the spin rotation parameters Q are calculated. These are represented by the solid curves in Fig. 27. By comparing with the MH model of dashed curves and the IA2 model of dotted curves, this figure indicates that the RIA calculations involving the medium effects can also reproduce the newly measured Q parameters well except those at backward angles of 400 MeV. The reaction mechanism becomes complicated at higher energies since inelastic processes such as pion productions contribute much more, thus it is difficult for model calculations to agree with experimental data at 400 MeV. Except for 400 MeV it is concluded that the medium effect model satisfactorily reproduces all of the observables: differential cross sections, analyzing powers and spin rotation parameters. Thus the predictability of this model

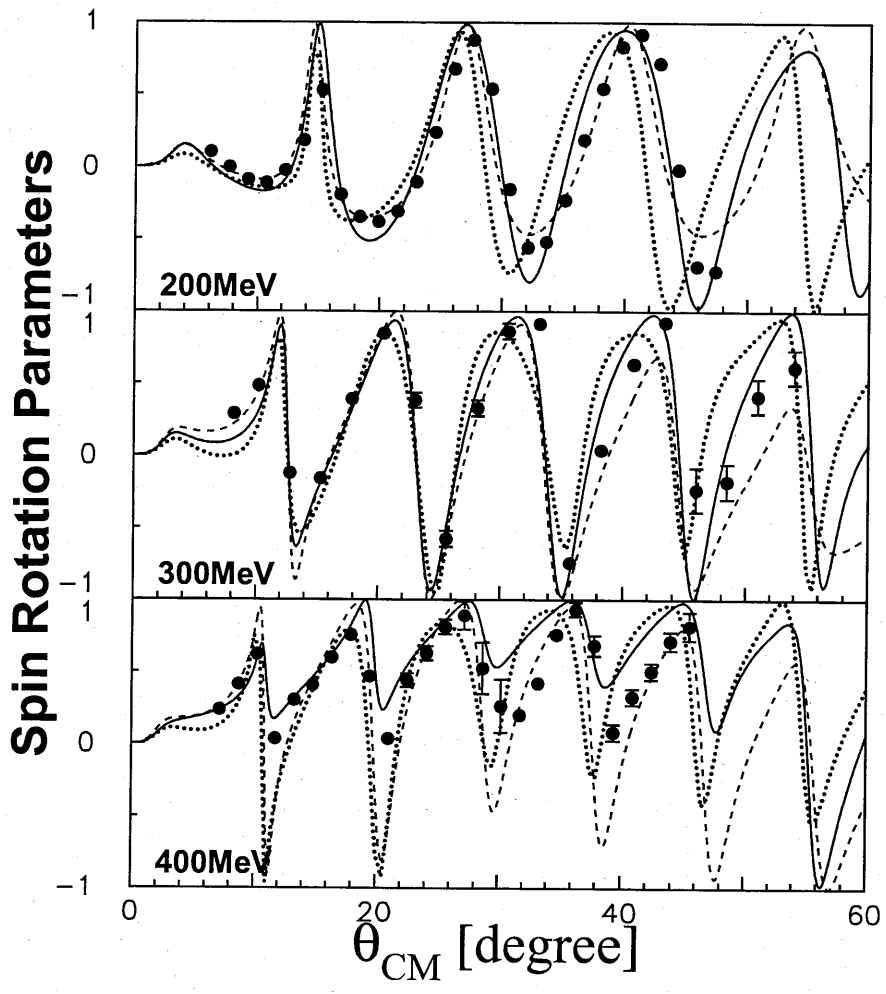

Figure 27: Spin rotation parameters of proton elastic scattering from ^{58}Ni at E_p = 200, 300 and 400 MeV. Solid curves are the medium modified RIA calculations with parameters taken from Ref. [8], Dashed and dotted curves represent the original RIA by Horowitz and the IA2 by Wallace, respectively.

Table 6: Best fit medium modification parameters with newly measured spin rotation parameters included.

energy	200 MeV	300 MeV	400 MeV
a_σ	0.0587	0.4499	0.4841
$\bar{a}_\sigma$	0.3994	−0.1349	0.5319
a_ω	0.4464	1.1481	1.1512
$\bar{a}_\omega$	0.6797	0.4255	0.6735
b_σ	0.0840	−0.1059	−0.1118
$\bar{b}_\sigma$	0.1147	−0.1794	0.1159
b_ω	−0.0453	−0.2615	−0.2879
$\bar{b}_\omega$	−0.0391	−0.2863	−0.0916
χ^2	2655	1668	1352

is confirmed.

Reliability of the medium modification parameters would be improved by performing the fine tuning with newly measured spin rotation parameters included. The reliable *NN* interactions in nuclear medium are also indispensable to extract a neutron distribution in next subsection. For each energy the parameters are searched to minimize χ^2. Search results are summarized in Table 6. The modified RIA calculations using the best fit parameters are displayed in Fig. 28, 29. Solid curves represent the best fit results, while dotted curves are the original MH calculations and dashed curves are same but the target density distributions are replaced by the realistic ones described in the previous subsection.

In order to investigate the correlations among $a_j, \bar{a}_j, b_j$ and $\bar{b}_j$ parameters, and also to confirm whether there exist other local minima or not, χ^2-map for every pair of parameters around the values at the best fit parameters are checked, with the other parameters fixed. Figure 30 shows the χ^2-map in (b_σ, b_ω) space for 300 MeV as an example. Very strong correlation between b_σ and b_ω is indicated by a narrow valley. This strong correlation is commonly found in other energies and also in $(\bar{b}_\sigma, \bar{b}_\omega)$ space. Not only mass parameters but also coupling constant modification parameters have similar correlations as shown in Fig. 31. These correlations correspond to our previous finding in Ref. [8]; it has been found that in order to maintain the quality of the fits to polarization observables, we have needed to keep the ratio of the scalar field to the vector field constant.

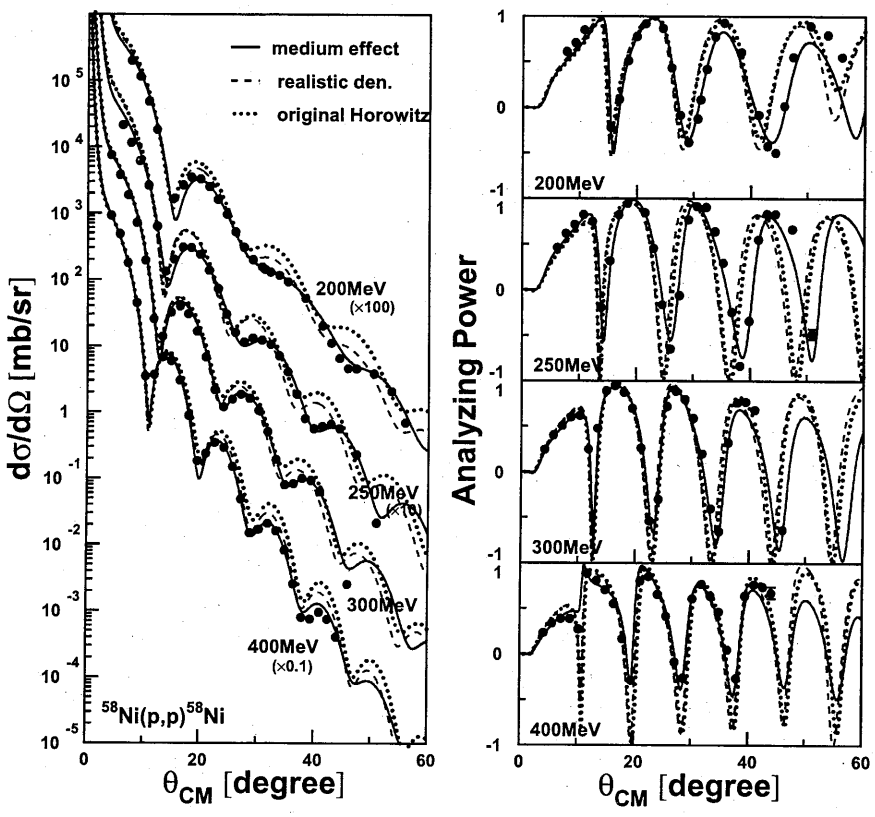

Figure 28: Cross sections and analyzing powers of proton elastic scattering from ^{58}Ni at E_p = 200, 250, 300 and 400 MeV. Solid curves represent the best fit results, while dotted curves are the original MH calculations and dashed curves are same but the target density distributions are replaced by the realistic ones.

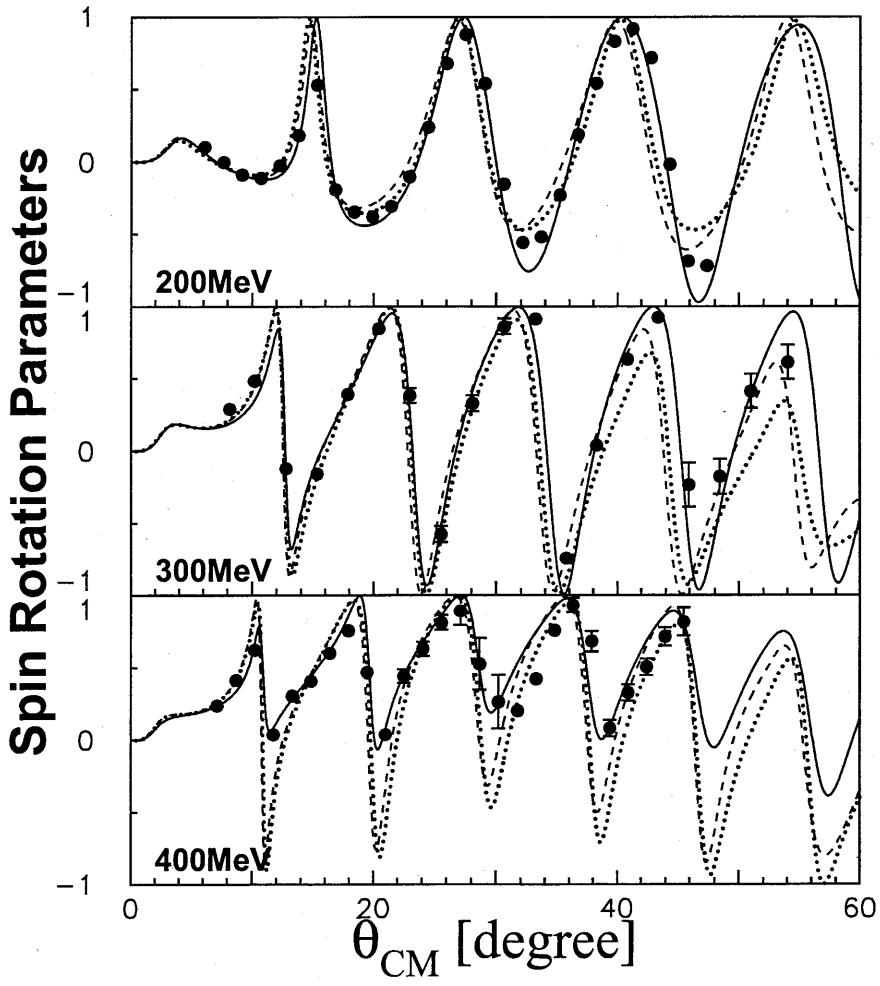

Figure 29: Same as Fig. 28, but for spin rotation parameters.

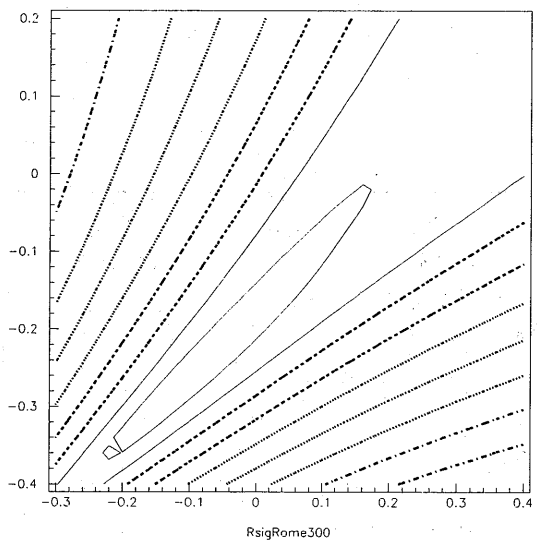

Figure 30: χ^2-map in (b_σ, b_ω) space for 300 MeV

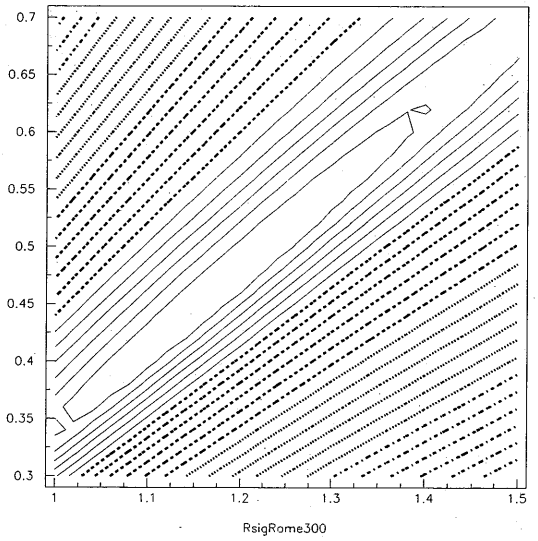

Figure 31: χ^2-map in (a_σ, a_ω) space for 300 MeV

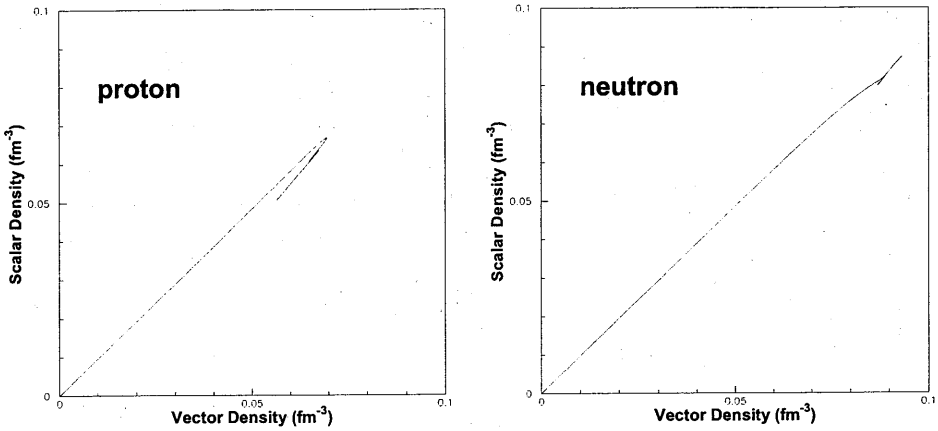

Figure 32: The RH scalar densities are compared with the RH vector densities for the ^{120}Sn nucleus. Left and right parts of the figure show the comparisons of proton and neutron, respectively. Similar to the ^{58}Ni case, it can be seen that the ratio of the scalar densities to the vector densities are almost constant.

4.4 Neutron distribution search

For $N \neq Z$ nuclei such as ^{120}Sn it cannot be expected that neutron distributions have the same shape as protons since the occupied single particle orbits are different. However, the elastic scattering is sensitive to both NN interactions in nuclear medium and density distributions of a target nucleus, neutron density distribution is expected to be extracted from the elastic scattering, by assuming the same medium modifications determined by the ^{58}Ni data and by using point proton proton distributions obtained from charge distributions. Since the SOG parameters of the nuclear charge distribution for ^{120}Sn are not available in Ref. [43], it is assumed to be an average between ^{116}Sn and ^{124}Sn;

$$\rho^{ch}_{^{120}\mathrm{Sn}}(r) = \frac{1}{2}\left[\rho^{ch}_{^{116}\mathrm{Sn}}(r) + \rho^{ch}_{^{124}\mathrm{Sn}}(r)\right]. \tag{69}$$

Using this charge distribution, vector and scalar proton distributions are deduced by the same procedure described in Sec. 4.2, where R_{SV} is also fixed to be 0.96, according to the results of RH calculations as shown in Fig. 32.

Before starting the neutron search, the following distribution is used as the first trial;

$$\rho^0_n(r) = \rho^{\mathrm{elec}}_p(r) + \left[\rho^{\mathrm{RH}}_n(r) - \rho^{\mathrm{RH}}_p(r)\right], \tag{70}$$

where $\rho_p^{\rm elec}$ is the point proton distribution deduced from the charge distribution of (69), $\rho_n^{\rm RH}$ and $\rho_p^{\rm RH}$ are relativistic Hartree (RH) densities for neutrons and protons, respectively. With this distribution and the best fit medium modification parameters in the previous section, the medium modified RIA calculations are performed. Solid curves in Fig. 33 are the results. As compared to the original MH model (dashed curves) and the IA2 model (dotted curves), the fits to the data are meaningfully improved. Thus the predictability of the medium effect model is confirmed again for the ^{120}Sn data.

In order to search the neutron distribution a sum of Gaussians (SOG) type distribution is used;

$$\rho_n^V(r) = \frac{N}{2\pi^{3/2}\gamma^3} \sum_i \frac{Q_i}{1+2R_i^2/\gamma^2} \left(e^{-(r-R_i)^2/\gamma^2} + e^{-(r+R_i)^2/\gamma^2} \right). \tag{71}$$

The volume integral of the point neutron distribution should be the neutron number N,

$$\int \rho_n^V(r)\, d\vec{r} = N. \tag{72}$$

By performing the integral we can see

$$\sum_i Q_i = 1. \tag{73}$$

With this constraint, Q_i are searched so as to reproduce ^{120}Sn data at 300 MeV, whereas width γ and position R_i of each Gaussian are fixed with the values listed in Ref. [43]. All the resulting SOG distributions with a good reduced χ^2;

$$\chi_\nu^2 \leq \chi_{\nu\min}^2 + 1, \tag{74}$$

where $\chi_\nu^2 \equiv \chi^2/\nu$, ν is the number of degrees of freedom ($\nu = 78$ in the present case) and $\chi_{\nu\min}^2$ is the minimum value of χ_ν^2, are possible densities and their superposition determines an error band, which is displayed in Fig. 34 as hatched area. Solid curves in Fig. 35 are the calculations of cross sections, analyzing powers and spin rotation parameters at 300 MeV using the best fit neutron distribution.

The deduced neutron distribution has an increase at the nuclear center as seen in Fig. 34. This result may be due to the wave function of neutrons in the $3s_{1/2}$ orbit as expected to be occupied in the ^{120}Sn nuclei. RH calculations of neutron distributions in ^{118}Sn and ^{120}Sn are compared in Fig. 36. The solid curve of ^{120}Sn has an increase also, whereas ^{118}Sn in which the $3s_{1/2}$ orbit is unoccupied has dent structure as indicated by the dashed curve. The RH calculation of ^{120}Sn under the assumption that not $3s_{1/2}$ but $1h_{11/2}$ orbit is

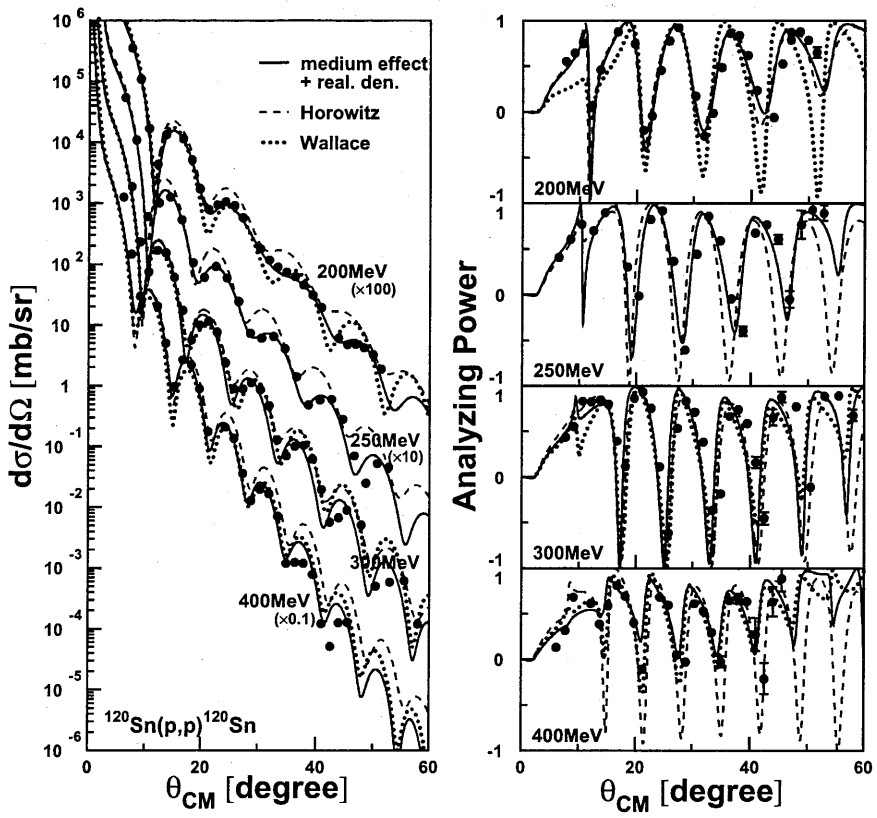

Figure 33: Comparison among three calculations for ^{120}Sn. Dashed and dotted curves represent the original RIA calculations of Horowitz and Wallace, respectively. Solid curves indicate the medium modified RIA calculations using the trial neutron distribution of (70). Fits to the data are meaningfully improved.

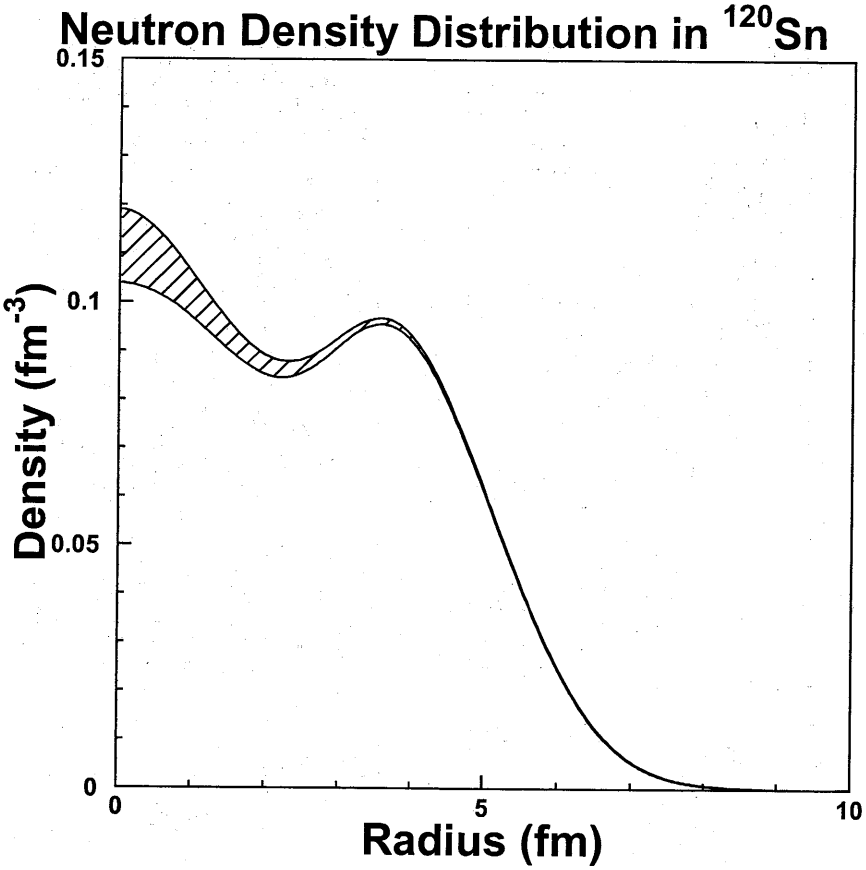

Figure 34: The neutron distribution in ^{120}Sn extracted from proton elastic scattering data at 300MeV is shown. Hatched area represents the superposition of possible distributions with good χ^2_ν defined by the inequality of (74).

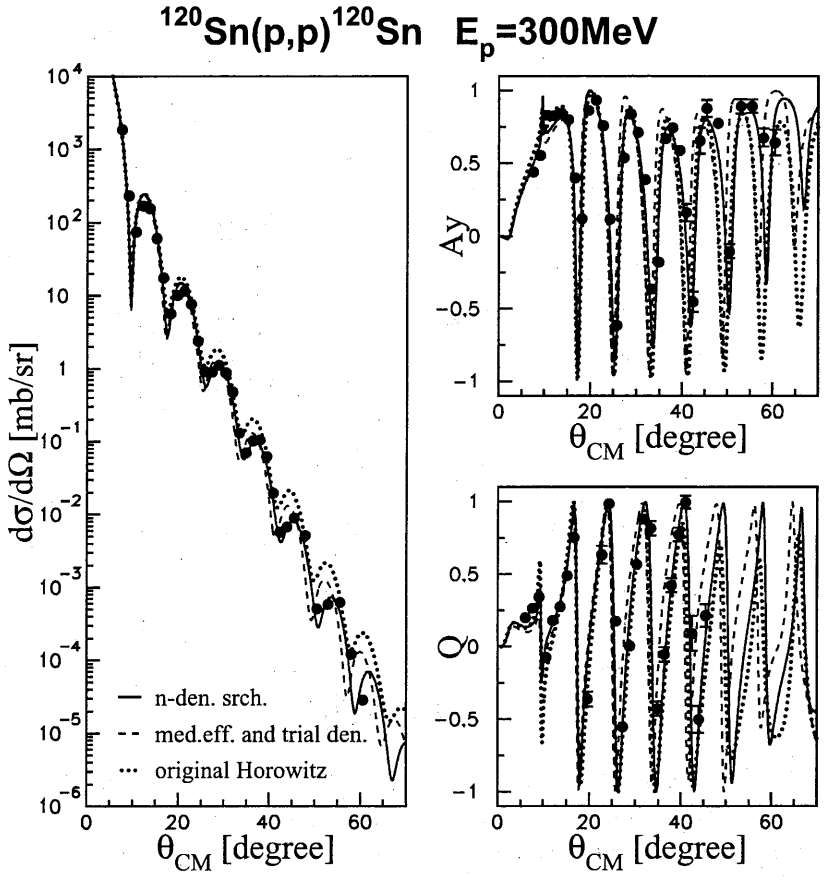

Figure 35: Cross sections, analyzing powers and spin rotation parameters at 300 MeV. Solid curves are the medium modified RIA with the best fit neutron distribution. Dashed curves are same but using the trial neutron distribution of (70). Dotted curves represent the original MH model with the RH densities.

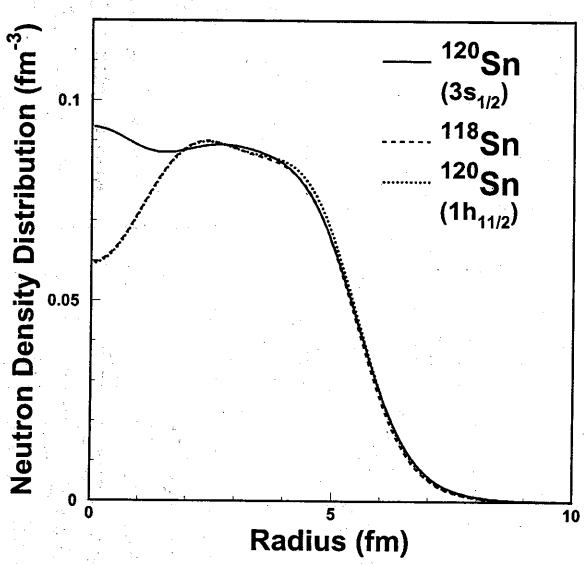

Figure 36: Relativistic Hartree calculations for neutrons are displayed. The solid curve represents the neutron in ^{120}Sn, while the dashed curve for ^{118}Sn. Clear bump structure at the nuclear center can be seen in ^{120}Sn. The dotted curve indicates the neutron in ^{120}Sn but the last two neutrons are assumed to occupy $1h_{11/2}$ orbit, not $3s_{1/2}$. The shape is very similar to ^{118}Sn.

occupied by the last two neutrons is also displayed as the dotted curve in the same figure. The shape is very similar to ^{118}Sn and hard to distinguish. Thus deduced increase at the nuclear center is a signature of $3s_{1/2}$ orbit.

Root mean square (RMS) radii of the realistic proton distribution deduced from the nuclear charge distribution and the best fit neutron distribution are

$$\left\langle r^2 \right\rangle_p^{1/2} = 4.569 \pm 0.004\,\mathrm{fm}, \tag{75}$$

$$\left\langle r^2 \right\rangle_n^{1/2} = 4.685 \pm 0.014\,\mathrm{fm}, \tag{76}$$

respectively. The error of $\langle r^2 \rangle_p^{1/2}$ comes from the error in the intrinsic proton charge radius, while the error of $\langle r^2 \rangle_n^{1/2}$ is estimated from the distribution of RMS radii of possible densities with good reduced χ^2 of (74). Thus RMS radius difference becomes

$$\begin{aligned} \Delta r_{np} &\equiv \left\langle r^2 \right\rangle_n^{1/2} - \left\langle r^2 \right\rangle_p^{1/2} \\ &= 0.116 \pm 0.015\,\mathrm{fm}. \end{aligned} \tag{77}$$

This result is consistent with the result[46] based on a sum rule of spin-dipole resonance (SDR), where the value of

$$\Delta r_{np} = 0.179 \pm 0.068\,\mathrm{fm}, \tag{78}$$

for ^{120}Sn has been reported.

Solid curves in Fig. 37 are the calculations using the best fit neutron density, whereas dashed curves are related to the trial neutron density of (70). The original RIA calculations without medium modifications using the RH densities are also displayed by dotted curves. It is notable that our data indicated by solid circles are well explained by the deduced density not only at 300 MeV but also at other energies although the density search is performed using the 300 MeV data only.

4.5 Effects of ρ meson modification

Isovector ρ mesons are insensitive to proton elastic scattering from $N \simeq Z$ nuclei as shown in Fig. 38, where dotted curves indicate the calculations assuming that ρ meson modifications are as same as ω meson (*i.e.* $a_\rho = a_\omega$ and $b_\rho = b_\omega$) and solid curves are the original ones without ρ meson modifications. Two types of curves are almost equal. Thus it is hard to determine ρ meson modifications in medium from data of ^{58}Ni, therefore not considered in Sec. 4.3. However, the ρ meson modifications contribute for $N \neq Z$

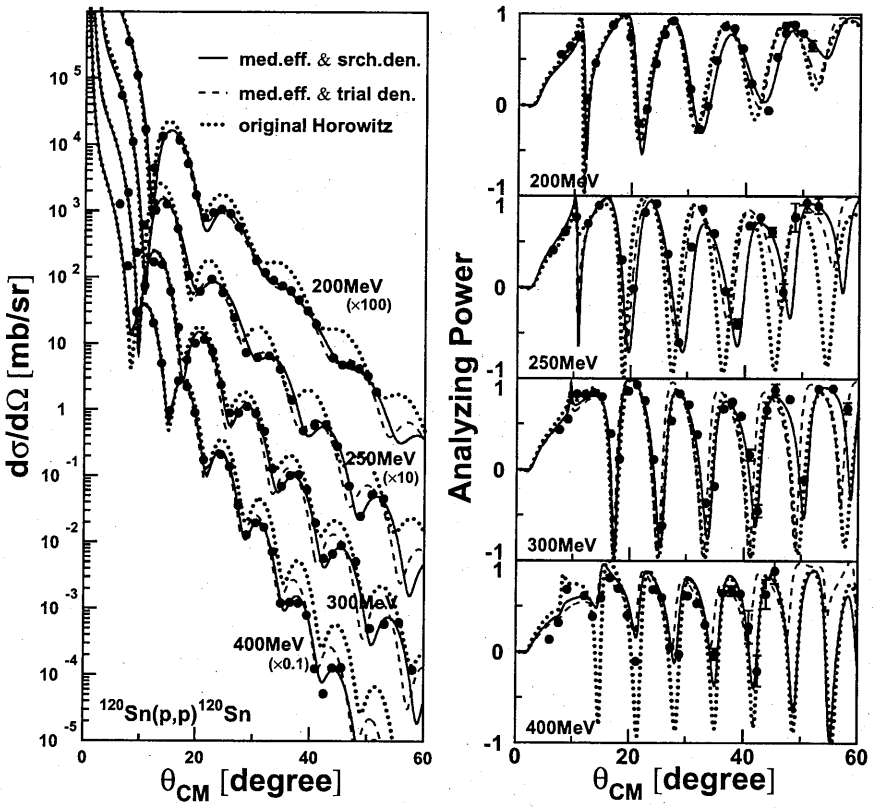

Figure 37: Cross sections and analyzing powers of proton elastic scattering from ^{120}Sn at E_p = 200, 250, 300 and 400 MeV. Meaning of the curves are same as Fig. 35.

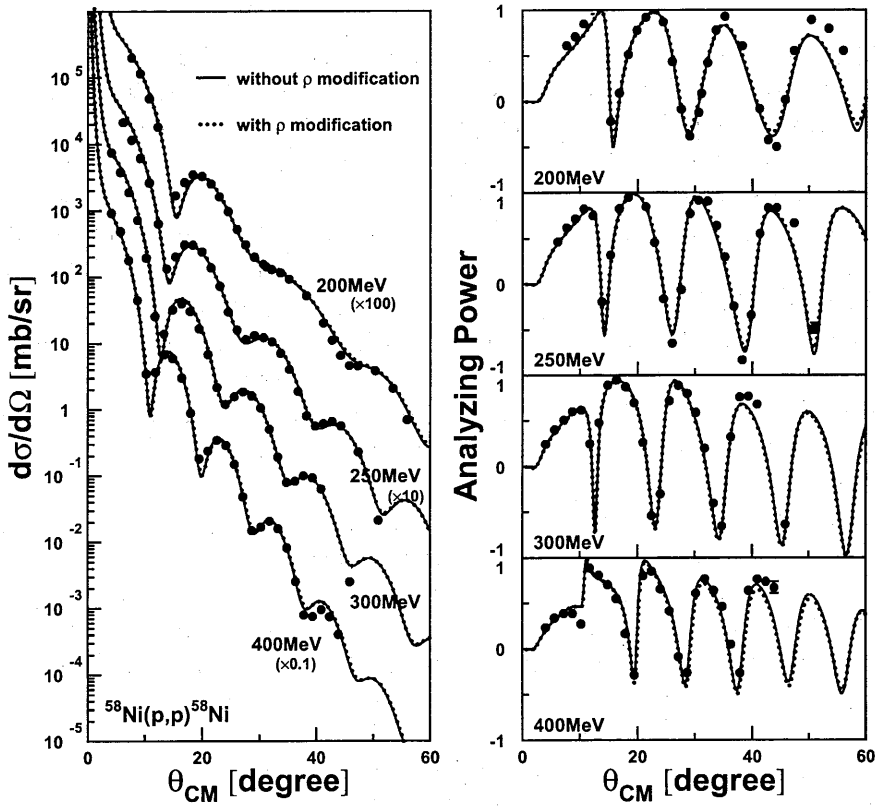

Figure 38: Two medium modified RIA calculations for ^{58}Ni at 200, 250, 300 and 400 MeV are compared. Dotted curves indicate the calculations assuming that ρ meson modifications are as same as ω meson (*i.e.* $a_\rho = a_\omega$ and $b_\rho = b_\omega$). Solid curves are the original ones without ρ meson modifications.

nuclei. This causes uncertainties in extracting neutron distributions. However, for deducing the final conclusion, modifications for ρ meson should be examined by other ways than the elastic scattering such as measurements of isovector inelastic transitions. Suggestions from the theoretical side are also indispensable.

5 Future perspective

Techniques to determine the interaction in nuclear medium and to extract neutron distributions in stable nuclei have been essentially established except for the ρ meson modification in nuclear medium. The investigations discussed above can also be extended to unstable nuclei; one of the new frontiers of nuclear physics. Due to the recent developments of radioactive isotope beam facilities all over the world, research fields in nuclear study are remarkably spreading toward the proton/neutron drip lines. Properties of nuclei far from the β stability line are expected to be different not only quantitatively but also qualitatively. For instance neutron rich unstable nuclei are expected to have anomalous structures such as the neutron skin and the halo. Neutron distributions in nuclei will provide fundamental information for nuclear structure study. Thus our techniques will provide powerful tools for such researches.

Indeed it is proposed to measure proton elastic scattering from unstable nuclei at intermediate energies by means of inversed kinematics measurements. Radioactive isotope beam factory (RIBF) is under construction in RIKEN. Many kinds of unstable nuclear beam of a few hundred MeV/A will be available. These beams will bombard hydrogen targets and recoiled protons will be measured by counter telescopes consisted of multi-wire drift chambers and NaI(Tl) scintillators surrounding the hydrogen targets. Elastic scattering events will be identified by the measurements of scattering angles and energies of recoiled protons with the counter telescopes. In the center of mass system, these scatterings are exactly the same as the scattering of intermediate energy protons from the fixed targets reported in this work. Thus the techniques developed here will be applicable to extracting nucleon distributions in unstable nuclei.

6 Conclusion

Spin rotation parameters of proton elastic scattering from ^{58}Ni were measured at $E_p = 200$, 300 and 400 MeV. By combining them with the previously measured cross sections and analyzing powers at the same energies, the se-

ries of measurements became the "complete" experiment. Cross sections and analyzing powers of proton elastic scattering from ^{58}Ni at 250 MeV, those of ^{120}Sn at E_p = 200, 250, 300 and 400 MeV and spin rotation parameters of ^{120}Sn at E_p = 300 MeV were also newly measured. The experiment was performed at Research Center for Nuclear Physics (RCNP), Osaka University, by using the high-resolution magnetic spectrometer 'Grand Raiden', the Focal Plane Polarimeter (FPP) and polarized proton beam from the ring cyclotron.

The experimental data were analyzed in the framework of the relativistic impulse approximations (RIA). Our previous work dealt with only cross sections and analyzing powers has found that the medium modified RIA explains the data well when compared to the original RIA by Murdock and Horowitz or the IA2 by Tjon and Wallace. In our model, coupling constants and masses of σ and ω mesons have been modified. It was found that this model also well explained newly measured spin rotation parameters except for 400 MeV without any changes. Thus the predictability of the medium modified RIA was established.

A new search was performed including spin rotation parameters and the best fit parameter set was found. Correlation between the modification parameters were investigated and strong correlations were found in some combinations of parameters.

We applied the present framework to ^{120}Sn and found that fits to the data were meaningfully improved compared to the original unmodified RIA models of MH and IA2, thus the predictability and applicability were confirmed again. With this reliable interaction in nuclear medium the neutron distribution in ^{120}Sn was searched so as to reproduce the ^{120}Sn data at 300 MeV. The deduced neutron distribution has an increase at the nuclear center. This seems to be a signature of $3s_{1/2}$ orbit as expected to be occupied in ^{120}Sn nuclei. Root mean square radius difference between the deduced neutron and proton distributions was found to be consistent with the result derived from a sum rule of spin-dipole resonance. By using the deduced neutron distribution, not only at 300 MeV but at other energies fits to the data were remarkably improved although they were not included in the search. These results imply that the deduced neutron distribution is reliable.

However, there still remains an ambiguity due to the ρ meson modification. It is impossible to fix the ρ meson modification only by the proton elastic scattering off ^{58}Ni since the isovector ρ mesons contribute little for $Z \simeq N$ nuclei. But it contributes to $Z \neq N$ nuclei. Further studies on ρ meson modification from both experimental and theoretical sides are indispensable.

7 Acknowledgments

This work would not be accomplished without a large amount of support from a considerable number of people.

First of all, I would like to express my appreciation to Prof. H. Sakaguchi. He is my supervisor and has continuously guided, advised and supported me from the planning of experiments to the publication. I also learn the grounding for experimental scientists from him.

I sincerely thank Dr. M. Nakamura for giving me various suggestions on analysis of this work. His remark was a great stimulus for me. It is my pleasure to express my gratitude to Prof. T. Noro for his helpful advice and suggestions.

I would like to thank all the members of the RCNP-E7/E69/E109 collaborators, who had shared the great efforts with me to lead the experiments succeeded; Dr. H. Akimune, Mr. T. Baba, Dr. I. Daito, Ms. H. Fujimura, Prof. K. Hosono, Dr. T. Inomata, Mr. T. Ishikawa, Mr. M. Itoh, Dr. M. Kawabata, Mr. T. Kawabata, Prof. T. Noro, Ms. E. Obayashi, Prof. H. Sakaguchi, Prof. Y. Sakemi, Ms. T. Taki, Dr. A. Tamii, Mr. S. Toyama, Mr. M. Tsukahara, Mr. M. Uchida, Mr. A. Yamagoshi, Mr. H. P. Yoshida, Dr. M. Yoshimura and Mr. M. Yosoi.

I owe a lot in my data analysis on spin rotation parameters to Ms. T. Taki's work in her master thesis and I would like to express my thanks to her.

I would like to express my gratitude to Mr. M. Yosoi, Dr. A. Tamii, Mr. T. Kawabata and Mr. H. P. Yoshida for giving me information on the operation and analysis of the FPP and the DAQ system.

I am grateful to Prof. Hatanaka and the other staff members of RCNP for their support, for providing clear, stable and high intensity beam during the experiment and also for beam time managements. I am thankful to Dr. K. Nagayama for designing the new Faraday cup for extremely high intensity beam. I am grateful to staffs of Computing and Network Group of RCNP for their continuous maintenance of computers and networks.

Special thanks should be expressed to Prof. H. Toki and Dr. K. Kaki for performing the IA2 calculations described in Sec. 4.

I would like to give my thanks to Prof. K. Imai, Prof. H. En'yo, Dr. T. Murakami and Dr. H. Funahashi for their continuous suggestions and encouragements.

I am also grateful to other staffs, all the younger members of Nuclear and Hadronic Physics Group of Kyoto University and Nuclear Science 1A Group of the RCNP, secretaries and office members for the support of my daily life.

I acknowledge the receipt of the Research Fellowships for Young Scientists of Japan Society for the Promotion of Science.

Finally I would like to thank my parents, grandmother, brother and his fiancée from the bottom of my heart for their warm supports and encouragements.

A Digital data of experimental results

The digital data of differential cross sections ($d\sigma/d\Omega$), analyzing powers (A_y) and spin rotation parameters (Q) of proton elastic scattering from ^{58}Ni and ^{120}Sn at E_p = 200, 250, 300 and 400 MeV are listed here. Not only the newly measured data but also previously measured data are contained for convenience.

Table 7: Cross sections, analyzing powers and spin rotation parameters for ^{58}Ni$(p,p)^{58}$Ni at 200 MeV.

θ_{CM} (deg)	$d\sigma/d\Omega$ (mb/sr)	A_y	Q
6.125	—	—	0.103 ± 0.016
7.657	(2.010 ± 0.011) × 10^3	0.613 ± 0.008	−0.002 ± 0.021
9.188	(1.166 ± 0.009) × 10^3	0.708 ± 0.013	−0.090 ± 0.016
10.719	(4.907 ± 0.049) × 10^2	0.849 ± 0.016	−0.112 ± 0.014
12.250	(1.821 ± 0.014) × 10^2	0.956 ± 0.012	−0.026 ± 0.011
13.780	—	—	0.183 ± 0.012
15.312	(1.700 ± 0.009) × 10^1	−0.216 ± 0.007	0.533 ± 0.020
16.842	(2.675 ± 0.013) × 10^1	0.092 ± 0.006	−0.194 ± 0.020
18.372	(3.496 ± 0.020) × 10^1	0.514 ± 0.008	−0.346 ± 0.026
19.902	(3.293 ± 0.016) × 10^1	0.777 ± 0.007	−0.379 ± 0.023
21.432	(2.536 ± 0.027) × 10^1	0.921 ± 0.017	−0.308 ± 0.022
22.961	(1.631 ± 0.018) × 10^1	0.969 ± 0.017	−0.104 ± 0.020
24.490	(9.717 ± 0.081) × 10^0	0.868 ± 0.013	0.238 ± 0.012
26.018	(5.218 ± 0.036) × 10^0	0.434 ± 0.009	0.678 ± 0.016
27.547	(3.063 ± 0.016) × 10^0	−0.085 ± 0.007	0.879 ± 0.016
29.075	(2.004 ± 0.009) × 10^0	−0.379 ± 0.005	0.539 ± 0.015
30.602	(1.551 ± 0.009) × 10^0	−0.122 ± 0.008	−0.155 ± 0.016
31.111	(1.436 ± 0.008) × 10^0	0.087 ± 0.007	—
32.129	(1.301 ± 0.006) × 10^0	0.420 ± 0.006	−0.556 ± 0.016
33.656	(1.157 ± 0.006) × 10^0	0.779 ± 0.001	−0.520 ± 0.014
35.182	(9.333 ± 0.099) × 10^{-1}	0.927 ± 0.016	−0.228 ± 0.013
36.705	—	—	0.190 ± 0.013
38.233	(5.263 ± 0.031) × 10^{-1}	0.605 ± 0.007	0.543 ± 0.014
39.755	—	—	0.832 ± 0.016
41.282	(2.030 ± 0.017) × 10^{-1}	−0.079 ± 0.011	0.919 ± 0.023
42.805	(1.117 ± 0.011) × 10^{-1}	−0.420 ± 0.011	0.720 ± 0.027
44.328	(6.494 ± 0.094) × 10^{-2}	−0.493 ± 0.016	−0.018 ± 0.037
45.851	(4.618 ± 0.063) × 10^{-2}	0.017 ± 0.017	−0.686 ± 0.041
47.373	(4.531 ± 0.060) × 10^{-2}	0.556 ± 0.016	−0.718 ± 0.040
50.415	(3.856 ± 0.058) × 10^{-2}	0.892 ± 0.017	—
53.454	(2.091 ± 0.031) × 10^{-2}	0.796 ± 0.017	—
55.985	(6.967 ± 0.184) × 10^{-3}	0.553 ± 0.033	—

Table 8: Cross sections and analyzing powers for ^{58}Ni$(p,p)^{58}$Ni at 250 MeV.

θ_{CM} (deg)	$d\sigma/d\Omega$ (mb/sr)	A_y
6.131	$(2.143 \pm 0.031) \times 10^{3}$	0.466 ± 0.021
7.664	$(1.168 \pm 0.013) \times 10^{3}$	0.618 ± 0.018
9.197	$(6.234 \pm 0.073) \times 10^{2}$	0.716 ± 0.019
10.729	$(2.629 \pm 0.026) \times 10^{2}$	0.824 ± 0.017
12.261	$(6.408 \pm 0.136) \times 10^{1}$	0.751 ± 0.035
13.793	$(1.337 \pm 0.013) \times 10^{1}$	-0.195 ± 0.015
15.325	$(2.016 \pm 0.017) \times 10^{1}$	0.318 ± 0.012
16.857	$(3.081 \pm 0.058) \times 10^{1}$	0.827 ± 0.033
18.388	$(3.025 \pm 0.031) \times 10^{1}$	0.949 ± 0.016
19.919	$(2.401 \pm 0.042) \times 10^{1}$	1.050 ± 0.033
21.450	$(1.397 \pm 0.016) \times 10^{1}$	0.846 ± 0.017
22.981	$(7.266 \pm 0.075) \times 10^{0}$	0.457 ± 0.016
24.511	$(2.993 \pm 0.030) \times 10^{0}$	-0.160 ± 0.015
26.041	$(1.603 \pm 0.020) \times 10^{0}$	-0.649 ± 0.019
27.570	$(1.148 \pm 0.014) \times 10^{0}$	-0.060 ± 0.019
29.099	$(1.313 \pm 0.013) \times 10^{0}$	0.774 ± 0.016
30.628	$(1.231 \pm 0.019) \times 10^{0}$	0.918 ± 0.022
32.156	$(1.053 \pm 0.010) \times 10^{0}$	0.908 ± 0.017
33.684	$(7.127 \pm 0.081) \times 10^{-1}$	0.638 ± 0.017
35.211	$(4.051 \pm 0.039) \times 10^{-1}$	0.298 ± 0.015
36.738	$(1.889 \pm 0.016) \times 10^{-1}$	-0.241 ± 0.013
38.264	$(8.105 \pm 0.116) \times 10^{-2}$	-0.833 ± 0.021
39.790	$(5.666 \pm 0.081) \times 10^{-2}$	-0.340 ± 0.022
41.315	$(6.140 \pm 0.086) \times 10^{-2}$	0.553 ± 0.021
42.840	$(6.590 \pm 0.089) \times 10^{-2}$	0.836 ± 0.020
44.364	$(5.678 \pm 0.081) \times 10^{-2}$	0.834 ± 0.021
47.410	$(2.287 \pm 0.055) \times 10^{-2}$	0.666 ± 0.035
50.961	$(2.129 \pm 0.085) \times 10^{-3}$	-0.484 ± 0.058

Table 9: Cross sections, analyzing powers and spin rotation parameters for ^{58}Ni$(p,p)^{58}$Ni at 300 MeV.

θ_{CM} (deg)	$d\sigma/d\Omega$ (mb/sr)	A_y	Q
4.091	$(7.490 \pm 0.034) \times 10^{3}$	0.2447 ± 0.0064	—
5.625	$(3.806 \pm 0.026) \times 10^{3}$	0.4036 ± 0.0098	—
7.159	$(1.884 \pm 0.016) \times 10^{3}$	0.5109 ± 0.0121	—
8.181	—	—	0.289 ± 0.036
8.693	$(7.180 \pm 0.024) \times 10^{2}$	0.6049 ± 0.0046	—
10.226	$(1.937 \pm 0.010) \times 10^{2}$	0.6208 ± 0.0066	0.484 ± 0.026
11.760	$(2.566 \pm 0.017) \times 10^{1}$	0.2509 ± 0.0086	—
12.782	—	—	-0.121 ± 0.038
13.293	$(1.391 \pm 0.010) \times 10^{1}$	0.4793 ± 0.0088	—
14.826	$(3.208 \pm 0.023) \times 10^{1}$	0.8949 ± 0.0089	—
15.337	—	—	-0.160 ± 0.034
16.359	$(3.945 \pm 0.032) \times 10^{1}$	0.9490 ± 0.0061	—
17.892	$(3.015 \pm 0.021) \times 10^{1}$	0.8777 ± 0.0097	0.392 ± 0.036
19.424	$(1.672 \pm 0.008) \times 10^{1}$	0.7016 ± 0.0058	—
20.446	—	—	0.847 ± 0.033
20.956	$(6.772 \pm 0.035) \times 10^{0}$	0.2628 ± 0.0067	—
22.488	$(2.156 \pm 0.017) \times 10^{0}$	0.5379 ± 0.0093	—
22.999	—	—	0.383 ± 0.051
24.019	$(1.209 \pm 0.007) \times 10^{0}$	0.2999 ± 0.0080	—
25.551	$(1.565 \pm 0.011) \times 10^{0}$	0.7219 ± 0.0088	-0.577 ± 0.056
27.081	$(1.849 \pm 0.009) \times 10^{0}$	0.8910 ± 0.0062	—
28.102	—	—	0.329 ± 0.055
28.611	$(1.623 \pm 0.010) \times 10^{0}$	0.8024 ± 0.0078	—
30.141	$(1.061 \pm 0.005) \times 10^{0}$	0.5932 ± 0.0054	—
30.651	—	—	0.861 ± 0.054
31.671	$(5.086 \pm 0.027) \times 10^{-1}$	0.2038 ± 0.0071	—
33.200	$(1.939 \pm 0.010) \times 10^{-1}$	0.4027 ± 0.0064	0.912 ± 0.031
34.728	$(8.076 \pm 0.088) \times 10^{-2}$	0.6533 ± 0.0126	—
35.747	—	—	-0.744 ± 0.031
36.256	$(8.361 \pm 0.079) \times 10^{-2}$	0.3258 ± 0.0122	—
37.784	$(1.008 \pm 0.008) \times 10^{-1}$	0.7610 ± 0.0091	—
38.293	—	—	0.038 ± 0.030
39.310	$(9.345 \pm 0.088) \times 10^{-2}$	0.7697 ± 0.0104	—
40.837	$(6.303 \pm 0.063) \times 10^{-2}$	0.6816 ± 0.0112	0.636 ± 0.029
43.380	—	—	0.923 ± 0.031
45.921	$(2.528 \pm 0.100) \times 10^{-3}$	0.6343 ± 0.0465	-0.236 ± 0.153
48.460	—	—	-0.179 ± 0.121
50.997	—	—	0.412 ± 0.118
54.039	—	—	0.614 ± 0.119

Table 10: Cross sections, analyzing powers and spin rotation parameters for ^{58}Ni$(p,p)^{58}$Ni at 400 MeV.

θ_{CM} (deg)	$d\sigma/d\Omega$ (mb/sr)	A_y	Q
4.099	$(9.263 \pm 0.087) \times 10^{3}$	0.236 ± 0.014	—
5.635	$(4.852 \pm 0.027) \times 10^{3}$	0.343 ± 0.008	—
7.172	$(1.791 \pm 0.009) \times 10^{3}$	0.390 ± 0.008	0.238 ± 0.022
8.709	$(4.495 \pm 0.026) \times 10^{2}$	0.391 ± 0.008	0.413 ± 0.030
10.245	$(3.472 \pm 0.032) \times 10^{1}$	0.276 ± 0.013	0.621 ± 0.030
11.782	$(3.676 \pm 0.026) \times 10^{1}$	0.888 ± 0.009	0.037 ± 0.026
13.318	$(6.849 \pm 0.051) \times 10^{1}$	0.807 ± 0.010	0.303 ± 0.031
14.854	$(5.945 \pm 0.043) \times 10^{1}$	0.705 ± 0.009	0.408 ± 0.032
16.389	$(3.026 \pm 0.023) \times 10^{1}$	0.552 ± 0.010	0.598 ± 0.030
17.925	$(8.831 \pm 0.070) \times 10^{0}$	0.168 ± 0.011	0.755 ± 0.031
19.460	$(1.845 \pm 0.009) \times 10^{0}$	-0.284 ± 0.007	0.469 ± 0.033
20.995	$(2.405 \pm 0.016) \times 10^{0}$	0.804 ± 0.009	0.036 ± 0.044
22.529	$(3.460 \pm 0.017) \times 10^{0}$	0.853 ± 0.007	0.440 ± 0.048
24.063	$(2.905 \pm 0.026) \times 10^{0}$	0.658 ± 0.012	0.629 ± 0.049
25.597	$(1.506 \pm 0.011) \times 10^{0}$	0.414 ± 0.010	0.812 ± 0.051
27.130	$(4.879 \pm 0.037) \times 10^{-1}$	-0.086 ± 0.011	0.892 ± 0.098
28.663	$(1.505 \pm 0.018) \times 10^{-1}$	-0.257 ± 0.016	0.524 ± 0.180
30.195	$(1.698 \pm 0.017) \times 10^{-1}$	0.610 ± 0.012	0.263 ± 0.185
31.727	$(2.063 \pm 0.025) \times 10^{-1}$	0.770 ± 0.014	0.202 ± 0.028
33.258	$(1.609 \pm 0.016) \times 10^{-1}$	0.643 ± 0.012	0.422 ± 0.028
34.789	$(8.288 \pm 0.092) \times 10^{-2}$	0.464 ± 0.015	0.759 ± 0.029
36.319	$(2.567 \pm 0.058) \times 10^{-2}$	0.051 ± 0.032	0.932 ± 0.049
37.849	$(8.002 \pm 0.211) \times 10^{-3}$	-0.262 ± 0.037	0.682 ± 0.071
39.378	$(7.557 \pm 0.254) \times 10^{-3}$	0.639 ± 0.040	0.080 ± 0.057
40.907	$(9.677 \pm 0.242) \times 10^{-3}$	0.764 ± 0.031	0.327 ± 0.055
42.435	$(7.464 \pm 0.251) \times 10^{-3}$	0.738 ± 0.042	0.504 ± 0.057
43.962	$(4.044 \pm 0.204) \times 10^{-3}$	0.673 ± 0.065	0.713 ± 0.063
45.488	—	—	0.817 ± 0.097

Table 11: Cross sections, analyzing powers and spin rotation parameters for ^{120}Sn$(p,p)^{120}$Sn at 200 MeV.

θ_{CM} (deg)	$d\sigma/d\Omega$ (mb/sr)	A_y	Q
7.576	$(3.547 \pm 0.035) \times 10^{3}$	0.553 ± 0.014	—
9.091	$(1.093 \pm 0.009) \times 10^{3}$	0.645 ± 0.013	—
10.606	$(1.686 \pm 0.013) \times 10^{2}$	0.747 ± 0.010	—
12.121	$(4.425 \pm 0.027) \times 10^{1}$	0.075 ± 0.008	—
13.636	$(1.331 \pm 0.010) \times 10^{2}$	0.460 ± 0.009	-0.233 ± 0.024
16.666	$(1.158 \pm 0.011) \times 10^{2}$	0.878 ± 0.014	-0.263 ± 0.023
18.180	$(5.188 \pm 0.069) \times 10^{1}$	0.972 ± 0.022	-0.239 ± 0.029
19.695	$(1.747 \pm 0.014) \times 10^{1}$	0.746 ± 0.011	—
21.209	$(8.005 \pm 0.048) \times 10^{0}$	-0.199 ± 0.008	—
22.723	$(9.446 \pm 0.044) \times 10^{0}$	-0.043 ± 0.006	—
24.237	$(1.064 \pm 0.008) \times 10^{1}$	0.458 ± 0.010	—
25.751	$(9.158 \pm 0.089) \times 10^{0}$	0.780 ± 0.013	—
27.265	$(5.804 \pm 0.056) \times 10^{0}$	0.926 ± 0.014	—
30.291	$(1.794 \pm 0.013) \times 10^{0}$	0.175 ± 0.010	—
31.805	$(1.172 \pm 0.008) \times 10^{0}$	-0.260 ± 0.009	—
33.317	$(9.026 \pm 0.074) \times 10^{-1}$	-0.011 ± 0.011	—
34.830	$(7.394 \pm 0.068) \times 10^{-1}$	0.489 ± 0.012	—
36.343	$(6.289 \pm 0.063) \times 10^{-1}$	0.864 ± 0.013	—
37.855	$(4.559 \pm 0.043) \times 10^{-1}$	0.840 ± 0.012	—
39.367	$(3.138 \pm 0.033) \times 10^{-1}$	0.622 ± 0.013	—
40.878	$(1.957 \pm 0.019) \times 10^{-1}$	0.235 ± 0.013	—
43.901	$(6.137 \pm 0.087) \times 10^{-2}$	-0.058 ± 0.019	—
45.412	$(4.829 \pm 0.073) \times 10^{-2}$	0.527 ± 0.019	—
46.923	$(4.865 \pm 0.094) \times 10^{-2}$	0.786 ± 0.023	—
46.923	$(4.839 \pm 0.112) \times 10^{-2}$	0.870 ± 0.025	—
48.433	$(4.218 \pm 0.087) \times 10^{-2}$	0.878 ± 0.022	—
49.943	$(3.264 \pm 0.094) \times 10^{-2}$	0.786 ± 0.033	—
51.453	$(1.900 \pm 0.085) \times 10^{-2}$	0.651 ± 0.053	—

Table 12: Cross sections and analyzing powers for ^{120}Sn$(p,p)^{120}$Sn at 250 MeV.

θ_{CM} (deg)	$d\sigma/d\Omega$ (mb/sr)	A_y
6.339	$(5.456 \pm 0.082) \times 10^{3}$	0.412 ± 0.021
8.360	$(1.105 \pm 0.013) \times 10^{3}$	0.608 ± 0.018
10.381	$(6.065 \pm 0.078) \times 10^{1}$	0.773 ± 0.019
12.402	$(1.018 \pm 0.011) \times 10^{2}$	0.704 ± 0.016
14.423	$(1.258 \pm 0.016) \times 10^{2}$	0.900 ± 0.023
16.443	$(5.356 \pm 0.077) \times 10^{1}$	0.958 ± 0.022
18.464	$(1.061 \pm 0.010) \times 10^{1}$	0.304 ± 0.013
20.484	$(6.102 \pm 0.078) \times 10^{0}$	-0.010 ± 0.017
22.503	$(9.276 \pm 0.136) \times 10^{0}$	0.826 ± 0.021
24.523	$(5.879 \pm 0.096) \times 10^{0}$	0.921 ± 0.025
26.542	$(2.452 \pm 0.021) \times 10^{0}$	0.366 ± 0.011
28.561	$(7.330 \pm 0.104) \times 10^{-1}$	-0.604 ± 0.019
30.579	$(6.148 \pm 0.089) \times 10^{-1}$	0.448 ± 0.020
32.598	$(6.534 \pm 0.111) \times 10^{-1}$	0.859 ± 0.024
34.615	$(4.148 \pm 0.069) \times 10^{-1}$	0.591 ± 0.022
36.633	$(1.412 \pm 0.024) \times 10^{-1}$	-0.042 ± 0.024
38.650	$(4.859 \pm 0.186) \times 10^{-2}$	-0.397 ± 0.050
40.666	$(5.879 \pm 0.151) \times 10^{-2}$	0.681 ± 0.032
42.682	$(6.045 \pm 0.172) \times 10^{-2}$	0.770 ± 0.035
44.697	$(2.843 \pm 0.107) \times 10^{-2}$	0.607 ± 0.049
46.712	$(7.099 \pm 0.447) \times 10^{-3}$	-0.051 ± 0.090
48.727	$(2.506 \pm 0.319) \times 10^{-3}$	0.768 ± 0.153
50.740	$(5.291 \pm 0.508) \times 10^{-3}$	0.929 ± 0.102
52.754	$(4.635 \pm 0.348) \times 10^{-3}$	0.895 ± 0.079

Table 13: Cross sections, analyzing powers and spin rotation parameters for ^{120}Sn$(p,p)^{120}$Sn at 300 MeV.

θ_{CM} (deg)	$d\sigma/d\Omega$ (mb/sr)	A_y	Q
3.033	$(3.858 \pm 0.020) \times 10^4$	0.020 ± 0.007	—
4.550	$(1.804 \pm 0.010) \times 10^4$	0.216 ± 0.008	—
6.066	$(6.915 \pm 0.035) \times 10^3$	0.347 ± 0.007	0.202 ± 0.022
7.582	$(1.876 \pm 0.011) \times 10^3$	0.441 ± 0.007	0.264 ± 0.019
9.099	$(2.340 \pm 0.014) \times 10^2$	0.554 ± 0.008	0.341 ± 0.023
10.615	$(7.407 \pm 0.057) \times 10^1$	0.831 ± 0.010	-0.075 ± 0.023
12.131	$(1.696 \pm 0.011) \times 10^2$	0.828 ± 0.009	0.181 ± 0.025
13.647	$(1.555 \pm 0.012) \times 10^2$	0.845 ± 0.012	0.276 ± 0.025
15.163	$(6.072 \pm 0.031) \times 10^1$	0.800 ± 0.006	0.490 ± 0.029
16.679	$(1.741 \pm 0.010) \times 10^1$	0.398 ± 0.007	0.753 ± 0.033
18.195	$(5.682 \pm 0.031) \times 10^0$	0.117 ± 0.007	—
19.711	$(1.014 \pm 0.008) \times 10^1$	0.864 ± 0.010	-0.363 ± 0.050
21.226	$(1.154 \pm 0.008) \times 10^1$	0.933 ± 0.009	0.633 ± 0.061
22.742	$(7.658 \pm 0.045) \times 10^0$	0.759 ± 0.008	—
24.257	$(2.384 \pm 0.013) \times 10^0$	0.115 ± 0.007	0.986 ± 0.003
25.772	$(9.045 \pm 0.078) \times 10^{-1}$	-0.613 ± 0.010	0.177 ± 0.034
27.286	$(8.990 \pm 0.051) \times 10^{-1}$	0.536 ± 0.007	-0.553 ± 0.030
28.801	$(1.122 \pm 0.010) \times 10^0$	0.836 ± 0.010	0.005 ± 0.029
30.316	$(8.749 \pm 0.051) \times 10^{-1}$	0.712 ± 0.007	0.566 ± 0.030
31.830	$(4.749 \pm 0.038) \times 10^{-1}$	0.388 ± 0.010	0.880 ± 0.029
33.344	$(1.302 \pm 0.018) \times 10^{-1}$	-0.363 ± 0.018	0.815 ± 0.049
34.857	$(7.033 \pm 0.134) \times 10^{-2}$	-0.182 ± 0.025	-0.429 ± 0.050
36.371	$(1.024 \pm 0.017) \times 10^{-1}$	0.670 ± 0.019	-0.054 ± 0.049
37.884	$(1.049 \pm 0.016) \times 10^{-1}$	0.745 ± 0.017	0.423 ± 0.048
39.397	$(6.247 \pm 0.113) \times 10^{-2}$	0.590 ± 0.022	0.771 ± 0.047
40.910	$(1.961 \pm 0.087) \times 10^{-2}$	0.162 ± 0.060	0.996 ± 0.045
42.422	$(5.719 \pm 0.325) \times 10^{-3}$	-0.452 ± 0.069	0.091 ± 0.120
43.934	$(6.744 \pm 0.496) \times 10^{-3}$	0.655 ± 0.087	-0.501 ± 0.093
45.446	$(9.020 \pm 0.505) \times 10^{-3}$	0.878 ± 0.053	0.213 ± 0.077
47.965	$(5.173 \pm 0.061) \times 10^{-3}$	0.775 ± 0.017	—
50.483	$(5.102 \pm 0.174) \times 10^{-4}$	-0.105 ± 0.048	—
53.001	$(5.885 \pm 0.198) \times 10^{-4}$	0.891 ± 0.041	—
55.517	$(6.234 \pm 0.193) \times 10^{-4}$	0.893 ± 0.037	—
58.032	$(1.210 \pm 0.057) \times 10^{-4}$	0.677 ± 0.059	—
60.546	$(2.844 \pm 0.196) \times 10^{-5}$	0.643 ± 0.086	—

Table 14: Cross sections and analyzing powers for $^{120}\mathrm{Sn}(p,p)^{120}\mathrm{Sn}$ at 400 MeV.

θ_{CM} (deg)	$d\sigma/d\Omega$ (mb/sr)	A_y
6.072	$(1.262 \pm 0.004) \times 10^{4}$	0.136 ± 0.008
7.589	$(1.466 \pm 0.006) \times 10^{3}$	0.318 ± 0.011
9.107	$(2.983 \pm 0.026) \times 10^{2}$	0.685 ± 0.022
12.142	$(2.034 \pm 0.014) \times 10^{2}$	0.615 ± 0.018
13.660	$(5.007 \pm 0.039) \times 10^{1}$	0.391 ± 0.021
15.177	$(9.713 \pm 0.080) \times 10^{0}$	0.593 ± 0.021
16.694	$(2.693 \pm 0.023) \times 10^{1}$	0.813 ± 0.021
18.212	$(2.215 \pm 0.014) \times 10^{1}$	0.693 ± 0.017
19.729	$(9.028 \pm 0.066) \times 10^{0}$	0.402 ± 0.019
21.245	$(1.765 \pm 0.021) \times 10^{0}$	-0.104 ± 0.032
24.278	$(2.094 \pm 0.013) \times 10^{0}$	0.683 ± 0.017
25.795	$(1.389 \pm 0.009) \times 10^{0}$	0.599 ± 0.016
27.311	$(3.610 \pm 0.039) \times 10^{-1}$	0.050 ± 0.029
28.827	$(1.301 \pm 0.024) \times 10^{-1}$	-0.024 ± 0.048
30.342	$(1.966 \pm 0.027) \times 10^{-1}$	0.615 ± 0.036
31.858	$(1.690 \pm 0.030) \times 10^{-1}$	0.532 ± 0.046
33.373	$(7.204 \pm 0.137) \times 10^{-2}$	0.298 ± 0.028
34.888	$(1.212 \pm 0.048) \times 10^{-2}$	-0.024 ± 0.063
36.402	$(1.240 \pm 0.037) \times 10^{-2}$	0.647 ± 0.043
37.917	$(1.203 \pm 0.042) \times 10^{-2}$	0.670 ± 0.051
39.431	$(7.928 \pm 0.245) \times 10^{-3}$	0.636 ± 0.043
40.944	$(1.233 \pm 0.142) \times 10^{-3}$	0.276 ± 0.180
42.458	$(5.204 \pm 0.571) \times 10^{-4}$	-0.210 ± 0.170
43.971	$(1.280 \pm 0.138) \times 10^{-3}$	0.634 ± 0.159
45.484	$(1.284 \pm 0.140) \times 10^{-3}$	0.888 ± 0.140

B Relativistic impulse approximation

The present analysis is essentially based on the framework of the relativistic impulse approximation (RIA) of Murdock and Horowitz (MH model)[4]. Thus overview of the MH model is reviewed here.

In the MH model, an NN scattering amplitude of the relativistic Love-Franey model of the form

$$\begin{aligned} F &= F^S + F^V \gamma^\mu_{(0)} \gamma_{(1)\mu} - F^{PV} \frac{\not{q}\gamma^5_{(0)}}{2M} \frac{\not{q}\gamma^5_{(1)}}{2M} \\ &\quad + F^T \sigma^{\mu\nu}_{(0)} \sigma_{(1)\mu\nu} + F^A \gamma^5_{(0)} \gamma^\mu_{(0)} \gamma^5_{(1)} \gamma_{(1)\mu}, \end{aligned} \tag{79}$$

is used. Here the subscripts (0) and (1) refer to the projectile and target nucleons, respectively. The superscripts S, V, PV, T, and A designate scalar, vector, pseudo-vector, tensor and axial-vector parts of the NN amplitude. Note that the pseudo-scalar piece $F^{PS}\gamma^5_{(0)}\gamma^5_{(1)}$ in the expression (1) in Sec. 1 is replaced by the pseudo-vector one in (79). They are equivalent for free NN scattering, but may be different in a nucleus. Indeed pseudo-vector coupling is desirable to give meaningful agreements at lower energies[4, 5].

Each of $F^L (L = S, V, PV, T$ or $A)$ may be written in the MH model as

$$F^L(q, E_c) = i \frac{M^2}{2E_c k_c} \left[F^L_D(q) + F^L_X(Q) \right], \tag{80}$$

$$F^L_D(q) = \sum_j \delta_{L,L(j)} \{\vec{\tau}_0 \cdot \vec{\tau}_1\}^{I_j} f^j(q), \tag{81}$$

$$F^L_X(Q) = (-1)^T \sum_i B_{L(j),L} \{\vec{\tau}_0 \cdot \vec{\tau}_1\}^{I_j} f^j(Q), \tag{82}$$

$$f^j(q) = \frac{g_j^2}{q^2 + m_j^2} \left(\frac{\Lambda_j^2}{\Lambda_j^2 + q^2} \right)^2 - \frac{\bar{g}_j^2}{q^2 + \bar{m}_j^2} \left(\frac{\bar{\Lambda}_j^2}{\bar{\Lambda}_j^2 + q^2} \right)^2, \tag{83}$$

where D and X indicate the direct and exchange terms (Fig. 39), q and Q are direct and exchange three-momentum transfers. I_j and $L(j)$ denotes the j-th meson's isospin and Lorentz type of coupling to nucleon. $B_{L(j),L}$ is the $(L(j), L)$ component of the Fierz transformation matrix;

$$B_{LL'} = \frac{\mathrm{Tr}(\lambda^L \lambda^{L'} \lambda^L \lambda^{L'})}{[\mathrm{Tr}(\lambda^{L'} \lambda^{L'})]^2} \tag{84}$$

$$= \frac{1}{8} \begin{pmatrix} 2 & 2 & 1 & -2 & 2 \\ 8 & -4 & 0 & -4 & -8 \\ 24 & 0 & -4 & 0 & 24 \\ -8 & -4 & 0 & -4 & 8 \\ 2 & -2 & 1 & 2 & 2 \end{pmatrix}, \tag{85}$$

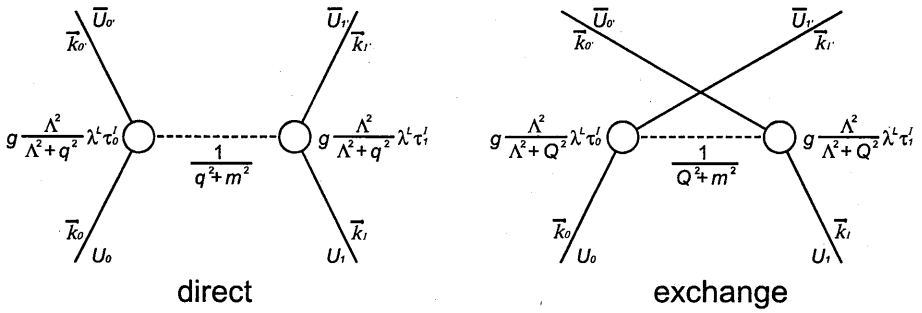

Figure 39: Meson exchange diagrams

where the rows and columns are labeled in the order S, V, T, A, PV and λ^L denotes type-L Dirac matrices. The coupling constant, mass and cut-off parameter for the j-th meson denoted by g_j, m_j and Λ_j are fitted to the free NN amplitudes at several different laboratory energies. The full set of parameters can be found in Ref. [4, 5]. T is the total isospin of the two-nucleon system, thus

$$F^L(pp) = F^L(T=1), \tag{86}$$

$$F^L(pn) = \frac{1}{2}\left[F^L(T=0) + F^L(T=1)\right], \tag{87}$$

are used to get pp and pn scattering amplitudes, respectively.

The first-order Dirac optical potentials for the spherical nuclei are produced by folding this NN amplitude with the target densities;

$$U^L(r;E) = U_D^L(r;E) + U_X^L(r;E), \tag{88}$$

$$U_D^L(r;E) = -\frac{4\pi i p}{M}\int d\vec{r}\,'\rho^L(\vec{r}\,')\,t_D^L\left(|\vec{r}\,'-\vec{r}|;E\right), \tag{89}$$

$$U_X^L(r;E) = -\frac{4\pi i p}{M}\int d\vec{r}\,'\rho^L(\vec{r}\,',\vec{r})\,t_X^L\left(|\vec{r}\,'-\vec{r}|;E\right) j_0(p|\vec{r}\,'-\vec{r}|), \tag{90}$$

where $t_D^L(|\vec{r}|;E)$ are Fourier transforms of $t_D^L(q,E) \equiv (iM^2/2E_ck_c)F_D^L(q)$ and similarly for the exchange pieces $t_X^L(Q,E)$. $\rho^L(\vec{r})$ are type-L target densities. In the MH model they are expressed as sums over the occupied nuclear levels;

$$\rho^L(\vec{r}) = \sum_{\alpha}^{\text{occ.}} \bar{\phi}_\alpha(\vec{r})\lambda^L\phi_\alpha(\vec{r}), \tag{91}$$

where ϕ_α is a single particle four-component wave function in state α, and the relativistic Hartree (RH) approximation is applied to obtain ϕ_α. Non-local

densities $\rho^L(\vec{r}',\vec{r})$ are approximated in this model as

$$\rho^L(\vec{r}',\vec{r}) \approx \rho^L\left(\frac{1}{2}(\vec{r}'+\vec{r})\right)\left(\frac{3}{|\vec{r}'-\vec{r}|k_F}\right) j_1(|\vec{r}'-\vec{r}|k_F), \qquad (92)$$

where $2k_F^3/3\pi^2 = \rho^V((\vec{r}'+\vec{r})/2)$. For a spin zero nucleus, the only nonzero densities are scalar, vector and tensor densities with $\lambda^T = \sigma^{0i}$ in (91). The tensor contribution is found to be small and will be neglected. Note that the vector densities ρ^V are same as a point nucleon (baryon) densities, while the scalar densities ρ^S have no nonrelativistic analog.

The Dirac equation for the projectile is written as

$$\left\{-i\vec{\alpha}\cdot\vec{\nabla} + U^V(r;E) + \beta\left[M + U^S(r;E)\right]\right\}\mathcal{U}_0(r) = E\mathcal{U}_0(r). \qquad (93)$$

Here $\mathcal{U}_0$ is the incident projectile wave function, E is the total energy in nucleon–nucleus cm coordinate system, and M is the mass of the proton, $\vec{\alpha},\beta$ are Dirac matrices. Coulomb potential should be included into U^V. The scattering observables, cross sections, analyzing powers and spin rotation parameters, are obtained by solving the Dirac equation.

C Unfolding of proton charge distribution

Point proton distributions are necessary for the RIA calculations as described in the main text. Charge distributions of nuclei can be obtained from electron scattering, however they are different from point proton distributions since a proton itself has its own charge distribution and magnetic moments of protons and neutrons also contribute to the charge densities. In order to obtain point proton distributions it is necessary to exclude such effects. Here only the proton charge distribution is considered since contribution from magnetic moments are roughly two order smaller than that of the proton charge distribution.

Charge distributions of nuclei $\rho^{ch}(\vec{r})$ are expressed with point proton distributions $\rho_p(\vec{r})$ and proton charge distributions $\rho_p^{ch}(\vec{r})$;

$$\rho^{ch}(\vec{r}) = \int \rho_p(\vec{r}')\,\rho_p^{ch}(\vec{r}-\vec{r}')\,d\vec{r}'. \qquad (94)$$

Form factors can be obtained by taking Fourier transform as

$$\begin{aligned} F^{ch}(\vec{q}) &= \int \rho^{ch}(\vec{r})\, e^{-i\vec{q}\cdot\vec{r}} d\vec{r} \\ &= \int \rho_p(\vec{r}')\rho_p^{ch}(\vec{r}-\vec{r}')\, e^{-i\vec{q}\cdot\vec{r}} d\vec{r} d\vec{r}' \end{aligned}$$

$$
\begin{aligned}
&= \int \rho_p(\vec{r}\,')\rho_p^{ch}(\vec{r}\,'')\, e^{-i\vec{q}\cdot(\vec{r}\,'+\vec{r}\,'')} d\vec{r}\,' d\vec{r}\,'' \quad (\text{note; } \vec{r}-\vec{r}\,' \equiv \vec{r}\,'') \\
&= \int \rho_p(\vec{r}\,')\, e^{-i\vec{q}\cdot\vec{r}\,'} d\vec{r}\,' \int \rho_p^{ch}(\vec{r}\,'')\, e^{-i\vec{q}\cdot\vec{r}\,''} d\vec{r}\,'' \\
&= F_p(\vec{q})\, F_p^{ch}(\vec{q}), \qquad (95)
\end{aligned}
$$

thus

$$
F_p(\vec{q}) = \frac{F^{ch}(\vec{q})}{F_p^{ch}(\vec{q})}. \qquad (96)
$$

If both $F^{ch}(\vec{q})$ and $F_p^{ch}(\vec{q})$ are known, $\rho_p(\vec{r})$ can be obtained from the inverse Fourier transform of (96);

$$
\rho_p(\vec{r}) = \frac{1}{(2\pi)^3} \int F_p(\vec{q})\, e^{+i\vec{q}\cdot\vec{r}} d\vec{q}. \qquad (97)
$$

Although numerical integration is necessary in general, it has an analytic form in some special cases as described below.

From now, only spherically symmetric nuclei are considered. The proton charge distribution is assumed to be the following form;

$$
\rho_p^{ch}(r) = \frac{1}{\pi^{3/2} a_p^3} e^{-(r/a_p)^2}, \qquad (98)
$$

where a_p is related to root mean square radius of proton charge distribution as

$$
\left\langle r_p^2 \right\rangle^{1/2} = \sqrt{\frac{3}{2}}\, a_p. \qquad (99)
$$

The Fourier transform can be performed analytically in this case. Resulting charge form factor is

$$
\begin{aligned}
F_p^{ch}(q) &= \int \frac{1}{\pi^{3/2} a_p^3} e^{-(r/a_p)^2} e^{-i\vec{q}\cdot\vec{r}} d\vec{r} \\
&= e^{-a_p^2 q^2/4}. \qquad (100)
\end{aligned}
$$

Charge distributions of various nuclei are obtained in the sum of Gaussians (SOG) forms;

$$
\rho^{ch}(r) = \frac{Z}{2\pi^{3/2}\gamma^3} \sum_i \frac{Q_i}{1+2R_i^2/\gamma^2} \left(e^{-(r-R_i)^2/\gamma^2} + e^{-(r+R_i)^2/\gamma^2} \right), \qquad (101)
$$

where γ and R_i represent width and central position of each Gaussian, $\sum_i Q_i = 1$ due to the normalization of the volume integral. The Fourier transformation of (101) is also carried out analytically and the result is

$$
F^{ch}(q) = \sum_i \frac{Z Q_i}{1+2R_i^2/\gamma^2} \left[\cos(qR_i) + \frac{2R_i^2}{\gamma^2} j_0(qR_i) \right] e^{-\gamma^2 q^2/4}, \qquad (102)
$$

where j_0 is a spherical Bessel function. By using (96) the form factors of the point proton distribution become

$$F_p(q) = \sum_i \frac{ZQ_i}{1+2R_i^2/\gamma^2}\left[\cos(qR_i) + \frac{2R_i^2}{\gamma^2} j_0(qR_i)\right] e^{-\Gamma^2 q^2/4}, \qquad (103)$$

where $\Gamma^2 \equiv \gamma^2 - a_p^2$. The inverse Fourier transform becomes an analytic expression again;

$$\begin{aligned}
\rho_p(r) &= \frac{1}{(2\pi)^3}\int F_p(q)\, e^{+i\vec{q}\cdot\vec{r}}\, d\vec{q} \\
&= \frac{1}{2\pi^2 r}\int_0^\infty q\sin(qr)F_p(q)dq \\
&= \frac{Z}{2\pi^{3/2}\Gamma^3}\sum_i \frac{Q_i}{1+2R_i^2/\gamma^2} \\
&\quad \times\left[\left(1-\frac{\alpha_i}{r}\right) e^{-(r-R_i)^2/\Gamma^2} + \left(1+\frac{\alpha_i}{r}\right) e^{-(r+R_i)^2/\Gamma^2}\right], \qquad (104)
\end{aligned}$$

where $\alpha_i \equiv R_i a_p^2/\gamma^2$. Thus point proton distributions are deduced in the explicit analytic form. It is notable that resulting form of (104) is similar to (101) with the new width parameter $\Gamma = \sqrt{\gamma^2 - a_p^2}$.

D Rapid Data Transfer Module

We developed a new module called a "Rapid Data Transfer Module" (RDTM) for the experiment. It is a key module for a new data acquisition system for high rate measurements with the focal plane polarimeter and is now included into the standard data acquisition system at RCNP.

Previously, the data have been collected by the Starburst from modules in the CAMAC crate, transferred to the front-end VME, and broadcasted to other nodes on the system with reflective memory boards (RFM) through a fiber optic link[26]. By the use of RFM's, a 2 Mbytes/sec data transfer rate has been achieved for the VME-VME transfer. However the total data acquisition rate has been limited by CAMAC cycles. In consideration of the software overheads following the CAMAC actions, the total acquisition rate has been reduced to be about 160 Kbytes/sec. In order to utilize the full performance of RFM's it was indispensable for us to exclude CAMAC actions from the data flow. Thus we developed the RDTM[28].

The RDTM is designed as an interface between a LeCroy DATABUS and an ECL BUS of a CES8170 High Speed Memory (HSM). The schematic view of the system is illustrated in Fig. 40. The data from multi wire proportional

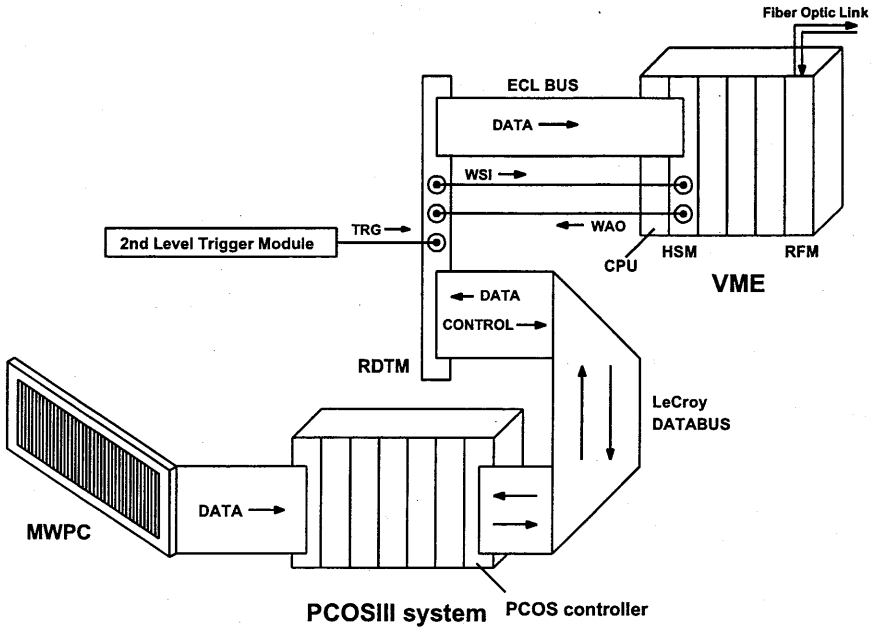

Figure 40: Schematic view of the new data acquisition system.

counters (MWPC) (they adopt the LeCroy DATABUS system) are transferred through the RDTM to the HSM in the VME crate and stored on it. They are broadcasted to other nodes on the system with RFM's through a fiber optic link. Only the hardware trigger signals are used and there is no software intervention in this transfer cycle. Thus we can exclude CAMAC actions from the data flow and a high transfer rate is realized.

For the convenience of the data analysis, the RDTM appends an event header and an event number before each of the PCOS data block. The 16bit event header can be arbitrary set by DIP switches implemented on the side of the RDTM. The event number is a scaler data which counts scaler inclement signals generated event by event. These additional information enables us to accumulate the data from various detectors on different memory modules in parallel. Such multi buffering system is essential for achieving high speed data transfer.

Since the system is designed for the experiments with the use of the 2nd level trigger system which judges whether the current event is useful or not, the data transfer cycle is started only when the RDTM receives the trigger signal from the 2nd level trigger circuit during the request signal from the PCOS controller is activated.

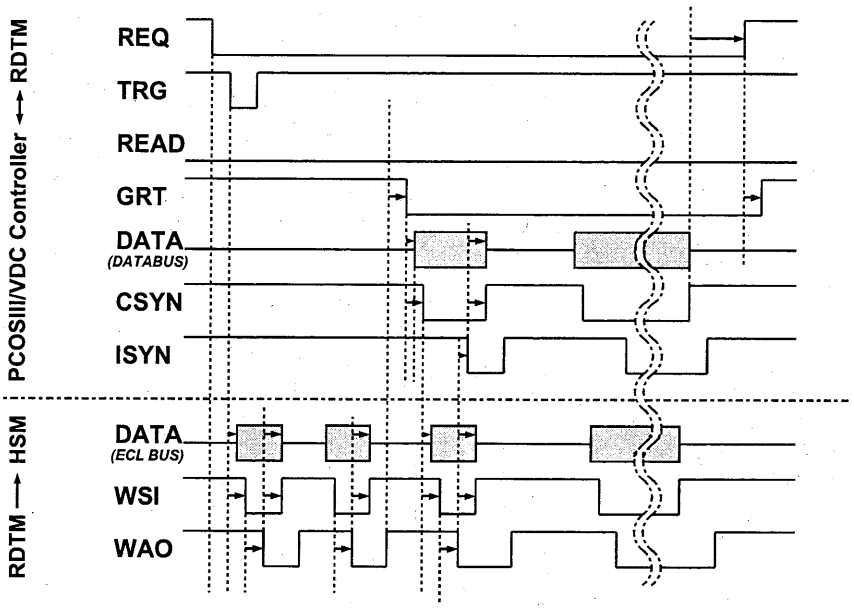

Figure 41: Timing chart in the normal data transfer mode.

Figure 41 illustrates the timing chart in the normal data transfer mode. It is drawn in the negative logic convention (i.e. the low level means "true"). A request signal REQ is generated by the PCOS controller when the data are available. After the 2nd level trigger accept signal TRG is received, the event header data is sent to the HSM via the ECL BUS along with a write strobe input signal WSI. The HSM generates a write acknowledge output WAO after accepting the data. The event number is transferred in the same manner. After the transfer of the event header and number, the RDTM activates a grant signal GRT which indicates that the RDTM is ready to accept data from the PCOS controller. In the response of GRT, the controller sends the first data via the LeCroy DATABUS along with a CSYN signal. The RDTM receives this data, converts to the ECL logic signals, and stores on the ECL BUS. The data is transferred to the HSM in the same manner of the event header and number. After receiving the WAO signal from the HSM, the RDTM activates an ISYN signal which indicates the end of the first data transfer. Then the next data is transferred. After all data are transferred, the PCOS controller deactivates the REQ signal and the transfer cycle is terminated.

We measured the transfer rate by a pulser test. The photograph of the oscilloscope taken at the test is shown in Fig. 42. Three signals are the REQ,

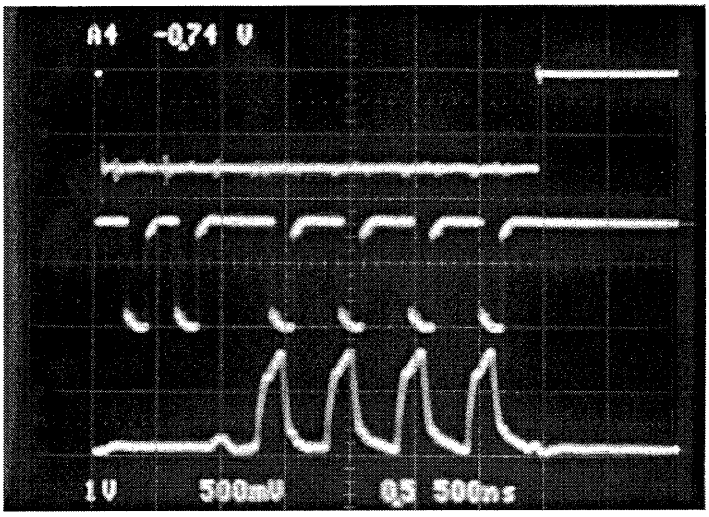

Figure 42: Picture of the oscilloscope at the pulser test.

WSI and $\overline{\text{CSYN}}$ signals from top to bottom, respectively. It is clearly shown that the PCOS controller waits for the first two WSI's correspond to the event header and number, and only after the end of the event number transfer it sends a write strobe signal CSYN to the RDTM. Since the horizontal scale is 500 nsec/division, the transfer rate is estimated to be about 2 Mwords/sec (i.e. 4 Mbytes/sec). This rate is comparable with that of the VME-VME transfer via the RFM. Thus the RDTM can extract the full performance of the previous data acquisition system.

The PCOS controller receives some commands to set logical addresses, threshold voltages and delays on LeCroy 2731A Delay and Latch Modules by writing data on the LeCroy DATABUS in a specific format. It is called "AUTOTRIM". Speed is not necessary for the AUTOTRIM. The RDTM accepts F(16)A(0) CAMAC functions to utilize the AUTOTRIM features. Timing chart in the AUTOTRIM mode is illustrated in Fig. 43. When the RDTM receives F(16)A(0) CAMAC action, it reads the data on the CAMAC DATAWAY at the timing of an S1 strobe signal, deactivates a READ signal, and transfers the data to the LeCroy DATABUS along with the ISYN. The PCOS controller returns the CSYN signal as the receipt. The deactivated READ signal indicates that the LeCroy DATABUS is in WRITE mode and the RDTM can write data on the DATABUS.

All CAMAC commands supported by the RDTM are summarized in Table 15.

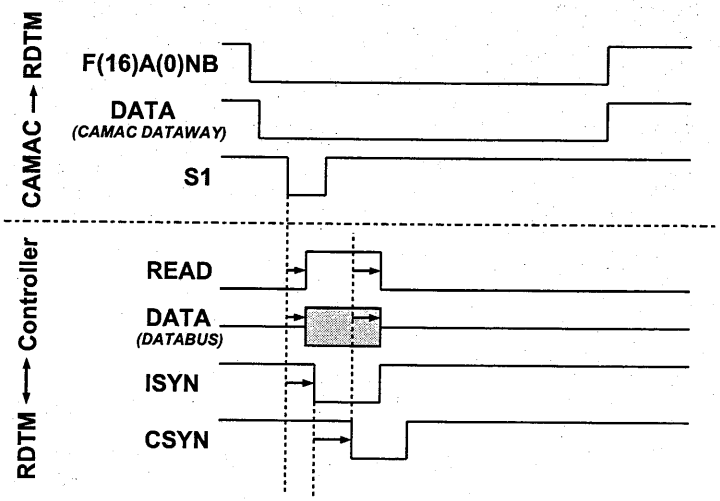

Figure 43: Timing chart in the AUTOTRIM mode.

Table 15: CAMAC commands supported by the RDTM. *INH signal on the DATABUS is generated if INH register or I signal of the CAMAC DATAWAY are activated.

commands	actions
Z or C	Initializes the RDTM.
	Internal INH register and event number are cleared.
	MASTER RESET is asserted on the LeCroy DATABUS.
I	Activates INH*.
F(9)A(0)	Same as Z or C.
	A Q-response is always generated.
F(11)A(0)	Same as F(9)A(0).
F(16)A(0)	A CAMAC data word is transferred to the DATABUS
	if all of REQ, INH and BUSY are not activated.
	(i.e. if the DATABUS is free).
	A Q-response is generated if the DATABUS is free.
F(24)A(0)	Activates INH register*.
	A Q-response is always generated.
F(26)A(0)	Clears INH register*.
	A Q-response is always generated.
F(27)A(0)	A Q-response is generated if BUSY is activated.

References

[1] L. G. Arnold, B. C. Clark, R. L. Mercer and P. Schwandt, Phys. Rev. **C23**, (1981) 1949.

[2] S. Hama, B. C. Clark, E. D. Cooper, H. S. Sherif and R. L. Mercer, Phys. Rev. **C41**, (1990) 2737; E. D. Cooper, S. Hama, B. C. Clark and R. L. Mercer, Phys. Rev. **C47**, (1993) 297. FORTRAN77 code is also available from `ftp://ftp.physics.ohio-state.edu/tmp/global/global.for`.

[3] J. A. McNeil, J. R. Shepard and S. J. Wallace, Phys. Rev. Lett, **50**, (1983) 1439; J. R. Shepard, J. A. McNeil and S. J. Wallace, Phys. Rev. Lett, **50**, (1983) 1443.

[4] D. P. Murdock and C. J. Horowitz, Phys. Rev. **C35**, (1987) 1442.

[5] C. J. Horowitz, Phys. Rev. **C31**, (1985) 1340.

[6] J. A. Tjon and S. J. Wallace, Phys. Rev. **C32**, (1985) 1667; Phys. Rev. **C36**, (1987) 1085.

[7] N. Ottenstein, S. J. Wallace and J. A. Tjon, Phys. Rev. **C38**, (1988) 2272.

[8] H. Sakaguchi, H. Takeda, S. Toyama, M. Itoh, A. Yamagoshi, A. Tamii, M. Yosoi, H. Akimune, I. Daito, T. Inomata, T. Noro and K. Hosono, Phys. Rev. **C57** (1998) 1749.

[9] E. J. Stephenson, in *Antinucleon- and Nucleon-Nucleus Interactions*, Telluride, Colorado, 1985, edited by G. E. Walker *et al.* p. 299 (Plenum, New York, 1985).

[10] M. Yoshimura, M. Nakamura, H. Akimune, I. Daito, T. Inomata, M. Itoh, M. Kawabata, T. Noro, H. Sakaguchi, H. Takeda, A. Tamii, K. Yonehara, H.P. Yoshida, and M. Yosoi, Phys. Rev. **C63** (2001) 034618.

[11] R. W. Fergerson *et al.*, Phys. Rev. **C33**, (1986) 239.

[12] E. Bleszynski *et al.*, Phys. Rev. **C37**, (1988) 1527.

[13] A. Rahbar *et al.*, Phys. Rev. Lett. **47**, (1981) 1811.

[14] B. Aas *et al.*, Nucl. Phys. **A460**, (1986) 675.

[15] O. Häusser *et al.*, TRIUMF Annual Report 1987, p.35.

[16] O. Häusser *et al.*, Phys. Lett. **B184**, (1987) 316.

[17] L. Ray, Phys. Rev. **C19**, (1979) 201.

[18] A. K. Kerman, H. McManus, R. M. Thaler, Ann. Phys. **8**, (1959) 551.

[19] T. Taki, H. Sakaguchi, M. Yosoi, H. Takeda, A. Tamii, M. Itoh, T. Kawabata, T. Noro, H. Akimune, M. Yoshimura, T. Inomata, I. Daito, H. Yoshida and E. Obayashi, RCNP Annual Report 1997, (1998) 56.

[20] K. Hatanaka, K. Takahisa, H. Tamura, M. Sato and I. Miura, Nucl. Instr. and Meth. **A384**, (1997) 575.

[21] K. Nagayama and K. Hatanaka, RCNP Annual Report 1998, (1999) 119.

[22] M. Fujiwara, H. Akimune, I. Daito, H. Fujimura, K. Hatanaka, H. Ikegami, I. Katayama, K. Nagayama, N. Matsuoka, S. Morinobu, T. Noro, M. Yoshimura, H. Sakaguchi, Y. Sakemi, A. Tamii, M. Yosoi, Nucl. Instr. and Meth. **A422**, (1999) 484.

[23] T. Noro, M. Fujiwara, O. Kamigaito, S. Hirata, Y. Fujita, A. Yamagoshi, T. Takahashi, H. Akimune, Y. Sakemi, M. Yosoi, H. Sakaguchi and J. Tanaka, RCNP Annual Report 1991, (1992) 177.

[24] H. Yoshida, T. Baba, T. Noro, M. Kawabata, H. Akimune, H. Sakaguchi, A. Tamii, H. Takeda and T. Kawabata, RCNP Annual Report 1996, (1997) 164.

[25] M. Yosoi, H. Akimune, I. Daito, T. Inomata, T. Ishikawa, M. Itoh, T. Kawabata, M. Nakamura, T. Noro, E. Obayashi, H. Sakaguchi, A. Tamii, H. Takeda, T. Taki, H. Yoshida and M. Yoshimura, RCNP Annual Report 1997, (1998) 245.

[26] A. Tamii, H. Sakaguchi, H. Takeda, M. Yosoi, H. Akimune, M. Fujiwara, H. Ogata, M. Tanaka and H. Togawa, IEEE Trans. on Nucl. Sci. **43**, (1996) 2488; A. Tamii *et al.*, *Proc. 2nd Int. Data Acquisition Workshop on Networked Data Acquisition System*, (World Scientific, Singapore, 1997), pp.238.

[27] T. Kawabata, H. Sakaguchi, A. Tamii, H. Takeda, T. Taki and H. Yoshida, RCNP Annual Report 1996, (1997) 161.

[28] H.Takeda, H. Sakaguchi, A. Tamii, H. Akimune, M. Kawabata, and M. Tanaka, *Proc. of the 1995 IEEE Conf. on Real-Time Computer*

Applications in Nuclear Particle and Plasma Physics, 1995, p.210.; H. Takeda, H. Sakaguchi, A. Tamii, M. Tanaka and H. Akimune, RCNP Annual Report 1995, (1996) 177.

[29] *Proc. 3rd Int. Symp. on Polarization Phenomena in Nuclear Reactions*, Madison, 1970.

[30] M. Ieiri, H. Sakaguchi, M. Nakamura, H. Sakamoto, H. Ogawa, M. Yosoi, T. Ichihara, N. Isshiki, Y. Takeuchi, H. Togawa, T. Tsutsumi, S. Hirata, T. Nakano, S. Kobayashi, T. Noro and H. Ikegami, Nucl. Instr. and Meth. **A257**, (1987) 253.

[31] M. R. Leo, *Techniques for Nuclear and Particle Physics Experiments 2nd. Ed.*, (Springer-Verlag, Berlin, 1994), Chapter 2; for example.

[32] G. G. Ohlsen, Rep. Prog. Phys. **35**, (1972) 717.

[33] M. W. McNaughton *et al.*, Nucl. Instr. and Meth. **A241**, (1985) 435.

[34] M.Yosoi, A. Tamii, H. Akimune, I. Daito, T. Inomata, M. Itoh, M. Kawabata, T. Kawabata, M. Nakamura, T. Noro, H. Takeda, T. Taki, H. Toyokawa, H. Yoshida, M. Yoshimura and H. Sakaguchi, RCNP Annual Report 1996, (1997) 127.

[35] Particle Data Group, Euro. Phys. J. **C15**, (2000) 1; *Particle Physics Booklet*, (Springer, 2000), p.194.

[36] L. Wolfenstein, Ann. Rev. Nucl, Sci. **6** (1956) 43.

[37] R. D. Sard, *RELATIVISTIC MECHANICS*, (W. A. BENJAMIN, INC., New York, 1970), Chapter 5; for example.

[38] C. J. Horowitz, D. P. Murdock and B. D. Serot, *Computational Nuclear Physics 1*, (Springer-Verlag, Berlin, 1991), Chapter 7.

[39] C. J. Horowitz and B. D. Serot, Nucl. Phys. **A368**, (1981) 503.

[40] H. V. von Geramb, *The Interaction Between Medium Energy Nucleons in Nuclei*, edited by H. O. Mayer, AIP Conf. Proc. No. 97 (AIP, New York, 1982), p. 44.

[41] L.Rikus *et al.*, Nucl. Phys. **A414**, (1984) 413; L. Rikus *et al.*, Nucl. Phys. **A426**, (1984) 496.

[42] I. Sick, Nucl. Phys. **A218**, (1974) 509; for example.

[43] H. de Vries *et al.*, Atomic Data and Nuclear Data Tables **36**, (1987) 495, and references therein.

[44] L. R. B. Elton, *Nuclear Sizes*, (Oxford University Press, London, 1961).

[45] H. Gao, *Proc. of the 14th International Spin Physics Symposium (SPIN2000)*, AIP Conf. Proc. Vol. 570, (Melville, New York, 2001), p.79, and references therein.

[46] A. Krasznahorkay, M. Fujiwara, P. van Aarle, H. Akimune, I. Daito, H. Fujimura, Y. Fujita, M. N. Harakeh, T. Inomata, J. Jänecke, S. Nakayama, A. Tamii, M. Tanaka, H. Toyokawa, W. Uijen and M. Yosoi, Phys. Rev. Lett. **82**, (1999) 3216.